Aus dem Walther-Straub-Institut für Pharmakologie und Toxikologie

der Ludwig-Maximilians-Universität München

Vorstand: Prof. Dr. med. Thomas Gudermann

Dissertation

zum Erwerb des Doctor of Philosophy (Ph.D.) an der

Medizinischen Fakultät der

Ludwig-Maximilians-Universität zu München

Endolysosomal cation channels and toxic chronic lung disease

vorgelegt von

Barbara Julia Spix

aus Willich, Deutschland

2022

Mit Genehmigung der Medizinischen Fakultät der

Ludwig-Maximilians-Universität zu München

First evaluator: *Prof. Dr. Dr. Christian Grimm*

Second evaluator*: Prof. Dr. Martin Biel*

Third evaluator: Priv. Doz. Dr. Annette Pohl-Koppe

Fourth evaluator: apl. Prof. Dr. Markus Rehberg

Dean: *Prof. Dr. med. Thomas Gudermann*

Date of defense:

29.04.2022

To my mother Elisabeth Spix,

with deep love and gratitude

Table of content

Abstract (English):

Chronic obstructive pulmonary disease (COPD) is a prevalent disease that affects million people worldwide. Classified as the third most common cause of death globally, it accounts for more than 3 million deaths per year. Smoking constitutes the main risk factor for developing COPD, while other factors include inhalation of environmental pollutants such as exhaust fumes from the industry or vehicles, occupational dusts and fumes, or genetic predispositions. Characteristic for COPD is a chronically inflamed lung and permanent pathological changes of the airways and lung tissue. Consequently, this leads to common symptoms like chronic cough, sputum, and shortness of breath, all of which significantly affect the quality of life. Two common forms of COPD can be described: chronic bronchitis associated with mucus hyper-production, and emphysema resulting from destruction of alveolar tissue, e.g. due to an excess of the macrophage elastase MMP-12. However, treatment options are poor, as no drugs are currently available that can slow down COPD progression or reduce the disease mortality. Thus, it is important and necessary to uncover novel treatment strategies and drug targets.

In this dissertation, the endolysosomal cation channel TRPML3 was investigated in the context of COPD and emphysema development with the aim to evaluate its potential as therapeutic target. Being located on membranes of intracellular organelles such as early endosomes and lysosomes, TRPML3 is involved in membrane fusion and fission events including endocytosis, trafficking, exocytosis, and autophagy. Here, by the use of the following novel reporter mouse line, *Trpml3*-IRES-Cre/*eR26*-τGFP, TRPML3 was found to be mainly expressed in alveolar macrophages (AMΦ) in the lungs. Further studies on lung function, and examination of lung tissues revealed that *Trpml3* deficient (*Trpml3*$^{-/-}$) mice show a pulmonary emphysema phenotype. This was demonstrated under both basal conditions and toxic conditions, meaning the exposure to cigarette smoke to induce COPD, and the application of a porcine pancreatic elastase to induce emphysema in the lungs. Analysis of bronchoalveolar lavage fluid (BAL-F) obtained from *Trpml3*$^{-/-}$ mice unveiled increased levels of the AMΦ-specific protease MMP-12, whereas other inflammatory cytokines, proteases and antiproteases, i.e. tissue inhibitor of metalloproteinases (TIMPs), were unchanged. Furthermore, loss of TRPML3 in AMΦ did not affect lysosomal exocytosis, but resulted in impairments in endolysosomal trafficking and endocytosis, being causative for the increased levels of MMP-12 also found in AMΦ cell culture supernatants and likely in BAL-F.

Overall, this work discovered a significant role of TRPML3 in COPD and emphysema development. Mice lacking TRPML3 were unveiled to be particularly susceptible for developing pulmonary emphysema, attributed to the reduced capacity of *Trpml3*$^{-/-}$ AMΦ to balance the MMP-12 concentration in the lungs properly (**Figure 1**). Functioning as such

a key regulator for MMP-12, TRPML3 may be considered as novel therapeutic target structure for the treatment of COPD.

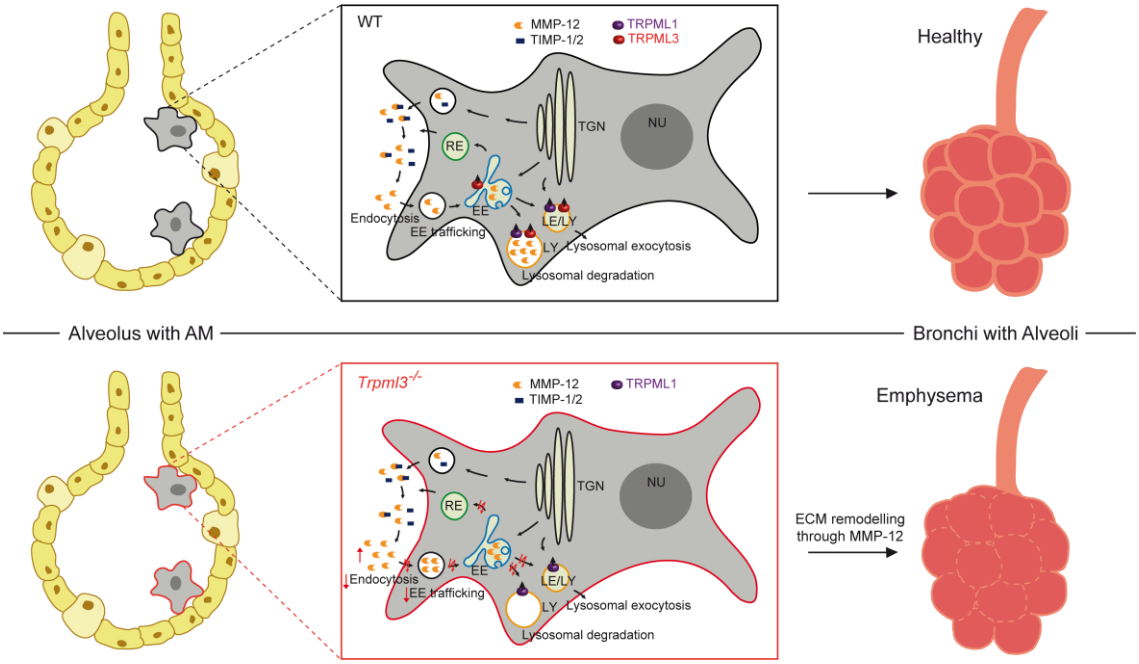

Figure 1. Mechanisms governing emphysema formation in *Trpml3*$^{-/-}$ lungs. Loss of TRPML3 leads to an imbalance in favor of MMP-12 over TIMPs due to trafficking and endocytosis defects in *Trpml3*$^{-/-}$ AMΦ compared to wildtype (WT) AMΦ. This results in the remodeling of extracellular matrix (ECM) of the lung tissue and emphysema formation. From: Spix et al., *Nat Commun* 13**,** 318 (2022) (1).

List of figures

List of tables

List of abbreviations

AMΦ	alveolar macrophages
AT	alveolar type
BAL	bronchoalveolar lavage
BAL-F	bronchoalveolar lavage fluid
BMDMΦ	bone marrow-derived macrophages
BSA	bovine serum albumin
BSAP	B-cell specific activator protein
BTK	bruton tyrosine kinase
CAST	computer-assisted stereological toolbox
CCL2	CC-chemokine ligand 2
CCSP	club cell secretory protein
cDNA	complementary DNA
CIE	clathrin-independent endocytosis
CME	clathrin-mediated endocytosis
COPD	chronic obstructive pulmonary disease
CS	cigarette smoke
DAPI	4’,6-diamidino-2-phenylindole, dihydrochloride
DMEM	Dulbecco's Modified Eagle Medium
DMSO	dimethyl sulfoxide
Dyn	dynasore
ECM	extracellular matrix
EE	early endosome
EEA1	early endosome antigen 1
EGF	epidermal growth factor
EIPA	5-(N-ethyl-N-isopropyl)-amiloride
ELISA	enzyme-linked immunosorbent assay
eR26	enhanced ROSA26
FA	filtered air
FACS	fluorescence-activated cell sorting
FBS	fetal bovine serum
FEV_1	forced expiratory volume per 1 second
FOT	forced oscillation technique

GOLD	Global Initiative for Chronic Obstructive Lung Disease
GRO-α	growth-regulated oncogene-α
H&E	hematoxylin & eosin
HBEC	human bronchial epithelial cells
IFN- γ	interferon-γ
IL	interleukin
IMΦ	interstitial macrophages
IRES	internal ribosome entry site
KC/CXCL1	keratinocyte-derived chemokine/C-X-C motif chemokine ligand 1
MIG/CXCL9	monokine induced by gamma interferon/C-X-C motif chemokine ligand 9
KO	knockout
LABA	long-acting β_2-agonists
LAMA	long-acting muscarinic-antagonist
LAMP	lysosomal-associated membrane protein
LC3	microtubule-associated protein 1A/1B-light chain 3
LDH	lactate dehydrogenase
LE	late endosome
LSD	lysosomal storage disorder
LTB_4	leukotriene B_4
LY	lysosome
MBCD	methyl-ß-cyclodextrin
MCOLN	mucolipin
MCP1	monocyte chemotactic protein-1
MEM	Minimum Essential Media
MIP2	macrophage inflammatory protein 2
MLI	mean linear chord length
MLIV	mucolipidosis type IV
MMP	matrix-metalloproteinase
MP	macropinocytosis
mTOR	mammalian target of rapamycin
MUC5AC	mucin 5AC
MUF	4-methylumbelliferyl N-acetyl-β-D-glucosaminide
NE	neutrophil elastase
Nf-κB	nuclear factor kappa B

PAGE	polyacrylamid gel electrophoresis
PAX5	transcription factor paired box 5
PBS	phosphate buffered saline
PCL	periciliary layer
PCR	polymerase chain reaction
PDE-4	phosphodiesterase-4
Pen-Strep	penicillin-streptomycin
PFA	paraformaldehyde
PI	protease inhibitor
$PI(3,5)P_2$	phosphatidylinositol 3,5-bisphosphate
PM	plasma membrane
PNEC	pulmonary neuroendocrine cells
PVDF	polyvinylidine difluoride
qRT-PCR	quantitative real-time PCR
RE	recycling endosome
ROS	reactive oxygen species
RPMI	Roswell Park Memorial Institute 1640 medium
RT	room temperature
SABA	short-acting β_2-agonists
SAMA	short-acting muscarinic-antagonist
SDS	sodium dodecyl sulfate
SEM	standard error of the mean
SN	supernatant
SNAP	synaptosomal-associated protein
SNARE	soluble NSF (*N*-ethylmaleimide-sensitive factor) attachment protein receptor
SP	surfactant protein
Tf	transferrin
TFEB	transcription factor EB
TfR	transferrin receptor
TIMP	tissue inhibitor of metalloproteinase
TMD	transmembrane domain
TNF-α	tumor necrosis factor-α
TPC	two-pore channel
TPM	total particulate matter

TRPM	transient receptor potential channel melastatin
TRPML	transient receptor potential channel mucolipin
TRPV	transient receptor potential channel vanilloid
VEGF	vascular endothelial growth factor
VVG	verhoeff-van gieson
WB	western blot
WT	wildtype
τGFP	Tau green fluorescent protein

1. Introduction

1.1 Endolysosomal System

The endolysosomal system represents a highly dynamic transportation network within eukaryotic cells consisting of several interacting compartments such as early endosomes (EEs), recycling endosomes (REs), late endosomes (LEs) and lysosomes (LYs) (2). These organelles are crucial for the intracellular transport, breakdown and secretion of lipids, proteins and other macromolecules (3). For instance, receptors or other cargo molecules are taken up from the cell surface into EEs via a process called endocytosis, which can be further subclassified into clathrin-mediated endocytosis e.g. uptake of the transferrin receptor or clathrin-independent endocytosis e.g. uptake of lactosylceramide (4). In any case, internalized cargo can be either degraded via delivery to LEs and LYs or returned to the plasma membrane (PM). This recycling process may happen indirectly via REs, i.e. slow recycling, or directly from EEs, i.e. fast recycling (4,5). For the degradation pathway EEs undergo several modification processes such as formation of intraluminal vesicles, acidification, and adjustment of ion concentrations, all contributing to the maturation into LEs (5). After receiving lysosomal hydrolases from *trans*-Golgi network (6) and movement to the perinuclear region LEs are ready to fuse with LYs to conduct the degradation of the transported cargo (5). Apart from that, the fusion of lysosomes with the PM results in the release of its content into the extracellular space. This process called lysosomal exocytosis is crucial for cellular clearance, PM repair and remodeling of extracellular matrix (ECM) mediated through the released lysosomal content (7,8). The described processes, meaning endocytosis, endosome maturation, intracellular trafficking, fusion and lysosomal exocytosis are partially regulated by certain mediator proteins, for instance Rab proteins regulating trafficking and maturation (9) or soluble NSF attachment protein receptors (SNAREs), and synaptosomal-associated proteins (SNAPs) being relevant for fusion events (10). Other important factors are the endosomal pH and the maintenance of certain ion concentrations within the different compartments (5). For instance, it is known that endosomes and lysosomes contain high luminal concentrations of Ca^{2+}, the release of which is necessary for fusion and fission events (11). These ion concentrations are regulated and maintained by endolysosomal cation channels that are conducting ion fluxes across the membranes of EEs/LEs/LYs. Examples are the transient receptor potential channel mucolipins (TRPMLs) and two-pore-channels (TPCs). TRPMLs are being described in more detail in the following sections as they constitute one focus of this dissertation.

1.2 TRPML channels

TRPML channels constitute one of seven subfamilies within the superfamily of transient receptor potential ion channels and include three members in mammalian genomes, TRPML1, 2 and 3. All are composed of six transmembrane domains, from which domains 5 and 6 build up the pore region permeable for cations. TRPMLs were found to be expressed intracellularly in vesicles of the endolysosomal system, i.e., in EEs, REs, LEs and LYs to various degrees (12,13). The channel activity is regulated by phosphatidylinositol 3,5-bisphosphate ($PI(3,5)P_2$), as demonstrated before using endolysosomal patch-clamp (14), as well as by luminal pH. For TRPML1, the highest activity was reported at highly acidic pH as found in LYs (15), whereas it decreases with milder acidic conditions and is lowest at neutral pH (16). Vice versa, TRPML2 and TRPML3 are more active at higher pH, meaning less acidic luminal conditions, as present in EEs and REs (15,17,18). Being localized within the endocytic pathway, they are involved in several processes such as endocytosis (19), endosomal acidification (19), endolysosomal trafficking (17,20), lysosomal exocytosis (21,22), secretion (17), phagocytosis (21–23) and autophagy (21,24), as described in depths in the following paragraphs.

1.2.1 TRPML3

1.2.1.1 Structure of TRPML3

The human and murine TRPML3 protein, both composed of 553 amino acids, share 91% sequence identity (25). The predicted molecular weight is about 64kDa (25). Like the other TRPML channels, TRPML3 comprises six transmembrane domains (TMDs) forming a channel pore between TMD5 and TMD6 (25) (**Figure 2**). Of note, a prominent extracellular loop is present between TMD1 and TMD2 (25). Various mutations of distinct amino acids have been described for TRPML3 and were found to be associated with functional alterations of the channel. In this regard, the varitint-waddler phenotype was discovered in mice that is characterized by deafness, vestibular impairments, coat color dilution and circling behavior (26). Two semi-dominant alleles were found to be responsible: *Va*, carrying a substitution of alanine to proline at the position 419 ($A^{419}P$), and Va^J, carrying an additional substitution of isoleucine to threonine at position 362 ($I^{362}T$) (26–28). The mutation $A^{419}P$ results in a helix-break within transmembrane domain 5 and thus, in a constitutively active TRPML3 channel that leads to the accumulation of intracellular Ca^{2+} with subsequent cell death (28–31). This affects TRPML3 expressing cells like marginal cells of the stria vascularis, melanocytes, and hair cells of the inner ear (29,31,32), which explains the phenotypic abnormalities. The Va^J mutant isoform shows

a milder phenotype compared to the *Va* mutant, because the $I^{362}T$ mutation reduces the excessive channel activity (27,30). A mutation of the negatively charged asparagine to the positively charged lysine at position 458 ($D^{458}K$) within the putative pore loop inactivates the channel (33).

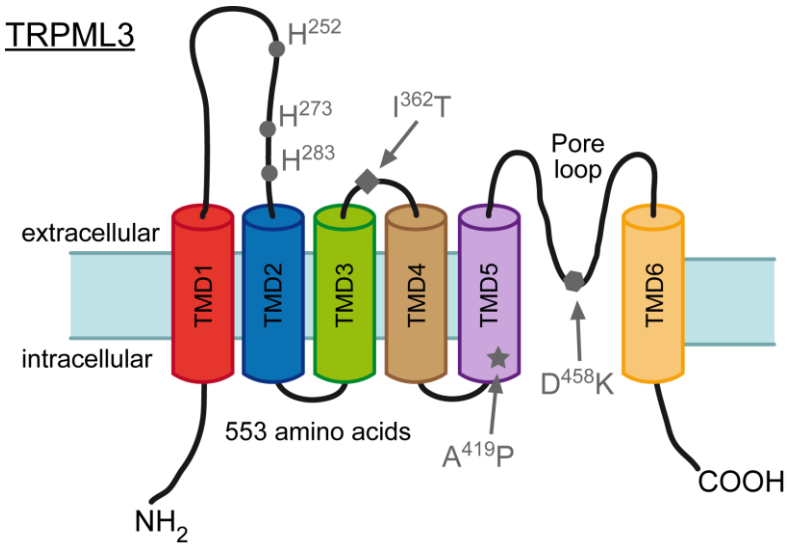

Figure 2. Predicted structure of TRPML3. Illustration showing TRPML3's six putative transmembrane domains (TMD1-TMD6), its pore region between TMD5 and TMD6 and its large extracellular loop between TMD1 and TMD2. Highlighted are various distinct amino acids or mutations that are assigned certain roles or phenotypes, as reported in the literature (18,29,33).

1.2.1.2 Expression of TRPML3

Various studies were performed to reveal TRPML3 expression in several tissues or tissue-specific cell types. Based on qRT-PCR of murine tissues, TRPML3 was detected in testis, muscle, bladder, colon, small intestine, stomach, pancreas, kidney, spleen, liver, lung, heart, thymus, tongue, eye, brain, and cerebellum (28,34). However, the expression levels for brain, thymus, lung, kidney, spleen and colon were clearly higher than the other analyzed tissues (28,34). Deriving from the varitint-waddler phenotype TRPML3 expression was investigated particularly in the inner ear and skin. Thus, TRPML3 was found in marginal cells of the stria vascularis, in melanocytes, and in vestibular and cochlea hair cells (26,29,32). Furthermore, the analysis of several other sensory organs revealed TRPML3 expression in vomeronasal and olfactory receptor neurons, more precisely in vesicles of their soma and dendrites, whereas no TRPML3 mRNA was found in retinal neurons, somatosensory neurons and taste receptor cells (32). Another pathological phenotype has been described for neonatal mice lacking both TRPML1 and

TRPML3, which confirmed high TRPML3 expression in intestinal enterocytes (35). Depletion of TRPML1 and TRPML3 in these cells correlates with an accelerated and abnormal vacuolation of endolysosomes (35). This leads to reduced endocytosis of nutrients from the intestinal lumen and results in growth delays, recovering after weaning, because mature enterocytes replace the neonatal ones that are specifically rich in endolysosomes (35). Most recently and as a part of this dissertation, TRPML3 was shown to be almost exclusively expressed in AMΦ in the lung, while other lung cell types showed no or low expression (1).

1.2.1.3 Functional roles of TRPML3

TRPML3 is an inwardly rectifying cation channel permeable for Ca^{2+} (18,27). The Ca^{2+} conductance and permeability of TRPML3 is inhibited by high sodium and regulated by luminal pH mediated by three histidine residues (H252, H273, H283) in the large extracytosolic loop of the channel (18) (**Figure 2**). A low pH of 6 already blocks the channel, while its activity is recovered at pH 7.4 (18). Another regulatory mechanism is described for Ca^{2+} ions that are trapped within the pore through binding to specific amino acids (33). This may protect the cell from an excessive Ca^{2+} influx, as this is toxic for the cell, as reported for the varitint-waddler phenotype. TRPML3 is localized in intracellular organelles (26,30,31), but is also found in the PM in overexpression systems, as demonstrated both in whole-endolysosomal and whole-cell patch clamp experiments (18,36). Located within the endolysosomal system, TRPML3 is implicated in several intracellular processes such as endocytosis, trafficking (37,38), autophagy (38), membrane fusion (19) and endosomal acidification (19). In these studies overexpression of TRPML3 was correlated with increased autophagy demonstrated by entire TRPML3 recruitment to autophagosomes upon exposure to cell stressors (38) and delayed epidermal growth factor degradation followed by accumulation in endosomes pointing to defects in trafficking and endocytosis (37,38). Knockdown of TRPML3 showed the opposite effects. Additionally, it resulted in Ca^{2+} accumulation in endosomes that led to impairments in endosomal acidification and increased endosomal fusion (19). Another functional role has been proposed for TRPML3 in human bladder epithelial cells, when infected by pathogens. TRPML3 senses the neutral pH of bacteria containing lysosomes and induces lysosomal exocytosis through Ca^{2+} release to eject the bacteria (23).

1.2.1.4 Relatives of TRPML3

1.2.1.4.1 TRPML1

Unlike its relatives TRPML2 and TRPML3, TRPML1 is ubiquitously expressed and not restricted to specific tissues or cell types and has been studied more extensively due to its clear link to the human disease mucolipidosis type IV (MLIV). Mutations in the mucolipin-1 (MCOLN1) gene are causative for this neurodegenerative lysosomal storage disorder (LSD) characterized by delayed psychomotor development and vision impairments (39,40). TRPML1 is primarily localized to lysosomal compartments (41) and there is clear evidence, that the channel is involved in lysosomal exocytosis through releasing Ca^{2+} from the lumen of the LY into the cytosol thereby inducing its fusion with the PM (21,22). Thus, lack or dysfunctions of TRPML1 is leading to an abnormal accumulation of diverse macromolecules e.g. lipids within LEs and LYs (42,43), as it was seen for human MLIV patient fibroblasts (44). The lysosomal exocytosis regulation through TRPML1 was further confirmed by the discovery of the transcription factor EB (TFEB) as a regulator for autophagy and lysosomal biogenesis, thereby promoting cellular clearance of pathological storage (45). It might therefore serve as therapeutic approach for the treatment of LSDs. TRPML1 has also been shown to be implicated in phagocytosis of large particles through macrophages (22,46). Upon stimulation of TRPML1 by its endogenous activator $PI(3,5)P_2$, lysosomal membranes are delivered to the PM at the site of particle engulfment via focal exocytosis to provide sufficient membrane for the phagocytosis process (22). The emerging phagosomes subsequently mature by fusion with LYs into phagolysosomes to promote particle degradation, a process also found to be induced through TRPML1 activation (46). Finally, TRPML1 has been investigated in depth in the context of autophagy. Both in MLIV patient fibroblasts and in cells lacking TRPML1, autophagic abnormalities have been observed such as the increase of microtubule-associated protein 1A/1B-light chain 3 (LC3) protein levels (47,48). LC3 is a marker for autophagosomes and abnormal protein amounts are an indication of impairments in autophagy. Several pathways have been suggested to explain the functional role of TRPML1 in autophagy: one points to a regulation of autophagy by the axis of TRPML1 – calcineurin – TFEB, meaning that Ca^{2+} release mediated by TRPML1 activates calcineurin, which in turn induces nuclear translocation of TFEB, an inducer of autophagy genes and lysosomal biogenesis (49). The activity of TFEB is inhibited through phosphorylation by mammalian target of rapamycin (mTOR) (50), and similarly mTOR was found to inhibit TRPML1 through phosphorylation (51,52). Thus, mTOR functions as a mediator to control both TRPML1 activity and TFEB activity: under starving conditions mTOR is inhibited, which activates TRPML1 and finally starts the autophagic machinery. An mTOR independent pathway to regulate autophagy has been described by Zhang et al. who found

reactive oxygen species (ROS) as activators of TRPML1, thereby activating the calcineurin – TFEB pathway resulting in induced autophagy (53). In this regard, TRPML1 functions as ROS sensor for the cell and may induce autophagy in case of high levels due to e.g. mitochondrial damage. In more recent studies TRPML1 was found to be involved in cancer cell proliferation (54) and cancer development (55).

1.2.1.4.2 TRPML2

Like TRPML1, TRPML2 was described as inwardly rectifying nonselective cation channel, conducting Ca^{2+}-ions from the lumen of endosomes, LYs or from the extracellular site into the cytosol, in case of overexpression of the channel (56,57). Tissue expression analyses revealed high levels of TRPML2 mRNA in lymphatic organs such as spleen and thymus, as well as kidney to a lower degree (34,58). Consistently with this, TRPML2 expression was found in immune cells, i.e. in activated macrophages (bone marrow-derived macrophages (BMDMΦ), AMΦ, microglia) (58), in several B-cell lines and primary B-lymphocytes (59), assigning them functional roles in the immune system (60). In this context, MCOLN2 expression was found to be regulated by the bruton tyrosine kinase (BTK) pathway (59) and by the transcription factor paired box 5 (PAX5) encoding the B-cell specific activator protein (BSAP) (61). Both BTK pathway and BASP/PAX5 represent important factors within B-cell development and differentiation, most obviously with TRPML2 being involved. Additionally, TRPML2 has been described as interaction partner of transmembrane protein 176A (62), a protein responsible to keep dendritic cells in an immature state (63). Except from these regulatory functions in the adaptive immune system, TRPML2 is also involved in innate immunity: TRPML2 was found to be upregulated in macrophages upon toll-like receptor stimulation through pathogen components such as lipopolysaccharide (58). Furthermore, it was shown that BMDMΦ lacking TRPML2 exhibit a decreased secretion of the CC-chemokine ligand 2 (CCL2) (58), while activation of TRPML2 using a selective agonist is increasing CCL2 secretion mediated through the early/recycling endosomal pathway (17), where high levels of TRPML2 were reportedly found (17,20,58). These afore mentioned findings strongly suggest a contribution of TRPML2 in innate immunity through CCL2 release and recruitment of immune cells. Finally and once more related to the immune response against pathogens, TRPML2 promotes trafficking of endocytosed viruses through the endosomal system, thereby enhancing virus replication and infection (64). Although these findings are strongly pointing to an involvement of TRPML2 in immune response, no human disease has been correlated with loss or dysfunctions of TRPML2, so far.

1.3 The mammalian respiratory system – Structure and function

Breathing provides the cells with oxygen that is indispensable for gaining energy through oxidative degeneration of nutrients. A similarly important function is the removal of metabolic products, primarily carbon dioxide, from the body. The lungs are fundamentally involved in these two important tasks: firstly, they transport air to the lung alveoli and secondly, they perform the gas exchange in the lung alveoli.

The air is initially transported through the upper respiratory tract, i.e. nasopharynx, oropharynx and larynx, before reaching the lower respiratory tract, consisting of the conducting airways (trachea, bronchi, and bronchioles) and the respiratory zone (alveoli) (65). The trachea is a wide, cartilaginous tube that splits into two main bronchi entering both right and left lung, respectively. Subsequently, the main bronchi subdivide into the lobar bronchi that are supplying the different lung lobes with oxygen, followed by segmental bronchi that further decrease in their lumen (65). Finally, these small bronchi turn into bronchioles followed by terminal and respiratory bronchioles, that branch into alveolar ducts, which are densely packed with alveoli (65). From the trachea to the alveoli the diameter of the airways constantly decreases, while the total cross sectional area massively increases (66). Such a high surface area of the respiratory zone is important for an efficient gas exchange within the alveoli. The trachea and large bronchi are made up of rings of cartilage that are providing stability and are keeping the airways open (67). Smaller bronchi only contain irregularly arranged plates of cartilage, while they are completely absent in the bronchioles and respiratory zone. A smooth muscle layer underneath the cartilaginous tissue is able to adapt the diameter of the airways (65).

1.3.1 Airway epithelium of the lower respiratory tract

The lower respiratory tract is lined with airway epithelium, which has a unique structure and composition depending on the region within the lung (**Figure 3A**). The conducting airways are lined with a pseudostratified columnar epithelium that consists of basal cells, club cells, goblet cells, ciliated cells, and neuroendocrine cells (**Figure 3B, C**).

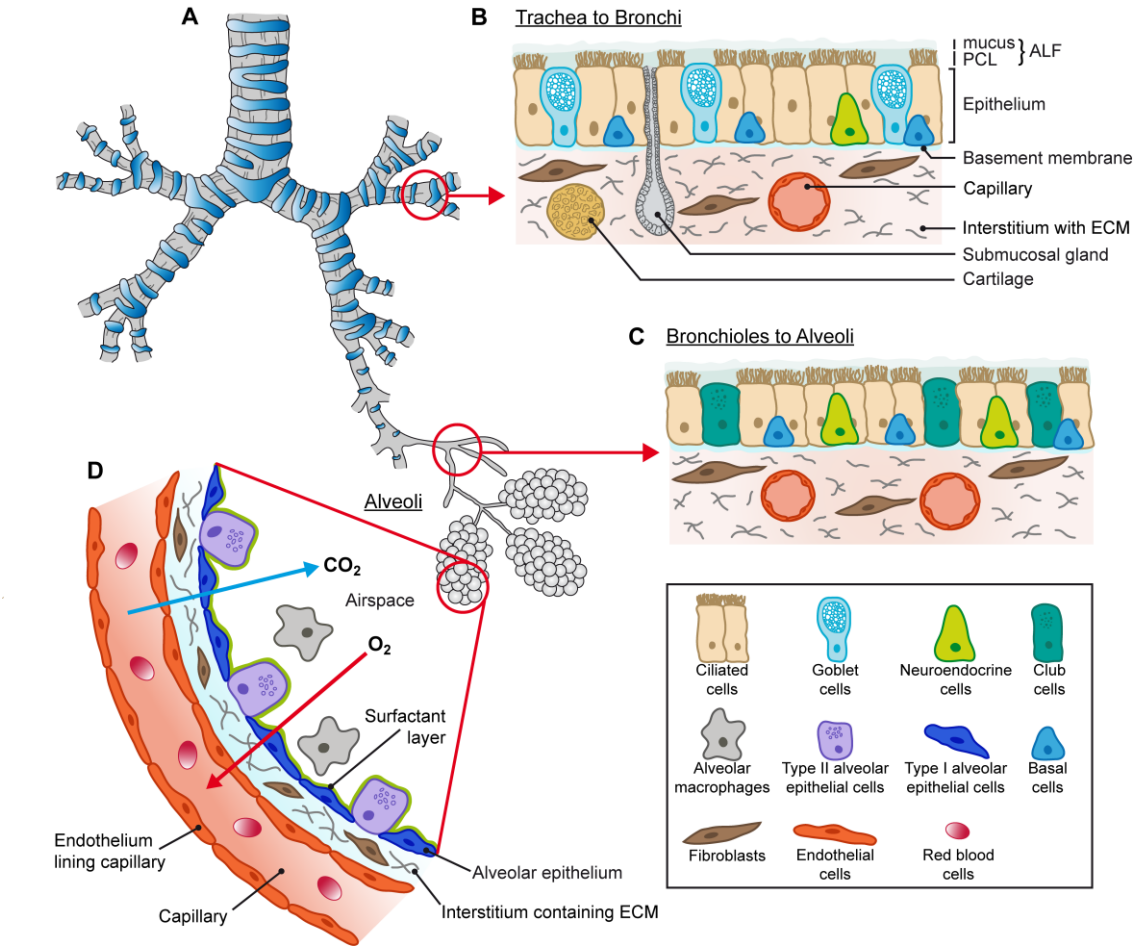

Figure 3. Structural cells of the lower respiratory tract. (A) Overview of the bronchial tree and its branches. (B, C) Structural composition of the conducting airway epithelium: trachea to bronchi (B) and bronchioles to alveoli (C). (D) Cellular composition of the alveolar epithelium and blood-air barrier.

Ciliated cells constitute the largest population of airway epithelial cells (68). On their apical surface, they carry tiny hair-like structures, called cilia that are performing propelling and coordinated movements (69). In this way, they are beating the airway lining fluid and therein mucus-trapped pathogens and particles towards the back of the throat (70). This clearing mechanism, known as mucociliary clearance, protects the lungs from any externally inhaled challenges that may have harmful effects on the airway or alveolar epithelium.

Goblet cells represent the major secretory cell type of the trachea-bronchial epithelium (69). They contain many secretory granules in their cytoplasm, from where mucins e.g. MUC5AC are released (71). Mucins are highly glycosylated macromolecular proteins and are essential components of the gel-like mucus layer (72), in which particle and pathogens are trapped. The mucus layer is located above the cilia-protecting periciliary layer (PCL), still reaching the tips of the cilia, and both together form the airway lining

fluid (73). Furthermore, there is growing evidence indicating the direct role of mucins in antimicrobial defense. It has been found that mucin production is stimulated by various microbial or inflammatory mediators such as β-glucan (74) and different interleukins (interleukin-13, -1β, -17A) (75,76).

Additionally, **submucosal glands** embedded within the interstitium of cartilaginous airways contribute to mucus production and host defense. In response to neuronal inputs (77), mucus cells of the proximal regions of the gland produce and secrete mucins, while serous cells located in the distal acini of the glands secrete water, ions and antimicrobial factors (78–80).

While the number of ciliated cells and goblet cells decreases form the trachea to the bronchioles, secretory **club cells** (previously named Clara cells) emerge in growing numbers being predominantly found in terminal and respiratory bronchioles (81,82). They have several functions: first, they produce and secrete various distinctive proteins, primarily club cell secretory protein (CCSP), but also mucins and surfactant proteins (A, B and D) (83,84), all contributing in forming the airway lining fluid. CCSP was also reported to have immunomodulatory effects, as the loss of club cells and reduced amounts of CCSP is correlated with the progression of COPD (85,86) or increased susceptibility to infections (87). Second, club cells exhibit stem-cell character and may serve as progenitors for ciliated cells and goblet cells. This unique capability of renewing the airway epithelium makes them an interesting target for the repair of destroyed lung epithelia, as it is present in chronic lung diseases (83,88). Finally, they play a key role in the detoxification of inhaled xenobiotics or compounds deemed toxic from e.g. tobacco smoke by the help of cytochrome P-450 (CYP) enzymes that are present in their cytoplasm (89,90). Thus, club cells are important to protect the lung epithelium from harmful influences from the environment.

Pulmonary neuroendocrine cells (PNEC) are very rare in the airway epithelium, representing only ~0.41% of all epithelial cells in human airways (91). They appear as solitary cells, but may also form clusters called neuroepithelial bodies (92). PNEC store various messenger molecules in densely packed secretory granules, e.g. serotonin, calcitonin, calcitonin gene-related peptide, substance P, that are released upon neuronal stimulation (93). Thereby, PNEC play a role in immune response, lung development/regeneration and regulation of pulmonary blood flow (92,94,95).

Finally, **basal cells** sticking to the basement membrane may serve as progenitor cells for goblet cells, club cells, ciliated cells and PNECs (96). As the main stem cells within the airway epithelium they are critical for self-renewal and lung regeneration upon injury (96,97).

Going deeper into the lung, the air reaches the **respiratory zone** made up of the respiratory bronchioles and plenty of alveoli grouped at the end of the alveolar ducts (**Figure 3D**). Compared to the conducting airways, the interstitium of the respiratory zone is much thinner, thereby enabling gas exchange between the oxygenated air and the carbon dioxide enriched blood (98). The interstitium is composed of ECM components, such as proteoglycans, glycoproteins, and collagen and elastin fibers that are providing stability for the lung tissue (99). Lung fibroblasts are embedded within the interstitial space and produce and secrete most of the ECM components, e.g. collagen, elastin, laminins, fibronectin, thereby being heavily involved in ECM maintenance (99). Pathological ECM remodeling also occurs in several lung diseases, e.g. COPD, lung cancer, and idiopathic pulmonary fibrosis (100).

Two different cell types make up the epithelium of the alveoli, first, **alveolar type I (AT1) cells**, and second, **alveolar type II (AT2) cells**. AT1 cells are flat epithelial cells lining the vast majority of the alveolar walls and are involved in the exchange of gas in-between the blood and the alveoli. Upon damage by inhaled toxicants, AT1 cells may be replaced through differentiating AT2 (101). On the contrary, AT2 cells are cuboidal shaped and reside only small amounts of the surface of the alveoli, although they are much more abundant in numbers (102). They produce and store pulmonary surfactant in so-called lamellar bodies, from where it is finally secreted into the liquid of the alveoli by exocytosis (103). Pulmonary surfactant is an extremely important factor for normal and healthy lung activity. It not only prevents the alveoli from collapse at the end of expiration through reducing the surface tension at the air-liquid interface, but also participates in host defense against infections (104). In this regard, the surfactant proteins SP-D and SP-A are able to opsonize pathogens, which makes it possible for AMΦ to easily phagocyte them (105,106). Even more, they seem to exhibit direct antibacterial and antifungal activity against several pathogens and can act as immunmodulators (107,108). There are several diseases known to be linked to surfactant dysfunction (109), e.g. deficiency of surfactant in premature infants is leading to neonatal respiratory distress syndrome (RDS) or loss of SP-D in mice is leading to lung emphysema (110).

1.4 Chronic lung diseases

Chronic lung diseases describe a status of the lung or other structures of the respiratory system, in which its histology and function is persistently and pathologically altered. It develops insidiously and usually worsens over time, causing difficulties in breathing and

affecting peoples' quality of life. Known risk factors are tobacco-smoking, allergies, inhalation of environmental pollutants, i.e. exhaust fumes from industries or vehicles, occupational dusts and fumes from chemicals, and in some cases, genetic predispositions. Chronic lung diseases include asthma, asbestosis, cystic fibrosis, pulmonary hypertension, restrictive lung diseases such as pulmonary fibrosis and obstructive pulmonary diseases such as COPD including chronic bronchitis and emphysema, the latter constituting the most prevalent disease. COPD is one of the main topics of this work, thereby being described in more detail in the following section.

1.4.1 Chronic obstructive pulmonary disease (COPD)

COPD is a collection term for various lung diseases, in which the airways are chronically inflamed and irreversibly narrowed, leading to restricted airflow and problems in breathing. The most common forms include chronic bronchitis characterized by an excessive production of mucus and emphysema denoted by the destruction of alveolar wall tissue.

1.4.1.1 Epidemiology

According to publications by the federal statistical office (Statistisches Bundesamt, Pressemitteilung Nr. N 036 vom 28. Mai 2021), the hospital cases due to smoking-related diseases such as COPD and lung cancer has increased by 18% in Germany within the past ten years. There have been 246 700 patients with an average age of 70.5 that needed to be treated fully stationary due to COPD. With more than 31 000 deaths, COPD accounted for the sixth most common cause of deaths in 2019 (111).

Globally, ischemic heart disease and stroke constitute the top causes of death, followed in third place by COPD (112). Resulting in the death of about 3 million people each year, COPD should be considered as a widespread disease and as a global health issue. Due to poor treatment options to stop disease progression or even cure it, and due to increasing air pollution, as well as still high popularity for smoking, it is likely that the worldwide prevalence of COPD will remain high in the decades to come.

1.4.1.2 Risk factors

There are several risk factors for COPD, but one must be mentioned in the first place: cigarette smoking, which clearly correlates with COPD prevalence (113). Since lung function is declining with increasing age, COPD is also more likely to occur in elderly people (113). Another risk factor with growing influence is the air pollution through fine

dust particles, nitrogen dioxide, ozone or sulfur dioxide, released by the industry or vehicles. This has been confirmed by several studies that found significant correlations between hospitalization rates of COPD patients and peaks of air pollutants (114,115). Further risk factors include occupational pollutants (116) e.g. cotton dust from the textile industry, dusts from coal mining or from the production of steel and iron. Finally, viral or bacterial infections during child- and adulthood also contribute to the development or progression of COPD, since they may cause damage to the respiratory epithelium resulting in declined lung function (117,118). However, there are people who are not heavily exposed to the mentioned risk factors and still develop COPD, as well as heavy smokers that don`t develop COPD. This implies genetic predisposition to play a role (119). Thus, it was found that lack of α_1-antitrypsin due to genetic polymorphisms in the SERPINA 1 gene is correlated with liver disease and lung emphysema (120,121), as reported for the PiZZ phenotype. Since α_1-antitrypsin functions as an inhibitor of proteases, e.g. neutrophil elastase, a deficit of α_1-antitrypsin leads to enhanced proteolytic events in the lung, resulting in COPD with emphysema. Other genes have been checked for potential polymorphisms and were found to be linked to COPD and worsening of lung function, such as a polymorphisms of MMP-9 (C-1562T) (122), MMP-1 (G-1607GG) (119), MMP-12 (rs652438 and rs2276109) (123) and of antioxidant genes (microsomal epoxide hydrolase, heme oxygenase, glutathione S-transferase) (119). Hence, genetic components in the development of COPD should not be neglected.

1.4.1.3 Pathomechansims of COPD

1.4.1.3.1 Enhanced chronic inflammation

COPD is characterized by a chronic inflammation in the lungs in response to the exposure to toxic particles. Lung macrophages are attributed a decisive role in these inflammatory processes. There are two types of macrophages in the lung: interstitial macrophages (IMΦ) and alveolar macrophages (AMΦ). IMΦ reside in the lung tissue, between the alveoli and the blood vessels, and develop from embryo yolk sac or from bone marrow derived monocytes circulating in the blood that continuously differentiate into local tissue macrophages after migration into the lung tissue (124). On the contrary, AMΦ are located within the alveoli, in close proximity to AT1 and AT2 cells. They originate from fetal monocytes and populate the airways shortly after birth (125). While tissue resident IMΦ are able to self-maintain themselves showing turnover rates of 21 days (126), AMΦ are long living cells with a slow replacement rate of about 40% in one year (127). Due to their direct exposure to the environmental air, AMΦ may be considered as guardians for the alveolar epithelium, as they are the first ones to face and clear the lungs from inhaled

pathogens and toxic particles (128). They eliminate those foreign invaders either through secretion of lysozyme, reactive oxygen products or antimicrobial proteases, which directly destroys microorganisms, or through phagocytosis or intracellular killing processes (128). In this way, they are strongly involved in the host defense of the lungs. Nevertheless, when the lungs are permanently exposed to cigarette smoke or other toxic particles as it is the case in many COPD patients, AMΦ initiate and drive pathological inflammatory processes in the lungs. They secrete a wide array of inflammatory mediators such as pro-inflammatory cytokines (e.g. tumor necrosis factor-α, interleukin-1β, interleukin-6) and several chemoattractants (e.g. MCP-1, CXC chemokines, interleukin-8, leukotriene B_4, growth related oncogene α) (129,130), which intensify the inflammation by recruiting more immune cells into the lung tissue. Thereby, monocytes circulating in the blood are attracted through CXC chemokines and MCP-1 and differentiate into lung tissue macrophages (131). Interluekin-8 and leukotriene B_4 are chemotactic mediators for neutrophils and $CD8^+$ T-cells that also migrate to the loci of inflammation (130). Again, these immune cells release further inflammatory mediators (e.g. TNF-α an interferon-γ by $CD8^+$ T-cells (132)), proteases (e.g. MMPs by macrophages, neutrophil elastase by neutrophils) or cytotoxic agents (e.g. ROS by macrophages and neutrophils) that either directly contribute to destruction of connective lung tissue or further drive and intensify the inflammation process, resulting in an chronic inflamed lung.

1.4.1.3.2 Protease-antiprotease imbalance

In addition to inflammation, there are other relevant key mediators being involved in the development of COPD: proteases and antiproteases. Proteases are enzymes that are cleaving proteins into smaller fragments through hydrolysis of peptide bonds. Thus, in lung tissue, they may degrade structural ECM constituents, e.g. elastin and collagen fibers, resulting in destruction of alveolar wall tissue and enlarged airspaces, as reported for an emphysema lung condition (130). There are three prominent classes of proteases associated with COPD: matrix-metalloproteinases (MMPs), cysteine proteases and serine proteases (133).

MMPs represent a large group of related enzymes that are capable of degrading matrix components. To catalyze this hydrolytic reaction, they contain a metal cation, usually Zn^{2+}, in their active site that gave this class of enzymes their name. MMPs are heavily involved in tissue remodeling, which is relevant for many biological processes, such as wound healing, development, angiogenesis, or pathological processes, such as cirrhosis, arthritis, tumor growth and metastasis. They are released by inflammatory cells, e.g. AMΦ and neutrophils. MMPs are divided into many subgroups and some of them have

been shown to be linked to COPD or emphysema, e.g. MMP-12, MMP-13 and MMP-9 (134). The collagenase MMP-13 was found to be mainly expressed in AMΦ and in AT2 cells and increased levels were found in lung tissue of COPD patients (135). MMP-9 is a gelatinase and degrades ECM components, as well as basal membrane. Several studies reported its contribution in airway inflammatory response, as MMP-9 concentrations were elevated in serum samples of COPD patients (136) and in the epithelial lining fluid, where it regulates the migration of human bronchial epithelial cells (HBEC) to repair wounds of the epithelium (137). Besides HBEC, sources of MMP-9 include several inflammatory cells, i.e. macrophages, neutrophils, monocytes, eosinophils and lymphocytes (138). Among the above mentioned MMPs, MMP-12 is certainly the one that has been most thoroughly investigated in COPD disease, especially emphysema. MMP-12 is also called macrophage elastase already pointing to its main origin, macrophages, and its main substrate, elastin, an important component of the ECM. MMP-12 is lowly expressed under basal condition, but is then highly upregulated upon smoke exposure, e.g. increased levels of MMP-12 were found in the sputum of patients with COPD (139). Importantly, the activity of MMPs need to be regulated, which is performed by the endogenously occurring tissue inhibitors of metalloproteinase (TIMPs), comprising four members: TIMP-1, TIMP-2, TIMP-3 and TIMP-4. Through their function of controlling MMP activity, the TIMPs are indirectly involved in ECM remodeling. Thus, homeostasis between TIMPs and MMPs is essential to maintain the tissue in a healthy, physiological state.

Next, cysteine proteases, specifically caspases, play another important role in COPD, as they regulate apoptosis, a complex mechanism of programmed cell death. In the lungs, apoptosis leads to death of structural epithelial cells. If those cells were not sufficiently replaced by new cells to maintain the epithelial barrier, it would result in tissue destruction and would contribute to COPD and emphysema formation. To this regard, several studies confirmed increased apoptosis of endothelial cells and alveolar epithelial cells in patients with COPD or emphysema (140,141).

Finally, serine proteases constitute another enzyme family with proteolytic activity. One prominent member is the neutrophil elastase (NE) that is predominantly expressed and secreted by neutrophils. Similar to MMPs, the NE is capable of cleaving ECM components, specifically elastin and collagens, thereby contributing directly to pathological tissue remodeling in case of increased levels of NEs or uncontrolled activity. Indirectly, NEs are involved in tissue degradation through activation of MMPs (142) and inactivation of its inhibitors (143), like the TIMPs. Further, NE is known to induce mucin secretion through degranulation of secretory cells (144,145). Of note, an overproduction of mucus is a characteristic feature of several chronic lung diseases, e.g. chronic bronchitis, and

conclusively, NE levels were found to be increased in smoker airways with overabundant mucus production (146). Obviously, too high activity of NE induces pathological processes, but low levels or lack of NE have also been reported to be disadvantageous, as they are implicated in the host defense against gram negative bacteria (147). Therefore, it is important to strongly regulate the activity of NE, which is executed by serine protease inhibitors (serpins), e.g. α_1-antitrypsin.

Otherwise, insufficient control of protease activity because of decreased levels of their endogenous inhibitors or because of increased levels of activated proteases results in protease/antiprotease imbalance in the airways, which finally leads to degradation of ECM components and loss of elastic tissue, as seen in an emphysematous lung (**Figure 4**). This balance should be kept for the ratios between MMPs and TIMPs, NE and serpins, caspases and cysteine protease inhibitors (cystatins), as these proteases may be potential contributors in the pathogenesis of COPD.

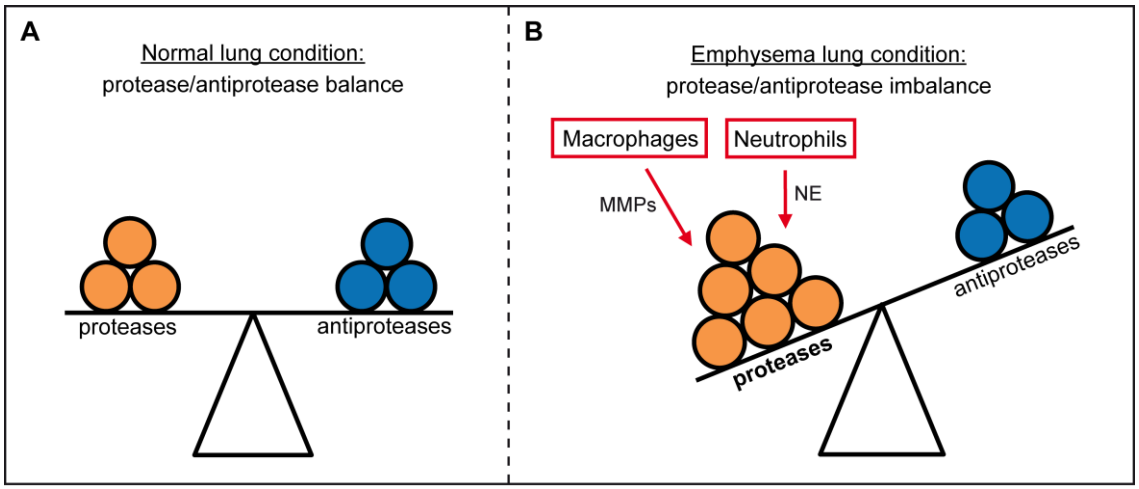

Figure 4. Protease/antiprotease ratios. (A) Proteases and antiproteases are balanced in a normal lung condition. (B) Proteases and antiproteases are imbalanced in favor of the proteases in an emphysema lung condition. Excessive proteases such as MMPs and NE may be secreted by macrophages and neutrophils.

1.4.1.3.3 Oxidant-antioxidant Imbalance

Cigarette smoke, which is known to consist of a huge variety of reactive ingredients (148), and other toxic environmental particles that are daily inhaled, are able to induce the production and release of reactive oxygen and nitrogen species through inflammatory cells in the lungs. This results in a high burden of oxidative stress due to an imbalance between oxidants and the protective antioxidants in favor of the oxidants. Hydrogen peroxide, a commonly used marker to evaluate oxidative stress, has been found in higher

concentrations in exhaled air from COPD patients and during acute exacerbations (149,150), which clearly proofs the critical role of oxidants in COPD pathogenesis. Oxidants can be involved in several COPD relevant processes. Firstly, they trigger the infiltration of inflammatory cells to the lungs and activate them to release further inflammatory mediators or proteolytic enzymes. Oxidants may also induce epithelial cell death, resulting in injuries of lung epithelial cell barriers that are in turn getting more permeable, and are therefore more susceptible to neutrophil infiltration (151). Additionally, antiproteases may be inactivated through oxidation of residues within the active site (152,153), which is favoring the imbalance for proteases. Next, oxidants can also activate Nf-κB (152), a redox-sensitive transcription factor regulating the expression of TNF-α and Interleukin-8, two pro-inflammatory mediators that are clearly linked to COPD, as their levels are increased in sputum of COPD patients (154). Finally, oxidative stress impairs mechanisms of lung repair or hinders protection against inflammation, e.g. it decreases the activity of the transcription factor Nrf2 that is transcriptionally regulating the expression of antioxidants (155). On the other hand, increased oxidative stress might also occur due to decreased levels of antioxidants that are not able to control the high oxidative load sufficiently. In this line, several studies found a deficiency of antioxidants, e.g. thiols, or decreased antioxidant enzyme activity, e.g. of superoxide dismutase, glutathione S-transferase, or glutathione peroxidase in AMΦ from smokers and patients with COPD (156,157). Altogether, the oxidant-antioxidant balance in the lung is one of many important factors to preserve the lungs in a healthy state.

In summary, COPD is caused by the interplay of several different pathomechanisms, i.e. an enhanced chronic inflammation, protease-antiprotease imbalance, oxidant-antioxidant imbalance, and apoptosis (**Figure 5**). In this context, certain immune cells like macrophages, neutrophils and $CD8^+$ T-cells play a pivotal role, as well as their secretions, such as inflammatory mediators (cytokines and chemokines), proteolytic enzymes, antiproteases, oxidants, antioxidants and transcription factors.

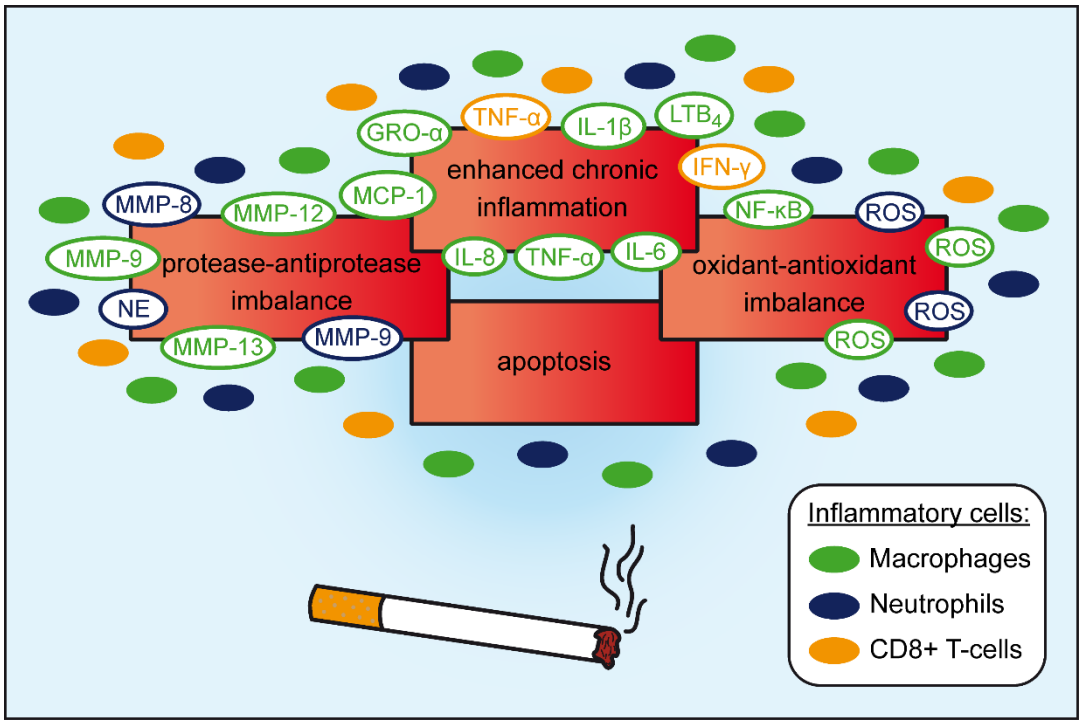

Figure 5. Interplay of pathomechanisms involved in COPD. Pathogenesis of COPD is a result of an interplay between protease-antiprotease imbalance, oxidant-antioxidant imbalance, apoptosis and enhanced chronic inflammation. Several inflammatory cells and their secretions are the driving force for development and progression of the disease. Abbreviations: NE, neutrophil elastase; MCP-1, monocyte chemotactic protein-1; TNF-α, tumor necrosis factor-α; IL, interleukin; MMP, matrix-metalloproteinase; LTB_4, leukotriene B_4; IFN- γ, interferon-γ; NF-kB, nuclear factor kappa B; GRO-α, growth-regulated oncogene-α; ROS, reactive oxygen species.

1.4.1.4 Pathophysiology of COPD

The pathomechanisms described above result in pathological changes of the lung tissue, which then are leading to physiological lung dysfunctions. Two main forms can be divided: chronic (obstructive) bronchitis and emphysema. In clinical terms, they should not be considered separately, because both forms often coexist in COPD patients.

The chronic bronchitis is characterized by a chronic inflammation of the bronchi resulting in a persistent cough with sputum expectoration and excessive mucus production due to hypertrophy of the mucus-producing cells in the airway epithelium (130). The chronic bronchitis may change into a chronic obstructive bronchitis, when additionally large and small airways are narrowed, so that the airflow is substantially impaired. This obstruction may be caused by several factors, e.g. overproduction of mucus that the mucociliary clearance is not able to clear sufficiently; ciliary dysfunctions or loss of cilia resulting in less efficient mucociliary clearance (70); increased activity of the bronchial musculature either directly through inflammatory mediators (e.g. histamine, serotonin), or indirectly through activation of the parasympathicus. All these abnormal structural changes of the

airways are finally leading to a reduced bronchial lumen making airflow more difficult because of an increase of airflow resistance (158).

Emphysema is correlated with a dramatic pathological remodeling or destruction of lung tissue. As described in chapters above, an imbalance between proteases and antiproteases in favor of the proteases is causative for this pathological condition. The remodeling of the lung tissue especially includes the degradation of elastic fibers leading to loss of elasticity and loss of the lung's ability to return to its original state after inspiration (158). In this way, alveolar walls and connective tissue between the alveoli are irreversibly destroyed, which results in enlarged airspaces (130). Summarized, few large airspaces replace many small ones, which massively reduces the surface area of the lungs. This has negative effects on the respiratory function of patients with emphysema. First, small bronchi collapse due to the loss of elastic fibers of their walls that are usually keeping them in an open state (158). This obstruction makes exhalation more difficult. Additionally, after exhalation air remains trapped within the enlarged alveoli. This air does not participate in the gas exchange and prevents enough fresh air to reach the alveoli. Thus, the gas exchange is impaired and emphysema patients have lower blood oxygen levels (158).

1.4.1.5 Symptoms and diagnosis

COPD symptoms include chronic cough and sputum exacerbations on the ground of an excessive production of mucus. Due to the obstructive character and restricted airflow, as well as due to the impaired gas exchange in an emphysematous lung tissue, patients suffer from shortness of breath and fatigue. They may have less energy and are easily becoming tired after physical activity. Low levels of blood oxygen because of an emphysematous lung condition might even lead to blue fingernails. Generally, COPD is a progressive disease, usually starting with mild symptoms, which are getting worse over time, depending on the load of harmful substances one is exposed to.

The Global Initiative for Chronic Obstructive Lung Disease (GOLD) grouped COPD into four severity stages based on a simple lung function test that measures the Forced Expiratory Volume per 1 second (FEV_1) (159). According to this, COPD is mild (i.e. GOLD 1) when $FEV_1 \geq 80\%$, COPD is moderate (i.e. GOLD 2) when $50\% \leq FEV_1 < 80\%$, COPD is severe (i.e. GOLD 3) when $30\% \leq FEV_1 < 50\%$ and COPD is very severe (i.e. GOLD 4) when $FEV_1 < 30\%$. Values indicate percentages of the predicted normal values.

The diagnosis of COPD is very complex, since it includes several tests and is not based on a single finding. Initially, a physician performs an anamnesis by screening symptoms,

sputum, smoking history and by listening to breathing with a stethoscope. Subsequently, pulmonary function tests may be performed to find out if the lungs are working properly. The most common used test is the spirometry, in which lung volumes and speed of inhalation and exhalation are measured, e.g. FEV_1 is used to diagnose COPD and to evaluate its severity as established by GOLD (159). To exclude other diseases that may cause similar symptoms as COPD a radiography of the thorax and analysis of the blood may be performed.

1.4.1.6 Therapy

The main goal of COPD therapy is to slow down the progression of the disease, to relieve symptoms and to minimize exacerbations, thereby increasing the patients' life quality. The main intervention is to reduce harmful influences on the lung, meaning quit smoking or reduction of the exposure to other toxicants. Several studies reported on the efficiency of smoking cessation, as it resulted in significant reductions of morbidity and mortality of COPD (160,161).

The pharmacotherapy of COPD is based on the inhalation of drugs by the use of pressurized metered dose inhalers, nebulizers, or dry powder inhalers. Thereby, drugs are delivered locally to the site of action within the lungs, which enables them to act rapidly, and makes the usage of relatively low doses possible, related with only low incidences of systemic side effects (162). Two main drug classes are available for COPD treatment, i.e. bronchodilators and anti-inflammatory drugs.

Bronchodilators reduce the tone of the airway muscles, which widens the airways and induces resistance to fall (163). Thus, breathing gets easier and more efficient for the patients, which also increases their physical fitness. Substances within the group of bronchodilators are classified due to its mode of action into β_2-agonists, muscarinic-antagonists and theophylline (163,164). The first two are further sub-grouped due to its duration of acting into long-acting β_2-agonists (LABA), e.g. salmeterol, formoterol; short-acting β_2-agonists (SABA), e.g. salbutamol; long-acting muscarinic-antagonist (LAMA), e.g. tiotropium and short-acting muscarinic-antagonist (SAMA), e.g. ipratropium (163,164). While the effect of short-acting agents lasts 4-6 hours and are used on demand to improve symptoms immediately, the effect of long-acting agents lasts 12 hours and longer and are used to provide some basal bonchospasmolysis (163,164). The orally or intravenously applied theophylline has weak spasmolytic and anti-inflammatory effects with a narrow therapeutic range (164). Therefore, it is only used as an alternative medication and in special cases.

Next to bronchodilators, anti-inflammatory drugs, such as glucocorticoids and phosphodiesterase-4 (PDE-4) inhibitors, are used to control and attenuate the inflammation in COPD lungs. Glucocorticoids, e.g. beclomethasone or budesonide, are usually applied through inhalation, except for very severe COPD, in which they might be given systemically, as for prednisolone. Until now, roflumilast was the first and only PDE-4 inhibitor, which received approval for COPD treatment. It is administered orally, but only in a subset of patients suffering from severe COPD and chronic bronchitis to reduce the frequency of exacerbations (165).

According to the GOLD report from 2021 (159), COPD patients are treated with the former described drugs based on disease severity, taking into account the symptoms and exacerbation risk, which classifies patients into groups A to D. Group A patients with a mild form of COPD should be treated with a bronchodilator, either short- or long-acting. Long-acting bronchodilators (LABA or LAMA) are recommended to treat moderate COPD of group B patients, as they are superior to short-acting bronchodilators (166). For the treatment of severe and very severe COPD (groups C and D) associated with two or more moderate exacerbations per year or at least one exacerbation leading to hospitalization, LAMAs are recommended as a basic therapy in preference to LABAs, as LAMAs are more effective in preventing exacerbations (167). In case of still high prevalence of severe symptoms, group D patients might use a combination of a LAMA with a LABA, or a combination of a LAMA with an inhalative glucocorticoid. Generally, the use of short-acting bronchodilators are recommended for patients of all groups, whenever a rapid symptom relief is needed. Finally, patients with arterial hypoxemia (PaO_2 < 55mmHg or SaO_2 < 88%) might need supplemental oxygen therapy (159).

1.5 Aims of the study

The overall aim of this study was to characterize the functional role of endolysosomal cation channels, specifically TRPML3, in toxic chronic lung disease, and to discover its capability as pharmacological drug target. To this end, three main objectives were pursued during the whole study:

1. Determination of TRPML3 expression in the lung
   The aim was to find out in which specific lung cell types TRPML3 is expressed, e.g. certain airway epithelial cells or lung immune cells, in order to deduce possible involvements in physiological or pathological processes in the lungs.

2. Characterization of potential lung phenotypes of *Trpml3*$^{-/-}$ mice

   The aim was to correlate the loss of the TRPML3 channel with potential pathological lung conditions. For this purpose, lung functions measurements were performed of WT and *Trpml3*$^{-/-}$ mice, as the resulting lung function parameters are useful to identify and characterize a phenotypically altered lung.

3. Elucidation of the molecular mechanism underlying the potential lung phenotype of *Trpml3*$^{-/-}$ mice

   The aim was to analyze lung samples, e.g. BAL-F, obtained from WT and *Trpml3*$^{-/-}$ mice in order to detect possible alterations of key mediators or biomarkers that are critical for disease development. Additionally, primary lung cells obtained from WT and *Trpml3*$^{-/-}$ mice were used to perform several cell-based assays to elucidate how TRPML3 is mechanistically involved in the formation and development of the pathological lung phenotype.

2. Material and Methods

2.1 Material

2.1.1 Mouse lines

Designation of mouse lines	Genetic background	Additional information
Trpml3-IRES-Cre/*eR26*-τGFP (1)	Mixed, C57BL/6 and 129/Sv	Kindly provided by Prof. Dr. Ulrich Boehm
Trpml3$^{-/-}$, *Mcoln3*$^{tm1.2Hels}$ (168)	FVB/N	
Trpml3$^{-/-}$, *Mcoln3*$^{tm1.1Jga}$ (32,35)	75% C57BL/6 and 25% Sv129/Ola	Kindly provided by Prof. Dr. Jaime García-Añoveros

Table 1. Mouse lines used in this study.

2.1.2 Cells and cell culture media

Cell culture solutions	Supplier	Product code
Phosphate Buffered Saline (PBS)	Thermo Fisher	14190-094
Dulbecco's Modified Eagle Medium (DMEM)	Thermo Fisher	21063-029
Fetal Bovine Serum (FBS)	Thermo Fisher	10500-064
Penicillin-Streptomycin (Pen-Strep)	Sigma Aldrich	P4333
Roswell Park Memorial Institute (RPMI) 1640 medium	Thermo Fisher	21875-034 11835-030

Table 2. Cell culture media.

Primary cells	Culture media	Supplementation
Alveolar macrophages (AMΦ)	RPMI 1640 or DMEM	10% (v/v) FBS 1% (v/v) Pen-Strep

Table 3. Primary cells.

2.1.3 Chemicals

Chemicals	Supplier	Product code
16% Formaldehyde (w/v), Methanol-free	Thermo Fisher	28906
2-Mercaptoethanol	Merck	M3148
2-Propanol	Carl Roth	CP441.1
4-Methylumbelliferyl N-acetyl-β-D-glucosaminide	Sigma Aldrich	M2133
5-(N-ethyl-N-isopropyl)-amiloride	Sigma Aldrich	A3085
Agar	Merck	05040
Agarose	Carl Roth	3810.3
Ammonium persulfate	Sigma Aldrich	215589
bisBenzimide H33258	Sigma Aldrich	B1155
Boric acid	Carl Roth	5935.1
BSA	Sigma Aldrich	A3294
Collagenase D	Roche	11088858001
DAPI	Thermo Fisher	D1306
DMSO (Dimethyl Sulfoxide)	Corning	25-950-CQC
DNase I, recombinant, Rnase free	Roche	4716728001
Dynasore monohydrate	Sigma Aldrich	D7693
Elastase from porcine pancreas	Sigma Aldrich	45124
Entellan™	Sigma Aldrich	1079600500
Ethanol	Carl Roth	5054.4
Ethylenediamine tetraacetic acid (EDTA)	Carl Roth	8043.1
Fluoromount-G	Biozol	SBA-0100-01
Glycine	Sigma Aldrich	G8898
holo-Transferrin human	Sigma Aldrich	T0665
Hydrochloric acid	Merck	258148
Ionomycin calcium salt	Sigma Aldrich	I0634
Liquid nitrogen (N_2)	Linde	

Methanol	Merck	34860
Methyl-ß-cyclodextrin	Sigma Aldrich	C4555
Paraformaldehyde, 4% in PBS	TissuePro Technology	PFA04-500R
Paraformaldehyde, powder	Thermo Fisher	P/0840/53
Phosphatase Inhibitor Cocktail Tablets	Roche	04906845001
Potassium chloride	Merck	P9541
Potassium phosphate monobasic	Merck	P9791
Protease Inhibitor Cocktail Tablets	Roche	04693132001
Rotiphorese® Gel 30	Carl Roth	3029.1
Skim Milk Powder	Sigma Aldrich	70166
Sodium azide	Merck	S2002
Sodium carbonate	Carl Roth	8563.1
Sodium deodecyl sulfate (SDS)	Carl Roth	2326.2
Sodium hydroxide	Merck	S5881
Sodium phosphate dibasic dihydrate	Merck	71643
Sucrose	Carl Roth	4661.1
TEMED	Carl Roth	2367.1
Tissue-Tek® O.C.T. Compound	Sakura	4583
TRIS base	Sigma Aldrich	T1503
TRIS hydrochloride	Merck	PHG0002
Tri-sodium citrate dihydrate	Carl Roth	4088.1
Triton X-100	Sigma Aldrich	X100
Tween 20	Carl Roth	9127.1
Xylol	Merck	534056

Table 4. Chemicals.

2.1.4 Commercial kits and solutions

Kits and solutions	Supplier	Product code
Desmosine ELISA Kit	Cusabio	CSB-E14196m
Dextran, Alexa Fluor™ 568 conjugate	Thermo Fisher	D22912
Eosin Y-solution 0.5% aqueous	Sigma Aldrich	1098441000
Fixable Viability Dye eFluor™ 780	Thermo Fisher	65-0865-14
GeneRuler 1kb DNA Ladder	Thermo Fisher	SM0311
GoTaq® G2 Hot Start Master Mix	Promega	M7423
Immobilon® Crescendo Western HRP Substrate	Merck	WBLUR0500
LDH Assay Kit	abcam	6593
Light Cycler® 480 SYBR Green I Master Mix	Roche	04707516001
Mayer's hemalum solution	Sigma Aldrich	1092492500
MMP-12 ELISA Kits	Cloud-Clone Corp. abcam	SEA402-Mu-96 213878
MMP-8 ELISA Kit	abcam	206982
PageRuler™ Prestained Protein Ladder	Thermo Fisher	26616
peqGREEN DNA/RNA Dye	VWR, peqlab	37-5010
Protein Assay Dye Reagent Concentrate	Bio-Rad	500-0006
RevertAid First Strand cDNA Synthesis Kit	Thermo Fisher	K1621
RNeasy Plus Mini Kit	Qiagen	74134
SP-D ELISA Kit	abcam	213890
Staining Kit: Verhoeff - van Gieson (VVG)	Morphisto	18553
TIMP-1 ELISA Kit	abcam	196265
TIMP-2 ELISA Kit	abcam	227893

Transferrin from human serum, Alexa Fluor™ 488 conjugate	Thermo Fisher	T13342
UltraComp eBeads™ Compensation Beads	Thermo Fisher	01-2222-41

Table 5. Commercial Kits and solutions.

2.1.5 Buffers/Solutions

Buffers/solutions for molecular biology:

Buffer/Solution	Composition	Application
0.5 M EDTA solution (pH 8)	18.6% (w/v) $Na_2EDTA \cdot 2H_2O$ ~2% (w/v) NaOH in Milli-Q® ultrapure H_2O	Preparation of TBE-buffer (10x)
DNA extraction buffers (mouse tissue)	Alkaline lysis buffer (pH 12): 25 mM NaOH 0.2 mM $Na_2EDTA \cdot 2H_2O$ in Milli-Q® ultrapure H_2O Neutralization buffer (pH 5): 40 mM TRIS-HCl in Milli-Q® ultrapure H_2O	Genotyping
TBE-buffer (10x)	10.8% (w/v) TRIS base 5.5% (w/v) Boric acid 4% (v/v) 0.5 M EDTA solution in Milli-Q® ultrapure H_2O	Gel electrophoresis (genotyping)

Table 6. Buffers/solutions for molecular biology.

Buffers for immunostainings:

Buffer	Composition	Application
DAPI solution	0.2 µg/mL DAPI in PBS (1x)	Staining of cell nuclei
Hoechst solution	2 µg/mL bisBenzimide in PBS (1x)	Staining of cell nuclei
Immunostaining blocking buffer	10% (v/v) donkey serum 3% (w/v) BSA	Blocking of non-specific sites

	0.3% (v/v) Triton X-100 0.05% (w/v) Sodium azide in PBS (1x)	
Normal donkey serum	supplied by Jackson Immunoresearch, 017-000-121	Preparation of blocking buffer
PBS (20x)	3 M NaCl 161 mM $Na_2HPO_4 \cdot 2H_2O$ 39 mM KH_2PO_4 in Milli-Q® ultrapure H_2O	Washing, Preparation of blocking buffer
PBS-T (1x)	5% (v/v) PBS (20x) 0.05% (v/v) Tween 20 in Milli-Q® ultrapure H_2O	Washing of tissue and cells

Table 7. Buffers for immunostainings.

Buffers for FACS analysis:

Buffer	Composition	Application
Digestion buffer for mouse tissue	1 mg/mL collagenase D 0.05 mg/mL DNase I in HBSS	Homogenization of lung tissues
Phosphate Buffered Saline (PBS)	Supplied by Thermo Fisher, 14190-094	Preparation of FACS buffer
eBioscience™ 1x RBC Lysis Buffer	Supplied by Thermo Fisher, 00-4333-57	Lysis of erythrocytes in single cells suspension
FACS buffer	1% (w/v) BSA 0.05% (w/v) Sodium azide in PBS (1x)	Flow cytometry staining buffer
Hank's balanced salt solution (HBSS)	supplied by Thermo Fisher, 14025-050	Preparation of digestion buffer

Table 8. Buffers for FACS analysis.

Buffers for cell-based assays:

Buffer/Solution	Composition	Application
Cell lysis buffer	25 mM HEPES 150 mM NaCl	Hexosaminidase-assay

	0.5% (v/v) Triton X-100 in Milli-Q® ultrapure H_2O	
Citrate-phosphate buffer pH 4.5	17.6 mM $Na_2HPO_4 \cdot 2H_2O$ 11.2 mM Tri-sodium citrate dihydrate in Milli-Q® ultrapure H_2O	Buffer for Hexosaminidase-assay
Glycine buffer pH 10	2 M Na_2CO_3 1.1 M Glycine in Milli-Q® ultrapure H_2O	Stop solution for Hexosaminidase-assay
Glycine-PBS Solution	0.1 M Glycine in PBS (1x)	Transferrin-trafficking assay
HEPES	supplied by Thermo Fisher, 15630-056	LAMP1 translocation assay
HEPES buffered MEM	10 mM HEPES in MEM	LAMP1 translocation assay
Minimum Essential Media (MEM)	supplied by Thermo Fisher, 10370-021	LAMP1 translocation assay

Table 9. Buffers for cell-based assays.

Buffers and solutions for WB analysis:

Buffer/Solution	**Composition**	**Application**
Blocking buffer	5% (w/v) Skim milk powder in TBS-T (1x)	Blocking of membrane
Loading buffer (4x)	10% (v/v) 2-Mercaptoethanol in NuPAGE™ LDS Sample Buffer (4x)	Preparation of samples for protein electrophoresis
Lower gel buffer – Resolving gel buffer (4x), pH 8.8	18.1% (w/v) TRIS-HCl 0.4% (w/v) SDS in Milli-Q® ultrapure H_2O	Preparation of Acrylamide gel
Lysis buffer for protein extraction, pH 8	0.2% (w/v) SDS in 10 mM TRIS-HCl supplemented with proteinase and phosphatase inhibitors	Lysis of AMΦ pellet
NuPAGE™ LDS Sample Buffer (4x)	supplied by Thermo Fisher, NP0007	Preparation of Loading buffer

Ponceau S solution	supplied by PanReac AppliChem, A2935	Staining of proteins on transfer membranes
Running buffer (10x)	14.4% (w/v) Glycine 3% (w/v) TRIS-HCl 1% (w/v) SDS in Milli-Q® ultrapure H_2O	Running buffer for SDS-PAGE
TBS-T (1x)	10% (v/v) TBS buffer (10x) 0.05% (v/v) Tween 20 in Milli-Q® ultrapure H_2O	Wash buffer for membrane
Transfer buffer (10x)	14.5% (w/v) Glycine 3% (w/v) TRIS-HCl in Milli-Q® ultrapure H_2O	Protein transfer from gel to the membrane
Transfer buffer (1x)	10% (v/v) Transfer buffer (10x) 20% (v/v) Methanol in Milli-Q® ultrapure H_2O	Protein transfer from gel to the membrane
TRIS buffered saline (TBS) buffer (10x), pH 7.4	8% (w/v) NaCl 3% (w/v) TRIS-HCl 0.2% (w/v) KCl in Milli-Q® ultrapure H_2O	Wash buffer for membrane
Upper gel buffer – Stacking gel buffer (4x), pH 6.8	6% (w/v) TRIS-HCl 0.4% (w/v) SDS in Milli-Q® ultrapure H_2O	Preparation of Acrylamide gel

Table 10. Buffers and solutions for WB analysis.

2.1.6 Antibodies

Antibodies used for immunofluorescence:

Antibody	Clone	Supplier and product code	Dilution
CD3	Polyclonal	Sigma Aldrich, C7930	1:200
CD45R	RA3-6B2	BD Biosciences, 550286	1:200
CD8α	EPR21769	abcam, 217344	1:500
F4/80	CI:A3-1	AbD Serotec, MCA497G	1:200
LAMP1	1D4B	SantaCruz, 9992	1:200

SFTPC	Polyclonal	Abcepta, AP13684b	1:200
Anti-rabbit-Cy5		Jackson ImmunoResearch, 711-175-152	1:500
Anti-rat-AlexaFluor488		Thermo Fisher, A11006	1:400
Anti-rat-Cy3		Jackson ImmunoResearch, 12-165-153	1:500

Table 11. Antibodies for immunofluorescence.

Antibodies used for Fluorescence activated cell sorting (FACS):

Antibody	**Clone**	**Supplier and product code**	**Dilution**
CD11b	M1/70.15.11.5	Miltenyi Biotec, 130-091-240	1:100
CD11b-BV785	M1/70	Biolegend, 101243	1:100
CD11c	N418	Miltenyi Biotec, 130-119-802	1:100
CD11c-BV605	N418	Biolegend, 117333	1:100
CD24-PerCP/Cy5.5	M1/69	Biolegend, 101823	1:100
CD3-PE/Cy7	17A2	Biolegend, 100219	1:100
CD45	30F11	Miltenyi Biotec, 130-123-900	1:100
CD45-PacBlue	30-F11	Biolegend, 103125	1:100
CD45R/B220-AlexaFluor700	RA3-6B2	Biolegend, 103231	1:100
CD64-APC	X54-5/7.1	Biolegend, 139305	1:100
F4/80	REA126	Miltenyi Biotec, 130-118-466	1:100
Ly-6G-PE/Dazzle™594	1A8	Biolegend, 127647	1:100
MHCII-PE	NIMR-4	SouthernBiotech, 1895-09	1:100
TruStain FcX™	93	Biolegend, 101319	1:100

Table 12. Antibodies for FACS.

Antibodies for Western Blot (WB):

Antibody	Clone	Supplier and product code	Dilution
Anti-mouse IgG, HRP-linked Antibody		Cell Signaling, 7076	1:5000
Anti-rabbit IgG, HRP-linked Antibody		Cell Signaling, 7074	1:5000
ß-actin	13E5	Cell Signaling, 4970	1:1000
TfR	H68.4	Thermo Fisher, 13-6800	1:500

Table 13. Antibodies for WB.

2.1.7 Oligonucleotides

All oligonucleotides were purchased from metabion international AG.

Target structure	Sequence (5' - 3')	Application
Trpml3 WT (*Mcoln3*$^{tm1.2Hels}$)	gaa cac act gac tac ccc caa (sense) tac agt ttt aca gat gtg ttt gag t (antisense)	Genotyping, WT band: 309 bp
Trpml3 KO (*Mcoln3*$^{tm1.2Hels}$)	gaa cac act gac tac ccc caa (sense) aga ggt tca cta gaa cga agt tcc tat tcc (anti-sense)	Genotyping, KO band: 374 bp
Trpml3 WT (*Mcoln3*$^{tm1.1Jga}$)	ctg tga gac ctc tta aca act ct (sense) gtg gag cct tga ctg tct ag (antisense)	Genotyping, WT band: 263 bp
Trpml3 KO (*Mcoln3*$^{tm1.1Jga}$)	ctg tga gac ctc tta aca act ct (sense) ggc aag agc tga gga tat ctt (antisense)	Genotyping, KO band: 443 bp
Actb	cac agc ctg gat ggc tac gt (sense) cta agg cca acc gtg aaa aga t (antisense)	qRT-PCR
Gapdh	cca cca ccc tgt tgc tgt ag (sense) ctc cca ctc ttc cac ctt cg (antisense)	qRT-PCR
Mmp-12	ctg cct cat caa aat gtg cat c (sense), att tgg agc tca cgg aga ctt (antisense)	qRT-PCR

Table 14. List of all murine primers used in this study.

2.1.8 Other materials and equipment

Name	Supplier	Product code
µ-Slide 8 well	ibidi	80826
3R4F Research Cigarettes	Tobacco Research Institute, University of Kentucky	
Atipamezol	Orion Pharma	
Blotting Papers RPTILABO® Thickness 0,75 mm	Carl Roth	0942.1
Embedding cassettes	neoLab	7-0014
Fentanyl	Janssen-Cilag	
Flumazenil	Hexal	
HistoStar™ Embedding Workstation	Thermo Fisher	
Immobilon-FL PVDF Membrane	Merck	IPFL00005
Introcan®-W, 20G	B. Braun	4254112B
Isoflurane (IsoFlo®)	Abbott	
Ketamine 10%	Serumwerk Bernburg AG	
LightCycler® 480 Multiwell Plate 96	Roche	04729692001
LightCycler® 480 Sealing Foil	Roche	04729757001
lumox® multiwell, 96	Sarstedt	94.6120.096
Medetomidine	Orion Pharma	
Microtome Hyrax M55	Zeiss	
Midazolam	Roche	
Naloxone	Actavis	
Peel-A-Way™ embedding molds	Sigma Aldrich	E6032-1CS
Spin Tissue Processor	Thermo Fisher	
Xylazine 20 mg/mL	WDT	

Table 15. Other materials and equipment.

2.1.9 Instruments and software

Instrument and software	Supplier	Application
Axio Scan.Z1 Slide Scanner running ZEN software (blue edition)	Zeiss	Acquiring of immunofluorescence images of lung
BD LSRFortessa II running BD FACSDiva software	BD	Acquiring of FACS data
CaseViewer and Slide Converter	3DHistech	Processing of lung histology images
Computer-assisted stereological toolbox (CAST) software Visopharm Integrator System (VIS)	Visiopharm	Analysis of lung histology images
FlexiVent running Flexiware software	Scireq	Lung function measurements
FlowJo software	FlowJo LLC, BD	FACS data analysis
FLUOstar Omega running Reader Control software	BMG LABTECH	O.D. measurements (ELISA and LDH assay)
GraphPad Prism		Statistical analysis
ImageJ		Quantification of immunofluorescence intensities and western blot bands
Light Cycler 480 running LightCycler 480 software	Roche	qRT-PCR
Microsoft Excel		Calculations of collected data
Mirax Microimaging slide scanner running MIRAXDESK and Mirax viewer software	Zeiss, 3DHistech	Acquiring of lung histology images
Odyssey FC Imaging System running ImageStudio software	LI-COR	Detection of western blot bands
SpectraMax iD3 running SoftMax Pro software	Molecular Devices	ß-Hexosaminidase assay
ZEISS LSM 880 running ZEN software	Zeiss	Acquiring images for Tf-trafficking assay, endocytosis experiment and LAMP1 translocation assay

Table 16. Instruments and software.

2.2 Methods

2.2.1 Mouse lines and animal housing

Two different *Trpml3*$^{-/-}$ mouse lines (*Mcoln3*$^{tm1.2Hels}$ and *Mcoln3*$^{tm1.1Jga}$) were used in this study and were kept in the mouse facilities of the Walther Straub Institute (WSI) of Pharmacology and Toxicology, LMU Munich, and of the Institute of Lung Biology and Disease (ILBD), Helmholtz Centre, Munich. Animals were kept in rooms with constant humidity (45-65%), temperature (20-24°C), and a 12-hour light-dark cycle. Food and water was provided ad libitum. The government of Upper Bavaria had approved all experimental procedures (ROB-55.2-2532.Vet_02-18-6 and ROB-55.2-2532.Vet_02-17-170).

Trpml3-IRES-Cre/*eR26*-τGFP mice were generated as described in Spix et al. (1). They were housed in the barrier rooms of Saarland University's animal facilities and were kindly provided by Prof. Dr. Ulrich Boehm, Saarland University.

2.2.2 Genotyping

For genotyping the mice, ear tissue biopsies were taken at weaning, i.e. 3-4 weeks after birth. The tissue was then dissolved in 75 µL of an Alkaline lysis buffer (pH 12), and subsequently heated at 95°C for ~1 hour until the tissue was visibly decomposed. After cooling of the samples to 4°C, 75 µL of Neutralization buffer (pH 5) was added. See **Table 6** for composition of respective buffers.

For DNA amplification via PCR, obtained DNA samples were mixed with oligonucleotides, RNase-free water and GoTaq® G2 Hot Start Master Mix, containing DNA polymerase, dNTPs and loading dye, as shown in **Table 17** for *Mcoln3*$^{tm1.1Jga}$ and **Table 18** for *Mcoln3*$^{tm1.2Hels}$. Primers were used diluted 1:10 for genotyping of *Mcoln3*$^{tm1.1Jga}$ mouse line and 1:20 diluted for *Mcoln3*$^{tm1.2Hels}$. As the expected WT and KO band sizes for *Mcoln3*$^{tm1.2Hels}$ (309 and 374 bp) are close together, one WT and one KO master mix was prepared to amplify and visualize the respective bands separately. This was not necessary for *Mcoln3*$^{tm1.1Jga}$ mouse line, as the expected band sizes ranged at 263 bp (WT) and 443 bp (KO). The PCR programs used to amplify the DNA products are depicted in **Table 17** and **Table 18**.

Volume [µL] for n=1	Reagents for master mix	PCR program
12.5	GoTaq® G2 Hot Start Master Mix	

2.5	Primer #1 (5'-ctg tga gac ctc tta aca act ct-3')	95°C 2:00 min 95°C 0:30 min 51°C 0:30 min 72°C 1:20 min } 35x 72°C 7:00 min
2.5	Primer #2 (5'-gtg gag cct tga ctg tct ag-3')	
2.5	Primer #3 (5'-ggc aag agc tga gga tat ctt-3')	
1	RNase-free water	
4	DNA sample	

Table 17. Genotyping of *Mcoln3*$^{tm1.1Jga}$.

Volume [µL] for n=1	**Reagents for WT master mix**	**Reagents for KO master mix**	**PCR program**
12.5	GoTaq® G2 Hot Start Master Mix	GoTaq® G2 Hot Start Master Mix	
2.5	Primer #1 (5'-gaa cac act gac tac ccc caa-3')	Primer #1 (5'-gaa cac act gac tac ccc caa-3')	94°C 2:00 min 94°C 0:30 min 59°C 0:30 min 72°C 1:10 min } 35x 72°C 5:00 min
2.5	Primer #2 (5'- tac agt ttt aca gat gtg ttt gag t-3')	Primer #3 (5'- aga ggt tca cta gaa cga agt tcc tat tcc-3')	
2.5	RNase-free water	RNase-free water	
5	DNA sample	DNA sample	

Table 18. Genotyping of *Mcoln3*$^{tm1.2Hels}$.

Agarose gel electrophoresis was used to separate obtained PCR products according to its band sizes. For preparation of the gels, two percent of agarose was suspended in 1x TBE buffer and heated in the microwave until complete dissolution of the agarose. After cooling down to ~50°C, peqGREEN DNA/RNA dye, 1:200000, was added, and the agarose solution was finally cast into gel chambers. After hardening, the gel was loaded with the samples, positive controls obtained from heterozygous, WT and *Trpml3*$^{-/-}$ mice, a negative control containing not DNA but H_2O, and a DNA ladder as a size marker. Gels were run in 1x TBE buffer at a constant voltage of 140V until clear separation of bands as visualized through UV detection using LI-COR Odyssey FC Imaging System. In this

way, the genotype for each mouse was identified based on the respective band sizes of the PCR products in comparison to positive control bands.

2.2.3 Bronchoalveolar lavage (BAL) of mice lungs

2.2.3.1 Isolation of AMΦ for cell-based assays

Female and male mice with an age of 2-6 months were used to perform the bronchoalveolar lavage (BAL) of the lungs. Mice were euthanized by intraperitoneal injection of ketamine/xalazine followed by exsanguination. After opening the peritoneum, the lungs' diaphragm was exposed and cut through to induce the collapse of the lungs. Next, the trachea was exposed by carefully removing the tissue around the trachea, thereby avoiding the injury of any surrounding blood vessels. Using scissors, one short incision was made in the trachea, in-between two rings of cartilage, resulting in a tiny whole. A cannula with a gauge size of 20G was slowly inserted into the trachea and kept in position by the help of sutures. Now, the lungs were lavaged for 7 times with 0.8 mL of ice-cold 1x PBS. That means, after each injection of the 1x PBS into the lung, the injected buffer was carefully aspirated back into the syringes and collected in a falcon tube on ice. This procedure of flushing the lungs and collecting the obtained fluid is called "broncholalveolar lavage". The collected fluid contains cells of the bronchi and alveoli lumen, the vast majority constituting for AMΦ, as well as other secreted and dissociated mediators that may be present in the lung lumen. To receive the AMΦ, the lavage was spun down for 10 min at 4°C and 1000g. The obtained cell pellet was finally re-suspended in 1 mL of RPMI medium containing 10% FBS and 1% Pen-Strep, while the cell-free supernatant (SN), also called BAL-Fluid (BAL-F), was discarded. Before seeding the AMΦ into appropriate well plates for the respective experiments, AMΦ were counted with a hemocytometer to ensure seeding of same numbers of cells in each well.

2.2.3.2 Collection of BAL-Fluid

After centrifugation and separation of the cells, the BAL-Fluid (BAL-F) represents the cell-free SN of the BAL. However, it may contain several secreted mediators that are distributed within the lung lumen and flushed out through the lavage, e.g. inflammatory mediators such as interleukins secreted by AMΦ. Thus, BAL-F samples were collected to analyze its composition, as well as concentrations of selected mediators by enzyme-linked immunosorbent assay (ELISA). Basically, to obtain BAL-F samples the same protocol was applied as described above for the isolation of AMΦ, except for two deviations.

Instead of washing the lungs 7 times with 0.8 mL of 1x PBS, only 3 washes were performed using 0.5 mL of 1x PBS, each, to reduce the volume and concentrate dissolved analytes inside. Additionally, after centrifugation of the lavage, the BAL-F was separated into 1.5 mL tubes, while the AMΦ pellet was discarded or used for another experiment. After shock freezing the BAL-F samples in liquid nitrogen, they were stored in the -80°C freezer until usage.

2.2.4 Cell-based experiments

2.2.4.1 Intracellular trafficking

Isolation of AMΦ from WT and *Trpml3*$^{-/-}$ mouse lungs was performed as described previously in chapter 2.2.3.1. They were seeded in phenol-red free DMEM containing 10% FBS and 1% Pen-Strep, in wells of a 24 well plate onto 12 mm coverslips. After 24 hours, cells were strongly attached to the coverslip and the assay was carried out. Firstly, cells were washed and exposed to a 10 min incubation on ice. The cooling ensures blockage of all other endocytosis pathways except from receptor-mediated endocytosis, through which transferrin (Tf) is taken up into the cell. After one 1x PBS-wash, cells were pulsed for 20 min at 37°C using 20 µg/mL Tf-Alexa Fluor™ 488 conjugate in serum-free DMEM. Then, cells were thoroughly washed thrice using 0.1 M glycine-PBS to completely remove or quench any left fluorescent conjugate. Then, trafficking of transferrin was chased by incubating the cells in complete media supplemented with 20 µg/mL unlabeled transferrin for several time periods (0, 5, 10, 15 and 20 min) before fixation of the cells using ice-cold, 4% PFA for 10 min. The treatment with unlabeled transferrin ensures the continuous internalization of the transferrin receptors, thereby keeping the recycling process going. Finally, the nuclei were stained for 10 min in DAPI solution, 0.2 µg/mL. After washing of cells with 1x PBS, the coverslips and adherent AMΦ were mounted onto microscope slides. Pictures were acquired using Zeiss LSM880, and a 40-x objective lens. The mean intracellular fluorescence intensity for each timepoint was measured using ImageJ.

2.2.4.2 β-Hexosaminidase release

Isolation of AMΦ from WT and *Trpml3*$^{-/-}$ mouse lungs was performed as described previously in chapter 2.2.3.1. About 60000 cells were seeded per well using 96 well plates and RPMI complemented with 10% FBS and 1% Pen-Strep. On the following day, AMΦ were treated with 4 µM ionomycin (positive control) for 10 min, 10 µM ML3-SA1 for 60

min or DMSO (vehicle control) for 60 min in phenol-red free and serum-free DMEM. After the respective incubation times, the SN of each well was collected and preserved on ice. Retained cells were lysed for 30 min on ice using lysis buffer (see **Table 9**). After centrifugation of the SN and lysates (10 min at 130000 rpm, 4°C), all samples were incubated with 4-Methylumbelliferyl N-acetyl-β-D-glucosaminide (MUF), 1 mM in sodium citrate-phosphate buffer (see **Table 9**) for 30 min at 37°C. Cells were incubated in wells of a black lumox® multiwell, 96. Through addition of glycine buffer (see **Table 9**), the reaction and turnover of MUF through β-hexosaminidase enzyme was stopped. Fluorescence intensities of all samples were measured using a SpectraMax iD3 plate reader and excitation/emission wavelengths of 365/450 nm. The β-hexosaminidase release was calculated as percentage release of total level of β-hexosaminidase measured in both SN and lysates.

2.2.4.3 Lysosomal-associated membrane protein (LAMP) 1 translocation

Isolation of AMΦ from WT and *Trpml3*$^{-/-}$ mouse lungs was performed as described previously in chapter 2.2.3.1. Cells were plated at a confluence of 20000 cells/well using ibidi µ-Slide 8 well plates and left overnight to attach to the well bottoms. Then, AMΦ were treated at 37°C with 4 µM ionomycin (positive control) for 10 min, 30 µM ML3-SA1 for 60 and 120 min or DMSO (negative control) for 120 min, all prepared in MEM containing 10 mM HEPES. Next, cells were washed, kept on ice and incubated with LAMP1-antibody, diluted at 1:200 in MEM supplemented with 1% BSA and 10 mM HEPES. The incubation was conducted for 20 min on ice. Thereafter, cells were fixed using methanol-free PFA 4% for 20 min followed by incubation for one hour with AlexaFluor 488 conjugated secondary antibody, diluted at 1:400 in 1x PBS complemented with 1% BSA. Nuclei were stained using DAPI solution, 0.2 µg/mL, for 10 min. Images were taken using the LSM880 confocal microscope and the 40-x objective lens and processed using ImageJ and ZenBlue software.

2.2.4.4 Dextran uptake

Isolation of AMΦ from WT and *Trpml3*$^{-/-}$ mouse lungs was performed as described previously in chapter 2.2.3.1. About 20000 cells per well were seeded in phenol-red free DMEM complemented with 10% FBS and 1% Pen-Strep, using ibidi µ-Slide 8 well plates. On the following day, AMΦ were washed and incubated with Alexa Fluor™ 568 conjugated dextran in dye- and serum-free DMEM, 50 µg/mL, at 37°C for several times. Incubation periods were 5, 10, 15, 20 and 30 min, while control cells were kept untreated in

dye- and serum-free DMEM (0 min dextran incubation). Afterwards, cells were thoroughly washed with 1x PBS, followed by fixation using ice-cold PFA 4% and staining of nuclei using 0.2 µg/mL DAPI solution, for 10 min respectively. Images were acquired on a LSM880 using a 40-x objective lens. Amounts of absorbed dextran at different timepoints were evaluated by measuring the intracellular fluorescence intensity using ImageJ.

2.2.4.5 Lactate Dehydrogenase (LDH) toxicity

Isolation of AMΦ from WT and *Trpml3*$^{-/-}$ mouse lungs was performed according to chapter 2.2.3.1. Then, cells were plated in wells of a 96 well plate, ~60000 cells/well, using phenol-red free RPMI complemented with 10% FBS and 1% Pen-Strep. On the next day, AMΦ were washed and incubated overnight with 30 µM ML3-SA1 or DMSO control. After the incubation, the SN was collected from each well in tubes and centrifuged at 600g for 10 min to remove dead cells and debris. Samples were subsequently mixed with LDH reaction mix containing WST substrate in wells of a 96 well plate as defined in the instruction of the manufacturer. The LDH enzyme from dead cells oxidizes lactate and generates NADH, which reacts with WST substrate to form a medium coloring product. The SN obtained from cells exposed to lysis buffer served as a positive control. The optical density of all samples was measured at 450 nm (reference wavelength at 650 nm) using FLUOstar Omega plate reader.

2.2.5 ELISA of BAL-F and AMΦ SN

2.2.5.1 ELISA of BAL-F

BAL-F was obtained from WT and *Trpml3*$^{-/-}$ mouse lungs as described previously in chapter 2.2.3.2. Frozen samples were thawed on ice and were subsequently analyzed undiluted through standard sandwich ELISA technology (**Table 19**), as defined though the instructions provided by the manufacturer. The optical density at 450 nm was measured using FLUOstar Omega plate reader and concentrations were calculated utilizing calibration curves obtained from respective standard proteins. With that, TIMP-1/2, MMP-12, desmosine, and SP-D levels were determined.

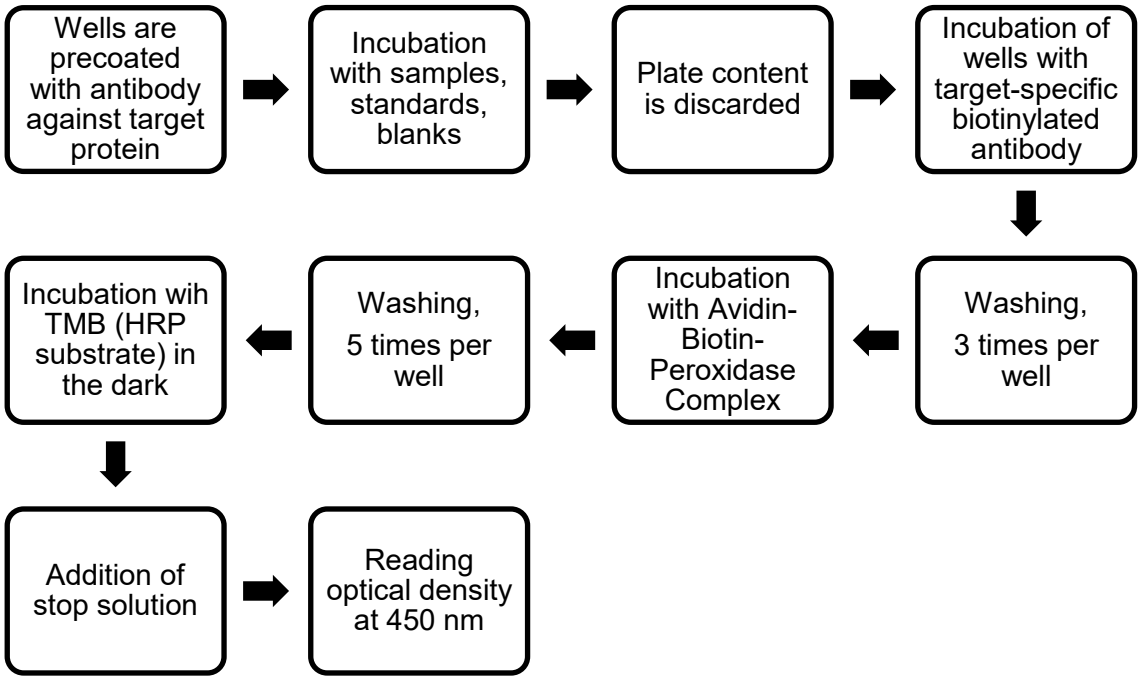

Table 19. Standard protocol for sandwich ELISA.

2.2.5.2 ELISA of AMΦ SN

Isolation of AMΦ from WT and *Trpml3*$^{-/-}$ mouse lungs was performed according to chapter 2.2.3.1. Lavage obtained from mice within its genotypic group were combined, because high numbers of cells were required. Hence, 100000 cells/well were seeded on a 96 well plate, in phenol-red free RPMI containing 10% FBS and 1% Pen-Strep. The following day, cells were washed and fresh media was provided, 200 µL per well of dye-free RPMI complemented with 10% FBS, 1% Pen-Strep, and a protease inhibitor (PI) cocktail. AMΦ were then kept in culture for 72 hours. Afterwards, the SN from each well was collected in tubes and cooled on ice, followed by centrifugation at 11000g and 4°C for 10 min to discard debris and dead cells. Samples were then frozen in liquid nitrogen before storing them at -80°C freezer until its usage for MMP ELISAs. On the day of the experiment, samples were thawed on ice and MMP-12 and MMP-8 concentrations were measured through standard sandwich ELISA technology (**Table 19**) according to the protocol provided by Abcam (ab206982 and ab213878). Samples were diluted 1:1 for the assay. Values for absorbance were read at 450 nm using FLUOstar Omega plate reader. The concentrations of MMPs were calculated using calibration curves obtained from respective standards, as defined by the manufacturer's instruction protocol.

For endocytosis inhibition or activation of TRPML3, WT and *Trpml3*$^{-/-}$ AMΦ were treated using several endocytosis blockers (4 hours, at 37°C) after the culture period of 72 hours, or with TRPML3 agonist (overnight, at 37°C) starting 48 hours beyond culturing the cells.

MBCD at 2.5 mg/mL was used to inhibit clathrin-independent endocytosis, Dyn at 50 µg/mL was used to block clathrin-mediated endocytosis, EIPA at 150 µM was applied as a blocker for macropinocytosis and 30 µM ML3-SA1 was used to activate TRPML3. DMSO was used as a basal control. Additionally, a blank control was processed in parallel for every condition, i.e. wells containing no cells but media and inhibitor/agonist/DMSO. After respective incubation times, SNs were collected in tubes on ice. Further sample processing and measurement of MMP-12 in the SN through ELISA were conducted as described in the paragraph above.

2.2.6 Immunostainings of lung tissue cryosections and lavage cells

Immunostainings were performed of lavage cells and lung tissue cryosections obtained from adult female *Trpml3*-IRES-Cre/*eR26*-τGFP mice which were euthanized through intraperitoneal (i.p.) injection of ketamine/xylazine.

For cryosections, mice were transcardially perfused with 1x PBS, followed by 4% PFA solution. Lungs were removed and subjected to a post-fixation in 4% PFA for 2-4 hours. After an overnight incubation in 18% sucrose solution for the purpose of cryoprotection, lung tissues were embedded in plastic cryomolds and frozen in Tissue-Tek. Next, 10 µm lung tissue cryosections were prepared and transferred onto microscope slides. For subsequent immunostainings, tissue cryosections were shortly air-dried and rinsed 3 times for 5 min in 1x PBS. After 1 hour of incubation in blocking buffer (see **Table 7** for composition), tissue sections were incubated with the primary antibodies overnight at 4°C. The following antibodies and dilutions were used: anti-mouse SFTPC (1:200), anti-mouse F4/80 (1:200), anti-mouse CD3 (1:200), and anti-mouse CD8α (1:500), and anti-mouse CD45R (1:200). The following day, the slices were rinsed 3 times for 5 min in 1x PBS-T and incubated with the secondary antibodies, anti-rabbit-Cy5 or anti-rat-Cy3, diluted at 1:500, for 2 hours at room temperature (RT). Nuclei were stained for 5 min using 2 ug/mL bisBenzimide solution followed by 3 times for 5 min for final washes in PBS-T and mounting in Fluoromount-G. Immunofluorescence images were taken using AxioScan.Z1 slide scanner and processed with ZenBlue software.

For immunostainings of lung lavage, cells were isolated from *Trpml3*-IRES-Cre/*eR26*-τGFP mice through bronchoalveolar lavage (BAL) as delineated in chapter 2.2.3.1. Cells were seeded in ibidi µ-Slide 8 wells in dye-free RPMI complemented with 10% FBS and 1% Pen-Strep. Post attachment to wells, cells were rinsed with 1x PBS and fixed in 4% PFA solution for 10 min on ice. All subsequent blocking, washing, and staining steps were performed as described above for lung tissue cryosections. Afterwards, cells were

stained with the primary antibody, anti-mouse F4/80 (1:200), followed by the secondary antibody, anti-rat-Cy3 (1:500). Nuclei staining was performed using 0.2 µg/mL DAPI solution. Immunofluorescence images were taken using a LSM 880 and processed with ZenBlue software.

2.2.7 Fluorescence-activated cell sorting (FACS)

FACS analysis was conducted of lung tissue and lung lavage isolated from *Trpml3*-IRES-Cre/*eR26*-τGFP mice that were euthanized by isoflurane inhalation. First, cells of the alveoli were isolated by BAL as described in 2.2.3.1, and kept on ice until further processing. After perfusion of the lungs with ~20 mL of ice-cold 1x PBS, lung tissues were dissected out and minced into small pieces <1 mm using feather scalpels. Lung tissues were then transposed into 1.5 mL tubes containing 700 µL digestion buffer (see **Table 8** for composition). Digestion was performed for 30 min at 37°C. The digested tissue was filtered through nylon strainers (100 µm and 30 µm) using syringe plungers. Filters were washed 3 times with 10 mL of 1x PBS and the resulting suspension was spun down at 400g for 5 min. The lavage collected at the start was centrifuged as well, at 1000g for 10 min. To remove erythrocytes, all cell pellets were incubated with 3 mL of eBioscience™ 1x RBC Lysis Buffer for 3 min followed by another centrifugation step for 5 min at 400g. Cells were washed with 1 mL of FACS buffer (see **Table 8** for composition) and incubated in 100 µL of the same buffer, supplemented with CD16/32 antibody for Fc blocking, for 10 min at 4°C. After another washing step, cells were eventually incubated with 100 µL of the staining master mix, containing viability dye, 1:1000, and several fluorochrome-conjugated antibodies. Antibodies were used in a dilution of 1:100 and are listed in **Table 12**. After 20 min of incubation at 4°C, cells were repeatedly rinsed with 1 mL of FACS buffer before re-suspension in 300 µL. Samples were kept on ice, protected from light until final measurements. To correct for spectral overlap, compensation controls were prepared simultaneously for each fluorophore using UltraComp eBeads™ compensation beads, and run on a BD LSR Fortessa II. After fluorescence compensation, samples were finally run on the flow cytometer and collected data were analyzed using FlowJo. This protocol was applied for five *Trpml3*-IRES-Cre/*eR26*-τGFP mice, as well as five regular mice free of τGFP expression, which were utilized to create a threshold value for τGFP+ cells.

2.2.8 Quantitative real-time PCR (qRT-PCR)

AMΦ were isolated by BAL as described in chapter 2.2.3.1 and obtained cell pellets were used for isolation of total mRNA using the RNeasy Plus Mini Kit as per the manufacturer's protocol. Total mRNA concentrations were determined using a NanoDrop™ UV-Vis spectrophometer. The same amounts of mRNA from each sample were used for subsequent complementary DNA (cDNA) synthesis using the RevertAid First Strand cDNA Synthesis Kit according to the manufacturer's protocol. Then, master mixes were prepared on ice for each gene (*Mmp-12*, *Gapdh*, *Actb*) containing Light Cycler® 480 SYBR Green I Master Mix, the respective primer mix (1:10 dilution) and nuclease free water. Primers were constructed with Primer-Blast software and no off-target bindings were predicted. The sequences of all used primers are shown in **Table 14**. Finally, 2.5 µL of cDNA sample and 7.5 µL of master mix were pipetted into the wells of a LightCycler® 480 Multiwell Plate. Negative controls containing no cDNA, only nuclease free water, were processed in parallel to ensure the specificity of the primers. Triplicates were prepared for each sample. The plate was spun down at 3000 rpm for 10 seconds and proceeded by the run on a LightCycler® 480 system. Relative mRNA expression was calculated according to the comparative ΔC_T method (169) and using the formula: Relative mRNA level = $2^{-\Delta CT}$ with $\Delta C_T = C_T$ (target) – C_T (reference) and C_T = cycle threshold. *Gapdh* and *Actb* served as reference genes.

2.2.9 Protein analysis using western blot (WB) technique

2.2.9.1 Protein extraction from AMΦ and sample preparation

AMΦ cell pellets were isolated from WT and *Trpml3*$^{-/-}$ mice through BAL as described previously in chapter 2.2.3.1. Cell pellets were lysed using 10 mM TRIS-HCl lysis buffer containing 0.2% SDS and supplemented with proteinase (1x) and phosphatase (1x) inhibitors. To achieve total cell lysis and to shear DNA to reduce viscosity, samples were subjected to ultrasonication on ice. Protein concentrations were subsequently determined using the Bradford method. The absorbance shift of the dye Coomassie brilliant blue G-250 after binding to sample proteins was measured and correlated to total protein concentrations based on a BSA standard curve that was recorded in parallel. The Bradford assay was performed according to the protocol supplied with Protein Assay Dye Reagent Concentrate from Bio-Rad. To reduce and denature samples, 4x Loading buffer (see **Table 10** for composition) was added to each sample that were subsequently boiled at 95°C for 5 min.

2.2.9.2 SDS-Polyacrylamid Gel Electrophoresis (SDS-PAGE)

SDS-PAGE was used to separate sample proteins pursuant to their molecular weight. The polyacrylamide gels were prepared consisting of a resolving gel at the bottom for optimal separation of proteins and a stacking gel on top to concentrate the proteins and ensure the same starting point for entering the resolving buffer. The pore size of the polyacrylamide gel is variable and can be adjusted according to the sample proteins. For separation of 90 kDa transferrin receptor protein, a 10% polyacrylamide gel was used as it is appropriate to resolve proteins with sizes of 15-100 kDa.

First, the resolving gel solution was prepared according to the composition depicted in **Table 20** and carefully poured into the gap between the glasses of the gel preparation apparatus. After 20 min of time for the polymerization of the resolving gel, the stacking gel solution was prepared (**Table 20**) and cast on top of the resolving gel. Finally, the comb was inserted and the gel was given 15-20 min to polymerize.

Solution	Composition per gel
Stacking gel, 6% poly-acrylamide	5.4 mL dH_2O 2.0 mL Rotiphorese® Gel 30 2.5 mL Stacking gel buffer (see **Table 10**) 50 µL 10% APS in dH_2O 13 µL TEMED
Resolving gel, 10% poly-acrylamide	4.1 mL dH_2O 3.3 mL Rotiphorese® Gel 30 2.5 mL Resolving gel buffer (see **Table 10**) 50 µL 10% APS in dH_2O 13 µL TEMED

Table 20. Preparation of polyacrylamide gel.

The polyacrylamide gel was arranged within the holder of the electrophoresis chamber, which was filled with 1x running buffer (see **Table 10** for composition). The comb was carefully removed and samples were loaded into the gel wells, according to their protein amount. 4 µL of PageRuler^{TM} Prestained Protein Ladder was loaded as reference. The gel was run at 80V until appropriate separation of proteins visualized through the colored marker proteins.

2.2.9.3 Western blot (WB)

In a following step, the separated proteins were transferred onto an Immobilon-FL polyvinylidine difluoride (PVDF) membrane. For that, the membrane was first immersed in methanol and subsequently rinsed with 1x Transfer buffer (see **Table 10** for composition). Then, the sandwich was prepared consisting of sponges at the outermost followed by filter papers enclosing the gel and membrane in the middle. The sandwich was set into the pre-cooled transfer tank with the orientation that the negatively charged proteins from the gel are pulled to the positively charged anode, thereby moving into the PVDF membrane. The tank was filled with precooled 1x Transfer buffer. The blotting took place at 100V for 1 hour. To control for complete transfer of the proteins, the dried membrane was stained with Ponceau-S solution. After location of the reddish-pink stained protein bands, the staining was removed through several washes with 1x TBS-T.

2.2.9.4 Detection of proteins through immunostaining

For the detection of distinct protein bands through immunostainings, the membrane was first blocked with a solution of 5% milk powder in TBS-T, for 1 hour at RT. Membranes were then incubated with the specific primary antibodies diluted in blocking buffer, overnight at 4°C on a shaker (see **Table 13** for dilution ratios). After three washes with 1x TBS-T, each 10 min, at RT on the shaker, the membrane was incubated with HRP-conjugated secondary antibody diluted in TBS-T containing 1% BSA (see **Table 13** for dilution ratios). The incubation was performed for 1 hour at RT on the shaker. Next, the membrane was again rinsed, twice with TBS-T for 5 min each, lastly once with 1x PBS for 5 min. Membranes were incubated with Immobilon® Crescendo Western HRP Substrate in the dark for 0.5-1 min for the detection of the chemiluminescence signal on the LI-COR Odyssey® FC imaging system. ImageJ was used to measure protein band intensities.

2.2.10 Animal experiments

Animal experiments were performed in cooperation with Dr. Önder Yildirim, Institute of Lung Biology and Disease (ILBD), Helmholtz Centre Munich. All handling, breeding and experimental proceedings were in strict conformance with all relevant ethical regulations and were approved by the government of Upper Bavaria.

2.2.10.1 Elastase-induced emphysema model

For the induction of lung emphysema through elastase application, female WT vs. *Trpml3*$^{-/-}$ mice with an age of 4-5 months were used. Mice were anesthetized through an

i.p. injection of a mixture of Fentanyl (50 µg/kg), Midazolam (5 mg/kg), and Medetomidine (500 µg/kg), according to the body weight of each mouse. Porcine pancreatic elastase, 20 U/kg body weight in a volume of 80 µL, was applied oropharyngeally, i.e. the elastase solution was dropped onto the oropharynx, while the tongue was pulled out and hold with forceps, and while the nostrils were blocked using forceps. This position was kept for ~5 seconds to ensure that the treated mice were unable to swallow or breathe through the nose, while the elastase solution was inhaled into the lower respiratory tract. Control mice were applied 80 µL of PBS through the same route. After the application, narcosis was antagonized through a subcutaneous injection of a mixture of Naloxone (1200 µg/kg), Flumazenil (500 µg/kg) and Atipamezol (2.5 mg/kg), and according to the body weight of each mouse. All mice were analyzed 21 days after the elastase application. Lung function measurements were performed, BAL-F was collected and left lungs were taken for histological analysis.

2.2.10.2 COPD mouse model – Exposure to tobacco smoke

To induce COPD, female WT vs. *Trpml3*$^{-/-}$ mice with an age of 4-5 months were used. The animals were exposed to cigarette smoke (CS) in whole body chambers for 50 min (= 10 cigarettes) twice per day over a time range of 2 months. A break of 3 hours was kept between the two applications per day. The CS was generated from filter-free 3R4F Research Cigarettes and directed into the exposure chambers by the use of membrane pumps. The total particulate matter (TPM) of the CS exposure were 500mg/m^3, constituting the sum of all particle burden of the exposure air. The TPM level was monitored on a regular basis through weighing quartz fiber filters, sampled with air from the chamber before and after the exposure, and referring the obtained particle mass to the total air volume. A GCO 100 CO Meter (Greisinger) was used to monitor CO concentrations of the air in the exposure chamber. Control mice were exposed to filtered air (FA). After 2 months of treatment all mice were analyzed for lung function and left lungs were taken for histological analysis.

2.2.10.3 Lung function measurements

Mice were deeply narcotized using a mixture of xylazine (0.7 mg/kg) and ketamine (100 mg/kg), according to the body weight of each mouse. The depth of anesthesia was confirmed by the absence of any reflexes. Then, the trachea was exposed, intubated through a small cut made between the cartilage rings and finally connected to the flexiVent^{TM} (Scireq) for mechanical ventilation with a tidal volume of 10ml/kg at a frequency of 150

breaths/min. For maintenance of a normal body temperature, mice were lying on a heating plate during the measurement.

By the use of a predefined script, the flexiVent™ applied several maneuvers to measure various lung function parameters. This included the Single Frequency Forced Oscillation Technique (FOT) providing the parameters Elastance (E), dynamic Compliance (C), and Resistance (R); Broadband (multi-frequency) FOT giving information about the Tissue Elasticity (H), Tissue Damping (G), and Airway Resistance (Rn); Deep Inflation estimating the Inspiratory Capacity (IC); and Pressure-volume loops that capture Total Lung Capacity (A), and the Quasi-static Compliance (Cst). An illustration of some maneuvers is shown in **Figure 6**. The predefined script took four readings per animal.

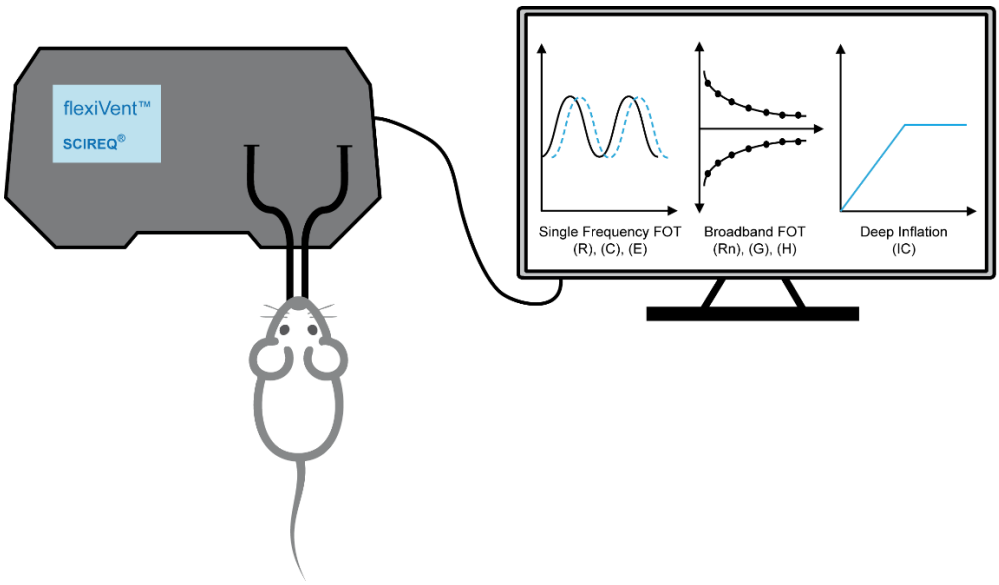

Figure 6. Illustration of lung function measurements using the flexiVent™. Different maneuvers are applied providing several respiratory mechanics parameters: Single Frequency Forced Oscillation Technique (FOT) provides (R), (C) and (E), Broadband FOT provides (Rn), (G) and (H), and Deep Inflation provides (IC).

2.2.11 Histological analysis of lung tissue

2.2.11.1 Lung tissue processing

After lung function measurements, mice were killed through exsanguination. BAL was performed for the collection of BAL-F. Subsequently, left lung lobes were fixed through an intratracheal instillation of ice-cold, 4% PFA solution. The instillation was performed at a constant pressure (20cm fluid column). After 10 min, left lungs were dissected out and transferred into falcon tubes for another 24h-post-fixation in 4% PFA solution. On the next day, lungs were embedded in 2% Agar. From the resulting Agar block containing

the lung tissue, 4 mm thick sagittal slices were prepared, placed side by side into small caskets and overlaid with liquid, 2% Agar solution. The hardened block was finally placed into embedding cassettes and washed with tap water. In the following, the Agar-embedded lung tissue slices were dehydrated using a row of different percent Ethanol (ascending from 70% to 100%), followed by Xylol and incubation in paraffin, as shown in **Table 21**. The dehydration and incubation in paraffin was performed overnight using a Spin Tissue Processor that is automatically transferring the samples from one medium to the next one.

Order	Medium	Time [hour]
1	70% Ethanol	1
2	80% Ethanol	1
3	96% Ethanol	1
4	96% Ethanol	2
5	96% Ethanol	2
6	100% Ethanol	1
7	100% Ethanol	2
8	100% Ethanol	2
9	Xylol	1
10	Xylol	2
11	Paraffin	1
12	Paraffin	2

Table 21. Dehydration protocol of lung tissue.

Next, the lung tissue blocks from the paraffin container were placed into steel molds and poured over with liquid paraffin (60°C) using an Embedding Workstation. The molds were kept on a cooling plate until the paraffin was completely hardened. The paraffin blocks containing the lung tissue were stored at 4°C until proceeding with the preparation of paraffin slices. For that, the paraffin blocks were clamped into a cooled holder of a rotary microtome and 3 µm slices were prepared. After stretching the paraffin sections in water at 40°C, the slices were transferred onto microscope slides. The slides were dried overnight at 37°C to be stained on the day after.

2.2.11.2 Hematoxylin & Eosin (H&E) staining

Firstly, all paraffin slices needed to be transferred to an aqueous milieu, carried out by using Xylol and Ethanol with descending percentages (100% to 70%), according to the following protocol (**Table 22**).

Order	Medium	Time [min]
1	Xylol	5
2	Xylol	5
3	100% Ethanol	1
4	100% Ethanol	1
5	90% Ethanol	1
6	80% Ethanol	1
7	70% Ethanol	1
8	dH_2O	1
9	dH_2O	1

Table 22. Hydration of paraffin slices.

Post hydration, paraffin slices were incubated for certain periods in different media, as listed chronologically in **Table 23**. Hematoxylin and Eosin stain nuclei dark-blue to dark-purple, cytoplasma pink to red and other intercellular substances e.g. collagen of the ECM appear pink to red, as well.

Order	Medium	Time [min]
1	Mayer's hemalum solution	5
2	Tap water	Brief immersion
3	0.1% HCl-Ethanol	Brief immersion
4	Tap water	5-10
5	dH_2O	5-10
6	0.5% Eosin Y-solution	8

Table 23. Hematoxylin & Eosin (H&E) staining protocol.

Following the H&E staining protocol, all slices were dehydrated again, performed according to the protocol depicted in **Table 24**. After the last incubation step in Xylol, lung tissue slices were mounted using Entellan™ and subsequently air-dried under the hood, overnight, before proceeding with the microscopic analysis of airspace enlargements.

Order	Medium	Time [min]
1	70% Ethanol	Brief immersion
2	80% Ethanol	Brief immersion
3	90% Ethanol	Brief immersion
4	96% Ethanol	Brief immersion
5	100% Ethanol	1
6	100% Ethanol	1
7	Xylol	5
8	Xylol	5

Table 24. Dehydration of paraffin slices after H&E staining.

2.2.11.3 Verhoeff-van Gieson (VVG) staining

For VVG stainings, lung tissue slices were initially transferred to an aqueous milieu using the protocol shown in **Table 23**. Then, the VVG staining kit supplied by Morphisto was used to stain the connective tissue of lung slices according to the protocol of **Table 25**. Thereby, elastic tissue was stained blue-black, collagen fibers red and other tissue elements yellow.

Order	Medium	Time [min]
1	Verhoeff staining solution (Mixture of solutions A:B:C with a ratio of 3:2:1, freshly prepared)	15
2	$FeCl_3$ solution, 1%	0.5
3	Tap water	8
4	96% Ethanol	1
5	Van Gieson's picrofuchsin	2
6	dH_2O	Brief immersion

Table 25. Verhoeff-van Gieson (VVG) staining protocol.

Afterwards, the slices were dehydrated through the following protocol (**Table 26**), before the lung tissue was finally mounted in Entellan™. Slices were air-dried and the numbers of elastin fibers were analyzed using an Olympus BX51 light microscope and a 40-x objective.

Order	Medium	Time [min]
1	96% Ethanol	1.5
2	96% Ethanol	2
3	Isopropanol	5
4	Xylol	5
5	Xylol	5

Table 26. Dehydration of paraffin slices after VVG staining.

2.2.11.4 Quantification of airspace enlargements

Quantification of airspace enlargements was performed using H&E stained lung tissue slices and an Olympus BX51 light microscope provided with a computer-assisted stereological toolbox (CAST). It allows the quantification of 3D geometric characteristics, e.g. analysis of the lengths of airspaces as mean linear chord length (MLI). In order to do that, the CAST software has randomly picked 30 fields of view per lung. The lung sections were then overlaid with a grid of lines. In the following, two parameters were analyzed, first the intercepts of lines with alveolar septa (I_{septa}) were counted, and second the counts of points located within airspaces (P_{air}) were determined. MLI was then calculated using the formula $MLI = \Sigma P_{air} \times L(p) / \Sigma I_{septa} \times 0.5$. L(p) is the line length/point, which was 88.08 µm. In this manner, the MLI was calculated for each mice from the elastase and tobacco smoke experiment.

3. Results

3.1 TRPML3 expression in the murine lung

To analyze TRPML3 expression in the murine lung, a *Trpml3*-IRES-Cre/*eR26*-τGFP reporter mouse line was used (1), in which TRPML3-expressing cells are visualized through cellular expression of τGFP. The fusion of GFP with the microtubule-associated protein Tau (τ) enables labeling of axons (170,171). Immunostainings of lung tissue cryosections and of BAL cells were performed, as well as FACS analysis of whole lung tissue and of lavage cells.

3.1.1 Immunostainings of tissue and BAL cells from *Trpml3*-IRES-Cre/*eR26*-τGFP mouse lungs

For immunostainings of lung tissue cryosections, several antibodies were used to detect various lung cells. F4/80 was used as a marker for macrophages, CD3 for T-cells, SFTPC for AT2 cells, CD45R for B-cells, and CD8α for cytotoxic T-cells. Co-localization of τGPF with the respective cell markers indicate TRPML3 expression in this cell type. As depicted in **Figure 7**, a high degree of co-localization was seen for macrophages, whereas AT2 cells and T-cells clearly showed lower rates of co-localization. Nearly no co-localization was detectable for B-cells and cytotoxic T-cells.

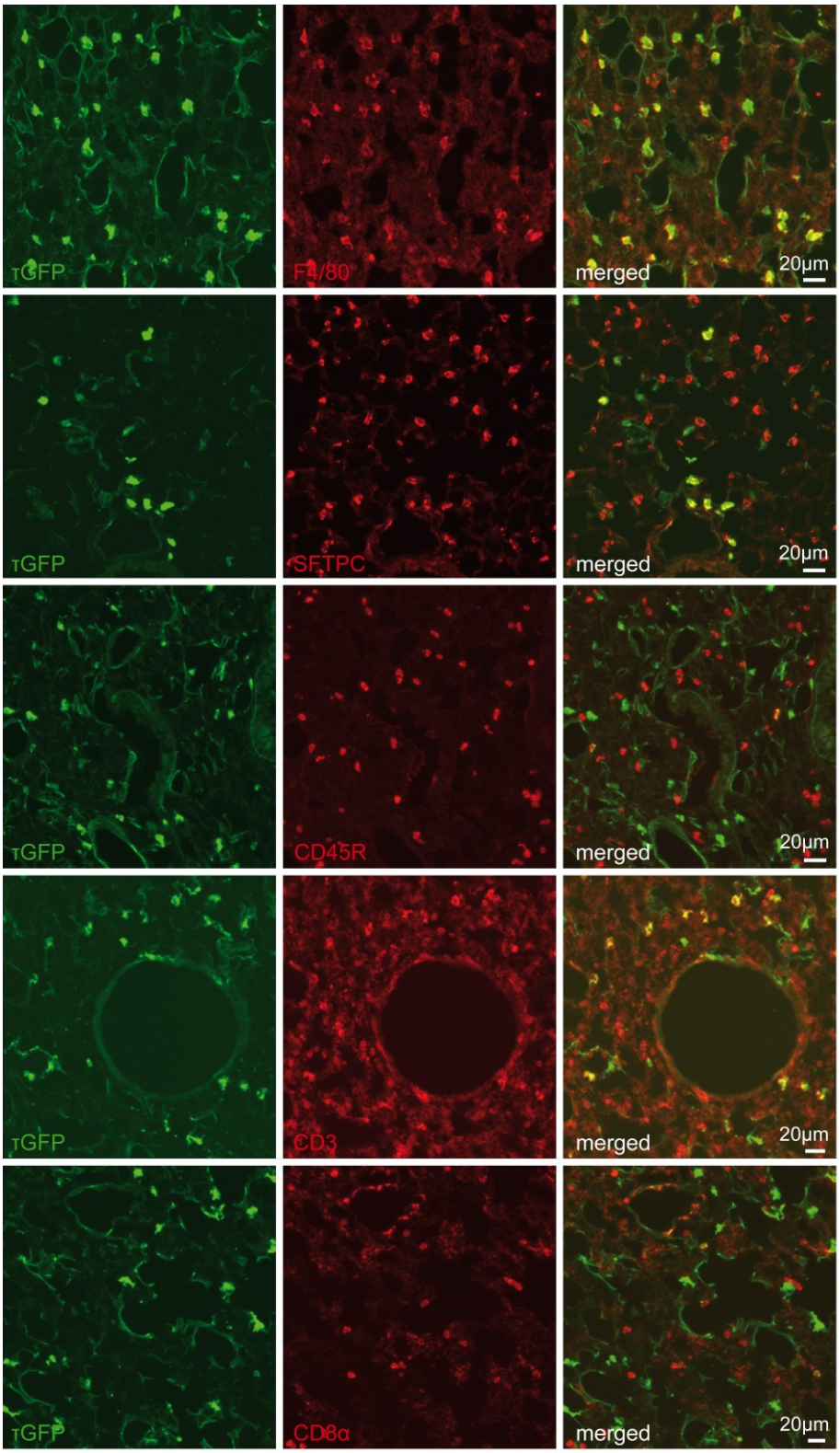

Figure 7. Immunostainings of lung tissue using *Trpml3*-IRES-Cre/eR26-τGFP mice. Co-localization of τGFP with cell markers indicate the presence of TRPML3 in the respective cell types. The highest rates of co-localization can be observed for macrophages detected through the marker F4/80. Modified from: Spix et al., *Nat Commun* 13**,** 318 (2022) (1).

Additionally, a quantification of TRPML3-expressing cells per cell type was performed by counting the numbers of cells showing co-localization in five randomly chosen fields of

view (**Figure 8**). This analysis revealed that ~40% of macrophages in the lung tissue are positive for TRPML3. This constitutes the highest percentage of TRPML3-expressing cells among all analyzed cell types, as the others showed lower expression rates (~12% for T-cells, ~10% for AT2-cells and 1% for B-cells).

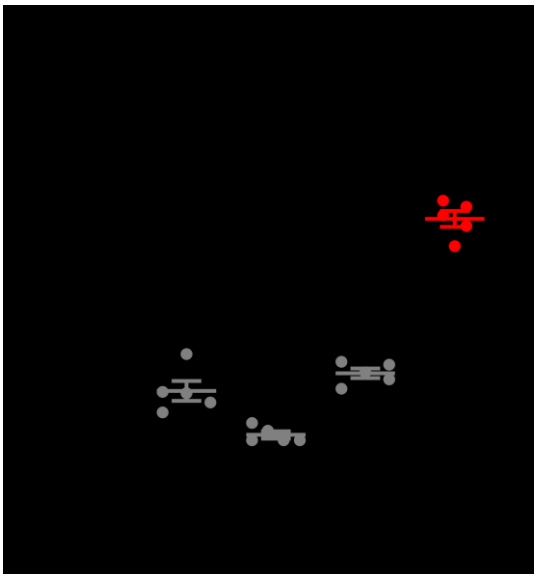

Figure 8. TRPML3 expression rates within several cell types. Quantification of TRPML3-expressing cells obtained from the analysis of five fields of view per cell type. Shown is the mean ± SEM. From: Spix et al., *Nat Commun* 13, 318 (2022) (1).

Figure 9 shows immunostainings of BAL cells collected from *Trpml3*-IRES-Cre/*eR26*-τGFP mouse lungs. All cells isolated by BAL were positively stained by the macrophage markers F4/80 and Galectin-3, which generally confirms their huge abundance in the lavage. Obviously, the vast majority of AMΦ also showed expression of τGFP indicating the presence of TRPML3 in this cell type.

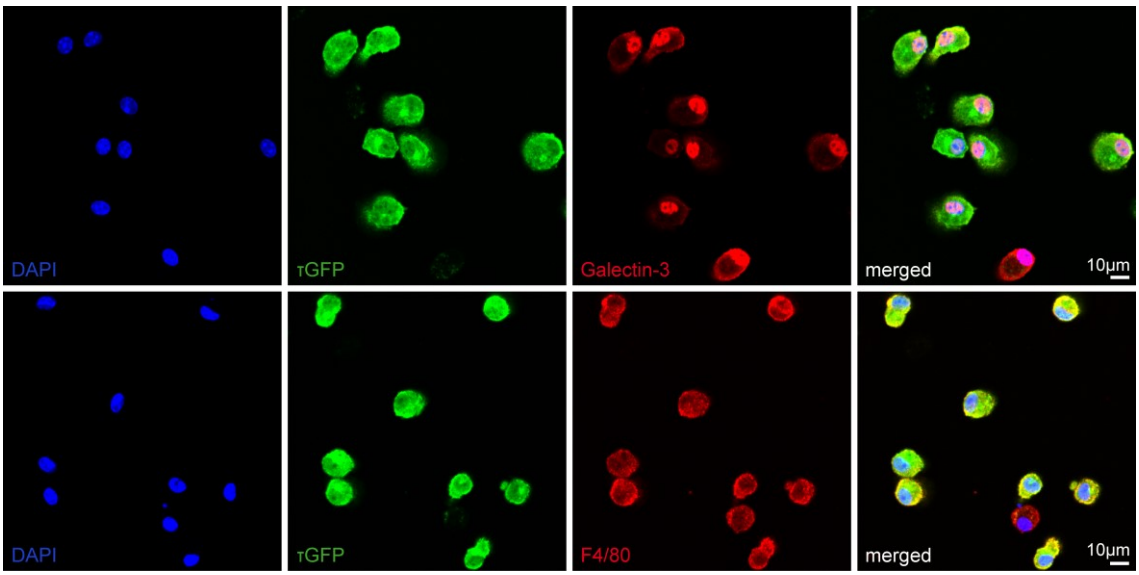

Figure 9. Immunostainings of BAL cells from *Trpml3*-IRES-Cre/eR26-τGFP mice. The vast majority of AMΦ isolated by BAL are positive for TRPML3, as shown by the co-localization with τGFP. Modified from: Spix et al., *Nat Commun* 13**,** 318 (2022) (1).

However, as depicted in **Figure 9 and Figure 10A**, some very few AMΦ appear to be τGFP-. Still, quantification analysis revealed a significant amount of ~87% of AMΦ being positive for τGFP, and TRPML3 respectively (**Figure 10B**).

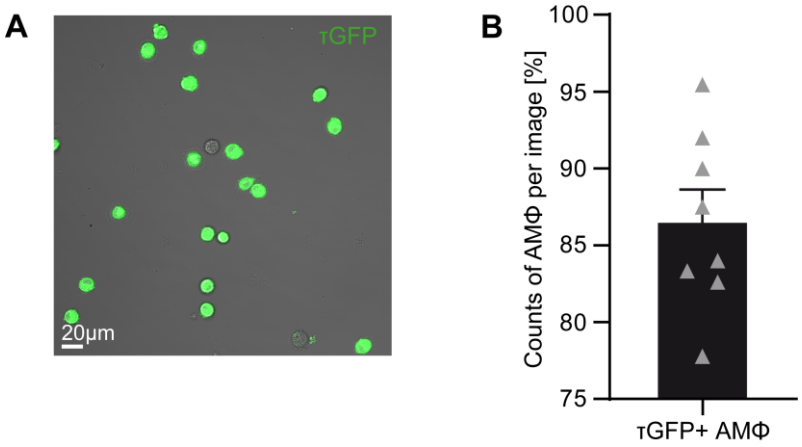

Figure 10. τGFP+ AMΦ in BAL from *Trpml3*-IRES-Cre/eR26-τGFP mice. (A) Representative image of τGFP+ AMΦ isolated by BAL. The vast majority of cells show τGFP expression. (B) Quantification of τGFP+ AMΦ illustrated as counts of AMΦ per image obtained from analysis of eight randomly chosen images, as shown in A. Shown is the mean ± SEM. From: Modified from: Spix et al., *Nat Commun* 13**,** 318 (2022) (1).

3.1.2 FACS analysis of tissue and BAL cells from *Trpml3*-IRES-Cre/*eR26*-τGFP mouse lungs

To corroborate the results of the immunostainings that are clearly pointing to expression of TRPML3 in AMΦ, and to extend the expression analysis to a broader range of immune cell types, FACS analysis was performed of both lung tissue and of BAL cells isolated from *Trpml3*-IRES-Cre/*eR26*-τGFP mice. The following gating sequence was applied to determine TRPML3-expressing cells in lung tissue (**Figure 11A**): Initially, forward scatter (FSC) and side scatter (SSC) were utilized to gate lymphocytes and single cells, thereby excluding doublets and debris. After selecting all living immune cells (CD45+/ LD-), only the τGFP+ (=TRPML3+) population was identified and used for the subsequent gating. Then, several immune cell types were excluded from further analysis: B-cells identified as CD3-/B220+, and T-cells identified as CD3+/B220-, and neutrophils identified as Ly6G+, as well as two small subgroups of CD11c-/CD11b- cells and MHCII- cells. This eventually provided a huge cluster of macrophages (MΦ) (CD24+/CD64-), and a tiny one of dendritic cells (DC) (CD24+/CD64-). The MHCII- population could be further separated into monocytes as CD64-/CD11b+ and natural killer cells (NK) as CD64-/CD11b^{low}. The

DC population was split into CD11b+ DC and CD11b- DC (=CD103+) and eosinophils (Eos) as CD11b+/MHCII-. The huge MΦ population was finally sub-grouped into AMΦ (CD11b-) and IMΦ (CD11b+). This sequential gating analysis revealed the vast majority of TRPML3-expressing immune cells being MΦ, or more specifically AMΦ, as only very few TRPML3+ cells were identified as IMΦ. Additionally, quantification analysis confirmed this: ~72% of τGFP+ cells accounted for MΦ, ~10% for T-cells and ~8% for B-cells, while for the other immune cell types the percentages were below 1% (**Figure 11B**).

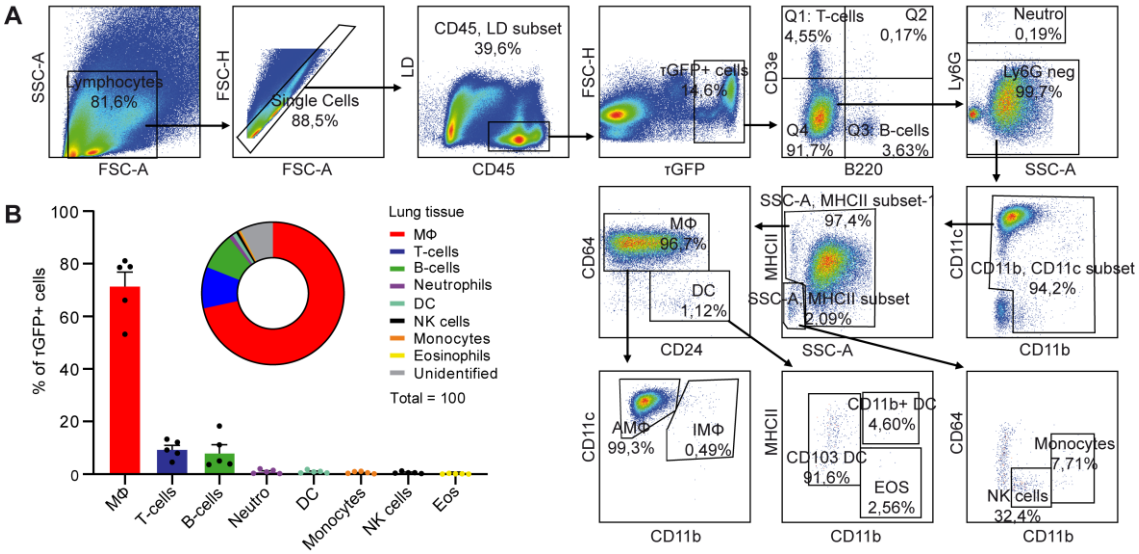

Figure 11. FACS analysis of lung tissue from *Trpml3*-IRES-Cre/eR26-τGFP mice. (A) Sequential gatings applied to determine TRPML3+ immune cells. Dot plots revealed AMΦ as the largest TRPML3+ immune cell population. (B) Bar and pie charts illustrate the percentages of τGFP+ cells for every analyzed cell type, based on quantitative analysis of dot plots as shown in A. Shown is the mean ± SEM, obtained from five *Trpml3*-IRES-Cre/eR26-τGFP reporter mice. From: Spix et al., *Nat Commun* 13**,** 318 (2022) (1).

For the identification of TRPML3-expressing immune cells in BAL, the same sequential gating strategy as described above for lung tissue samples was adopted to the first six gatings. As a last gating step, the Ly6G- cluster was further defined using the markers CD11c and CD11b. It uncovered a huge population of CD11b-/CD11c+ AMΦ, while IMΦ were absent (**Figure 12A**). Accordingly, a quantification analysis showed that the overwhelming majority of τGFP+ (=TRPML3+) cells in BAL correspond to AMΦ (97.5%) (**Figure 12B**).

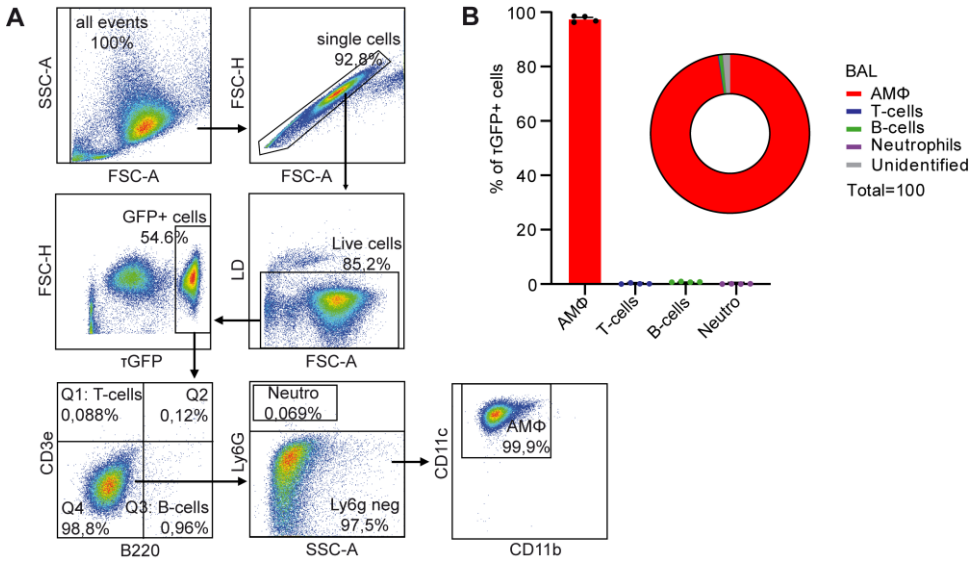

Figure 12. FACS analysis of BAL cells from *Trpml3*-IRES-Cre/eR26-τGFP mice. (A) Sequential gatings applied to determine TRPML3+ immune cells of the lavage. The final dot plot highlight the large TRPML3+ AMΦ population. (B) Bar and pie charts illustrate the percentages of τGFP+ cells for every analyzed cell type, based on quantitative analysis of dot plots as depicted in A. Shown is the mean ± SEM, obtained from four *Trpml3*-IRES-Cre/eR26-τGFP reporter mice. From: Spix et al., *Nat Commun* 13, 318 (2022) (1).

In summary, both immunostainings and FACS analysis of both lung tissue and lavage cells consistently and convincingly show that the TRPML3 channel is mainly expressed in AMΦ in the lung.

3.2 Lung function measurements

AMΦ constitute an important immune cell type in the lungs and are heavily involved both in host defense and in inflammatory processes in the lungs, as described in previous chapters. Therefore, loss of TRPML3 as in *Trpml3*$^{-/-}$ mice might contribute to development of lung diseases or might have influences on lung architecture resulting in limitations of lung function. Hence, lung function parameters of *Trpml3*$^{-/-}$ mice were measured and compared to WT control mice.

3.2.1 Basal measurements of Elastance and Compliance

Firstly, lung function measurements of *Trpml3*$^{-/-}$ mice compared to WT control mice were performed under basal conditions, i.e. without any previous treatments. To corroborate findings of changed lung function parameters, experiments were executed with two different *Trpml3*$^{-/-}$ mice models: *Mcoln3*$^{tm1.1Jga}$ and *Mcoln3*$^{tm1.2Hels}$. The lung function param-

eters dynamic Compliance (C) and Elastance (E) were measured. The Elastance is defined as pressure change (ΔP) per volume change (ΔV), E = ΔP/ ΔV. It describes the elastic rigidity of the respiratory system, e.g. a lung with low Elastance is very flexible and pliable. On the opposite, the dynamic Compliance is the reciprocal of the Elastance (C = ΔV/ ΔP) and is a measure for the ability of the lungs to stretch. Exemplary, a high dynamic Compliance of the lungs is associated with a high stretchability and is characteristic for an emphysematous lung.

Figure 13 shows a graphical illustration of the values for Elastance and dynamic Compliance measured from the two different *Trpml3*$^{-/-}$ mice models, *Mcoln3*$^{tm1.2Hels}$ in **Figure 13A** and *Mcoln3*$^{tm1.1Jga}$ in **Figure 13B**. In both mouse models, the Elastance was significantly reduced compared to the respective WT control mice, whereas the dynamic Compliance was significantly increased. These alterations pointed to an emphysema lung condition in *Trpml3*$^{-/-}$ mice.

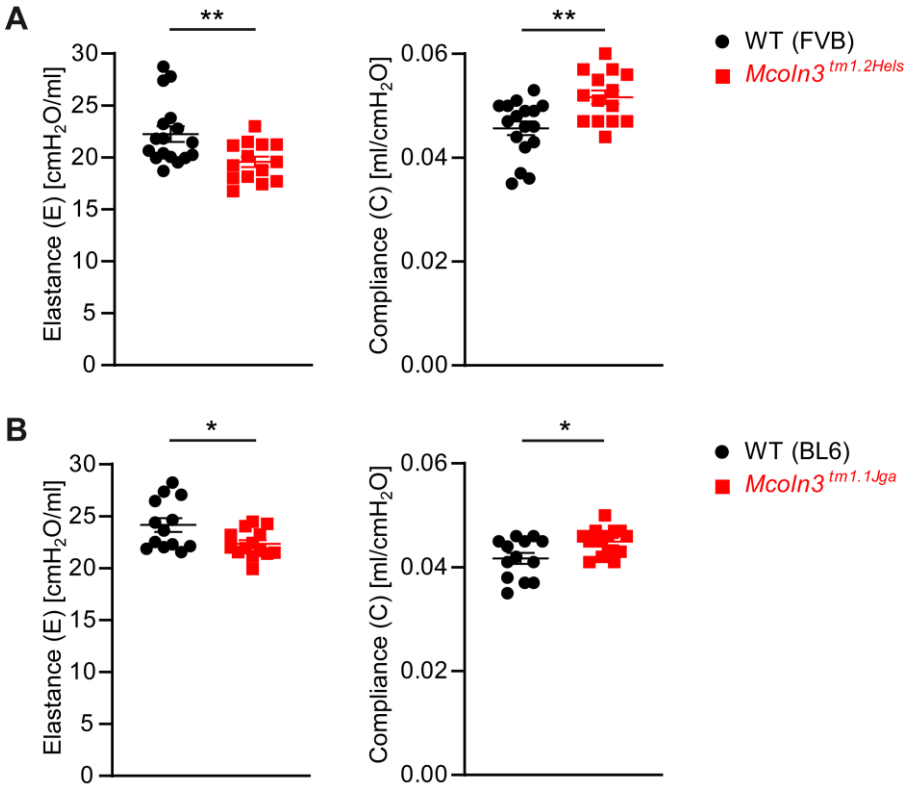

Figure 13. Lung function of *Trpml3*$^{-/-}$ mice under basal conditions. Values for Elastance and dynamic Compliance of two *Trpml3*$^{-/-}$ mouse models, *Mcoln3*$^{tm1.2Hels}$ in (A) and *Mcoln3*$^{tm1.1Jga}$ in (B), compared to WT mice, aged 4-5 months. One dot corresponds to the measurement of one mouse in A and B. Shown is the mean ± SEM. Unpaired and two-tailed Student's t-test was used. * p<0.05, ** p<0.01. Modified from: Spix et al., *Nat Commun* 13, 318 (2022) (1).

3.2.2 Lung emphysema mouse model

In a next step, lung function measurements of *Trpml3*$^{-/-}$ mice were performed under diseased conditions to investigate if the impairments in lung function, observed under basal conditions, are further aggravated. For that, a well-established mouse model for lung emphysema was used, in which the emphysematous lung condition is induced through the application of a porcine pancreatic elastase compared to PBS application as a control. The graphs of **Figure 14** show several lung function parameters measured for both the elastase-treated mice and control mice, WT versus *Trpml3*$^{-/-}$ mice (*Mcoln3*$^{tm1.1Jga}$), respectively. Repeatedly, a significant reduction of Elastance, as well as significant increase of dynamic Compliance, was detected for basal *Trpml3*$^{-/-}$ mice (**Figure 14A, B**). Additionally, the elastase treatment resulted in a further enhanced lung emphysema phenotype, as Elastance and dynamic Compliance were changed more dramatically with the most prominent change in *Trpml3*$^{-/-}$ mice compared to WT (**Figure 14A, B**). Furthermore, Tissue Elasticity (H) was measured, which is an estimation for the elasticity of the lung tissue, compared to the Elastance being indicative for the whole thorax (lung tissue + chest walls + airways). Tissue Elasticity was significantly reduced in both elastase- and PBS-treated *Trpml3*$^{-/-}$ mice compared to WT control mice (**Figure 14C**). Values for Inspiratory Capacity (IC), which represents the amount of air being potentially inhaled at end of a normal expiration, and Total Lung Capacity (A), an estimate for the volumes in the lungs at maximal inflation, were likewise and significantly elevated in the elastase-exposed *Trpml3*$^{-/-}$ mice in comparison to WT mice, but not in the PBS-treated groups (**Figure 14D, E**). Similar to the dynamic Compliance, the Quasi-Static Compliance (Cst) is a measure of the lungs to stretch, meaning to increase the lung volume, but at a static, given pressure compared to dynamic Compliance, where the pressure is variable during the measurement of lung volumes. Here, the Quasi-Static Compliance was significantly elevated in the elastase-exposed *Trpml3*$^{-/-}$ mice compared to WT (**Figure 14F**).

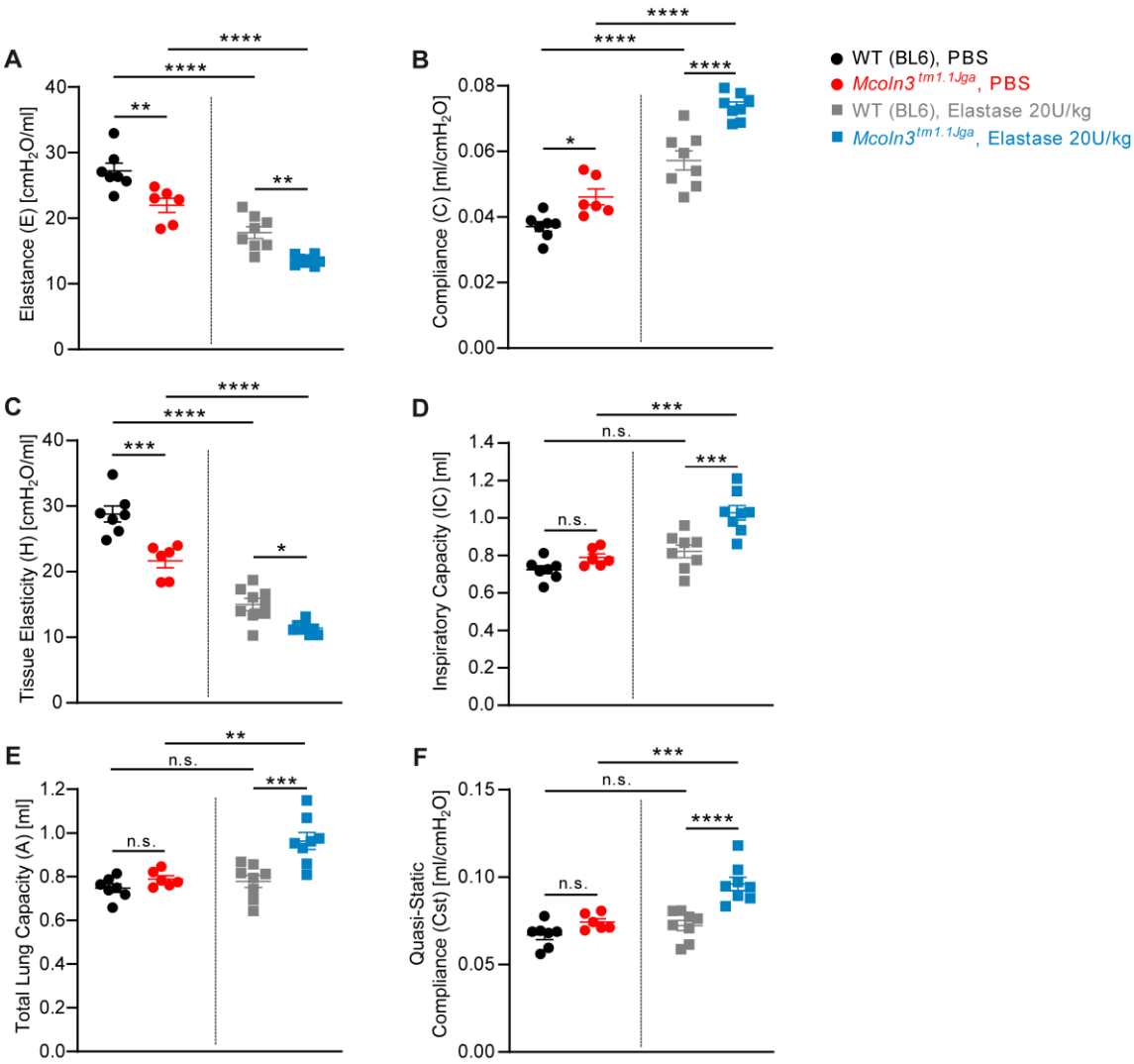

Figure 14. Lung function of *Trpml3*$^{-/-}$ mice after elastase treatment. Values for Elastance (A), dynamic Compliance (B), Tissue Elasticity (C), Inspiratory Capacity (D), Total Lung Capacity (E), and Quasi-Static Compliance (F) in elastase versus PBS treated WT and *Trpml3*$^{-/-}$ mice (*Mcoln3*$^{tm1.1Jga}$) aged 4-5 months. One dot corresponds to the measurement of one mouse in A to F. Shown is the mean ± SEM. Two-way ANOVA was used followed by Tukey's post-hoc test. * p<0.05, ** p<0.01, *** p<0.001, **** p<0.0001. Modified from: Spix et al., *Nat Commun* 13, 318 (2022) (1).

Finally, the values for lung volume measured at different pressures through gradual inflation and deflation were plotted to receive pressure-volume loops, as shown in **Figure 15**. This revealed a shift of the curves towards larger volumes in *Trpml3*$^{-/-}$ mice compared to WT under both PBS and elastase treatment, the latter one showing the most dramatic shift. Abnormalities or shifting of pressure-volume curves can be used as tool to uncover lung dysfunctions. E.g., a shift towards larger volumes as seen in *Trpml3*$^{-/-}$ mice is indicative for an emphysematous lung as the destruction of lung architecture results in already larger lung volumes at low pressures.

To summarize, several parameters of pulmonary function were significantly changed in *Trpml3* deficient mice compared to WT, with the most powerful alterations found in *Trpml3*$^{-/-}$ mice after elastase treatment. These changes are pointing to an emphysema lung phenotype.

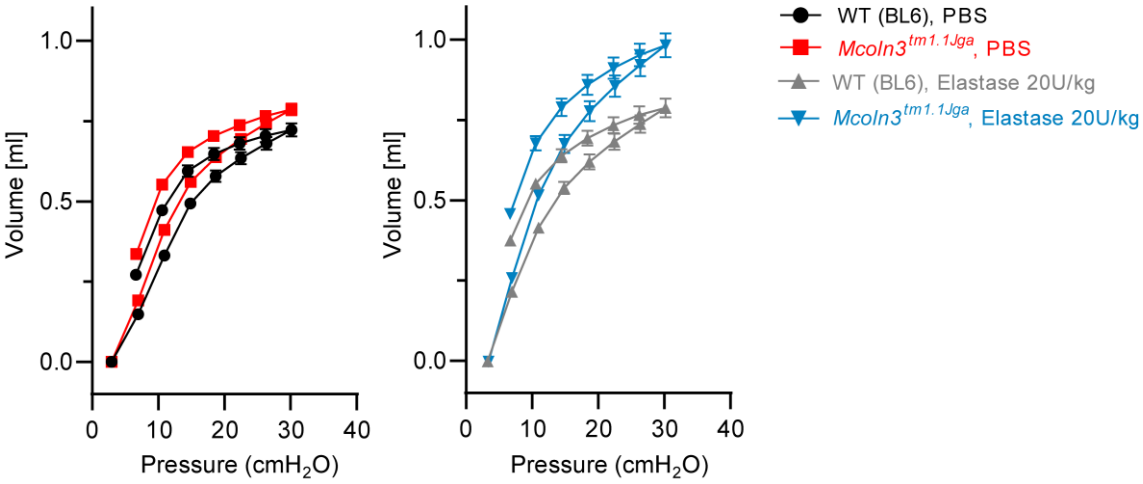

Figure 15. Pressure-volume loops of *Trpml3*$^{-/-}$ mice. Pressure-volume curves retrieved from lung function measurements using elastase versus PBS treated WT and *Trpml3*$^{-/-}$ mice (*Mcoln3*$^{tm1.1Jga}$) aged 4-5 months. Shown is the mean ± SEM calculated for each group. Modified from: Spix et al., *Nat Commun* 13**,** 318 (2022) (1).

3.2.3 COPD mouse model

To further strengthen the link between TRPML3 and COPD, measurements of respiratory mechanics were conducted using WT and *Trpml3*$^{-/-}$ mice that were chronically exposed to cigarette smoke (CS), since this constitutes the most relevant cause of COPD. **Figure 16** shows the values of Elastance and dynamic Compliance measured for each group. Elastance was significantly decreased while dynamic Compliance was significantly elevated in *Trpml3*$^{-/-}$ mice in comparison to WT, both under CS exposure and under filtered air (FA) control. This again pointed to an emphysema phenotype in *Trpml3* deficient mice and confirmed the observations of the elastase experiment.

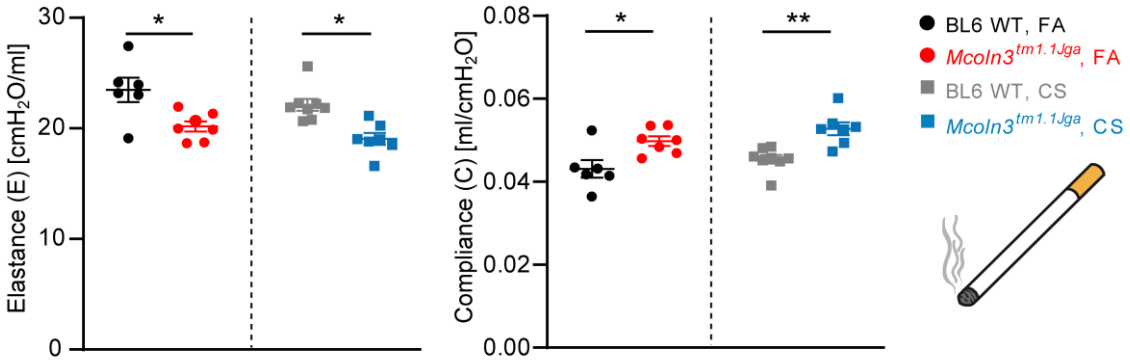

Figure 16. Lung function of *Trpml3*$^{-/-}$ mice after CS exposure. Values for Elastance and dynamic Compliance of FA or CS exposed *Trpml3*$^{-/-}$ mice (*Mcoln3*$^{tm1.1Jga}$) compared to WT. One dot corresponds to the measurement of one mouse. Shown is the mean ± SEM. Two-way ANOVA was used followed by Tukey's post-hoc test. * p<0.05, ** p<0.01. Modified from: Spix et al., *Nat Commun* 13, 318 (2022) (1).

3.3 Histological analysis of lung tissue

An emphysema lung condition is associated with pathological changes in the lung tissue, such as degradation of connective tissue between the alveoli and destruction of the alveolar walls that are leading to enlarged airspaces. To visualize such potential changes, lung tissues collected from the elastase and smoke experiment were analyzed in terms of quantification of airspace enlargements and loss of elastin fibers.

3.3.1 Lung emphysema mouse model

Figure 17A shows representative pictures of H&E-stained lung tissue section for all groups of the elastase experiment. It clearly shows the influence of the elastase application on lung tissue resulting in greatly enlarged airspaces compared to PBS control. These airspace enlargements were quantified by measuring the mean linear chord length per group, which is an estimation for the distance between the alveolar walls. It revealed increased airspace enlargements in *Trpml3*$^{-/-}$ mouse lungs compared to WT, which were only slightly significant (*) in the PBS control groups, but then strongly significant (****) under elastase treatment (**Figure 17B**). Thus, the strongest phenotype exacerbation was seen in elastase treated *Trpml3* deficient mice.

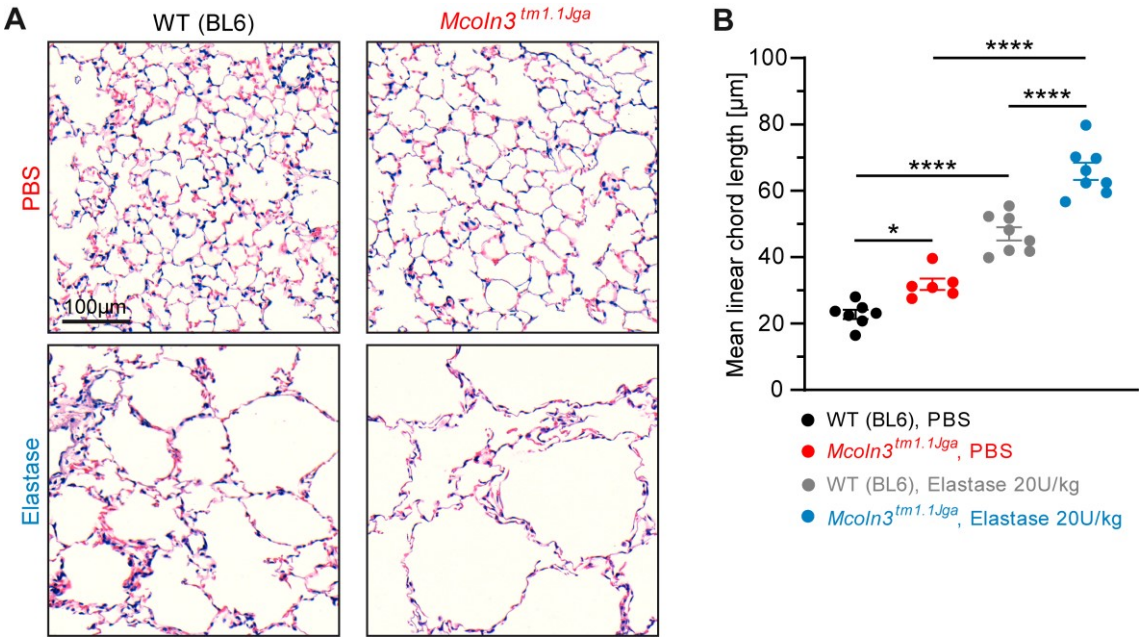

Figure 17. Quantification of airspace enlargements after elastase treatment. (A) Representative pictures of H&E-stained lung tissue slices from PBS and elastase treated WT and *Trpml3*$^{-/-}$ mice (*Mcoln3*$^{tm1.1Jga}$). (B) Quantitative analysis of enlarged airspaces as mean linear chord length. One dot corresponds to the lung tissue analysis from one mouse. Shown is the mean ± SEM. One-way ANOVA was used followed by Tukey's post-hoc test. * $p<0.05$, **** $p<0.0001$. From: Spix et al., *Nat Commun* 13**,** 318 (2022) (1).

Beside airspace enlargements, lung emphysema is characterized through degradation of ECM, especially elastin. To visualize elastin in lung tissue sections, the Verhoeff-Van Gieson staining (VVG) was applied, which stains collagen fibers red, elastin fibers black, and other tissue components yellow, as shown in **Figure 18A** for all groups of the elastase experiment. Furthermore, the images were the basis to quantify the amount of elastin in lung tissue sections of every group as counts of elastin fibers/field. This reveled a reduction of elastin in lung tissue sections from *Trpml3*$^{-/-}$ mice compared to WT, slightly significant (*) in the PBS control groups and stronger significant (**) in the elastase groups (**Figure 18B**).

Summarizing, the histological analysis of lung tissue sections corroborate the findings of the functional lung analysis. Airspace enlargements and atrophy of elastic tissue were markedly present in *Trpml3* deficient mice and confirms the emphysematous changes of their lungs.

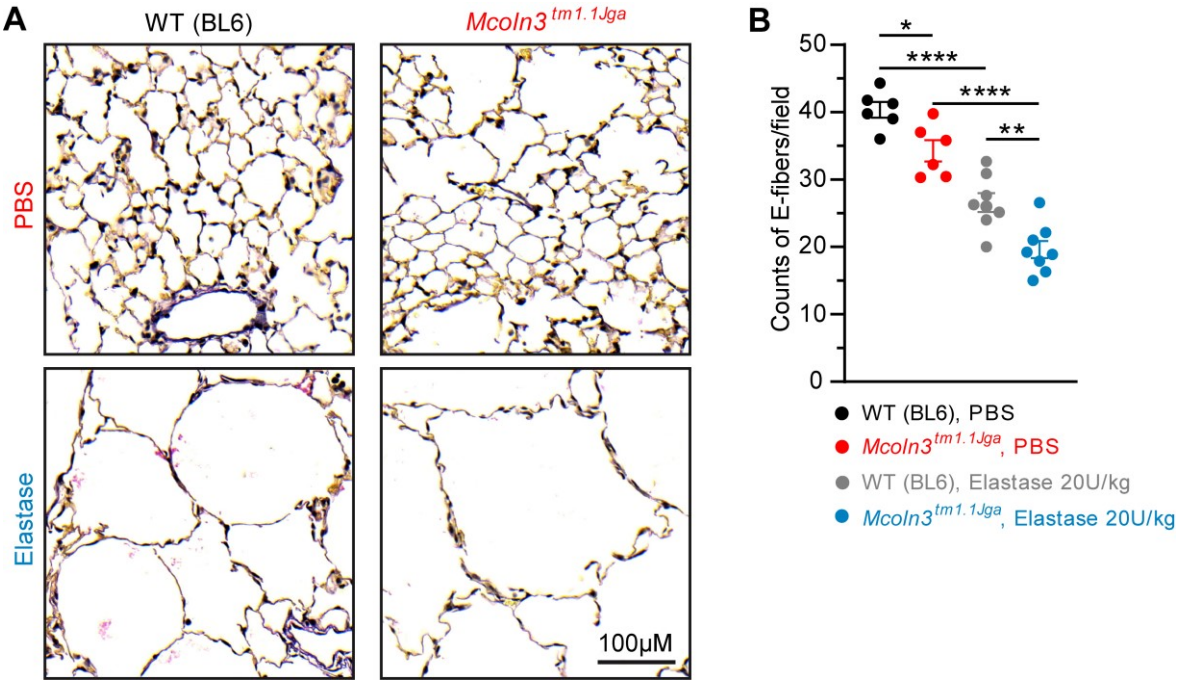

Figure 18. VVG staining and quantification of elastin fibers. (A) Representative pictures of VVG-stained lung tissue slices from PBS and elastase treated WT and *Trpml3*$^{-/-}$ mice (*Mcoln3*$^{tm1.1Jga}$). (B) Quantitative analysis of elastin fibers as counts/field in images as shown in A. The counts of elastin fibers were analyzed in 8-10 fields of view per mouse lung and the obtained mean corresponds to one dot. Shown is the mean ± SEM. One-way ANOVA was used followed by Tukey's post-hoc test. * $p<0.05$, ** $p<0.01$, **** $p<0.0001$. Modified from: Spix et al., *Nat Commun* 13**,** 318 (2022) (1).

3.3.2 COPD mouse model

To complete the histology data set, lung tissue sections were obtained from all mice of the smoke experiment and were subsequently analyzed in regards of airspace enlargements. In contrast to the elastase treatment, the smoke exposure appeared to be milder as it resulted in smaller and less conspicuous airspace enlargements (**Figure 19A)**. Still, and in line with the previous data, the quantification analysis revealed enlarged airspaces in *Trpml3*$^{-/-}$ mouse lungs compared to WT. The enlargements were present both under FA treatment and under CS exposure (**Figure 19B**), but were most pronounced in the lungs of treated *Trpml3*$^{-/-}$ mice showing the strongest phenotype exacerbation.

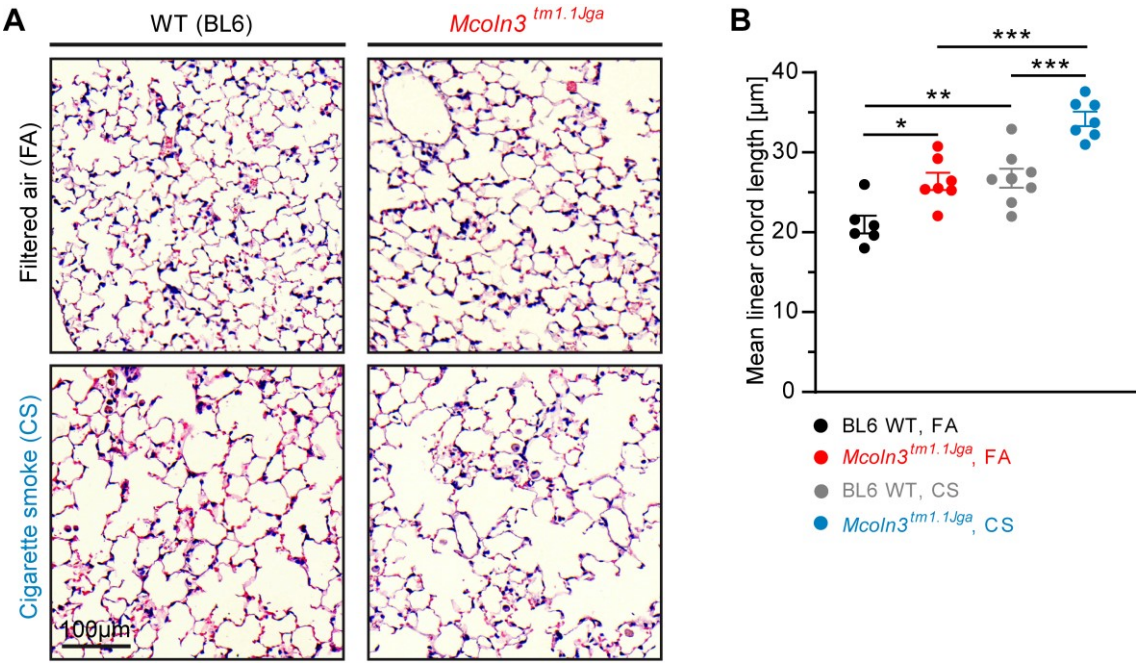

Figure 19. Quantification of airspace enlargements of CS exposed mice. (A) Representative pictures of H&E-stained lung tissue from FA or CS exposed WT and *Trpml3*$^{-/-}$ mice (*Mcoln3*$^{tm1.1Jga}$). (B) Quantitative analysis of enlarged airspaces as mean linear chord length. One dot corresponds to the lung tissue analysis from one mouse. Shown is the mean ± SEM. One-way ANOVA was used followed by Tukey's post-hoc test. * p<0.05, ** p<0.01, *** p<0.001. From: Spix et al., *Nat Commun* 13**,** 318 (2022) (1).

3.4 Analysis of BAL-Fluid

As described above, the results pointed to a lung emphysema phenotype in mice that are lacking the TRPML3 channel. Thus, the underlying mechanisms leading to this pathological lung condition should be determined. To this end, the bronchoalveolar lavage fluid (BAL-F) was collected from *Trpml3*$^{-/-}$ mice compared to WT to examine the acellular components of the lung lumen. In this context, both multiplex assay and ELISAs were performed for several inflammatory mediators (cytokines, chemokines, MMPs).

3.4.1 Multiplex assay

In an unbiased approach, a multiplex assay was applied to measure the concentrations of different cytokines, chemokines and proteases, i.e. MMP-12, MMP-9, MMP-2, interferon-γ (IFNγ), interleukin-10 (IL10), interleukin-6 (IL6), interleukin-4 (IL4), keratinocyte-derived chemokine/C-X-C motif chemokine ligand 1 (KC/CXCL1), vascular endothelial growth factor (VEGF), monokine induced by gamma interferon/C-X-C motif chemokine ligand 9 (MIG/CXCL9), and macrophage inflammatory protein 2 (MIP2), in BAL-F. As shown in **Figure 20**, only the macrophage-specific protease MMP-12 was significantly elevated in the BAL-F of *Trpml3*$^{-/-}$ mice compared to WT, whereas all other analyzed

inflammatory mediators were not significantly altered. Therefore, in the following experiments the focus was directed to the protease MMP-12, which is also known to be a key mediator in the formation and development of emphysema. Deducing from this, the increased MMP-12 levels in *Trpml3*$^{-/-}$ mice lungs could serve as a possible explanation for the emphysema phenotype.

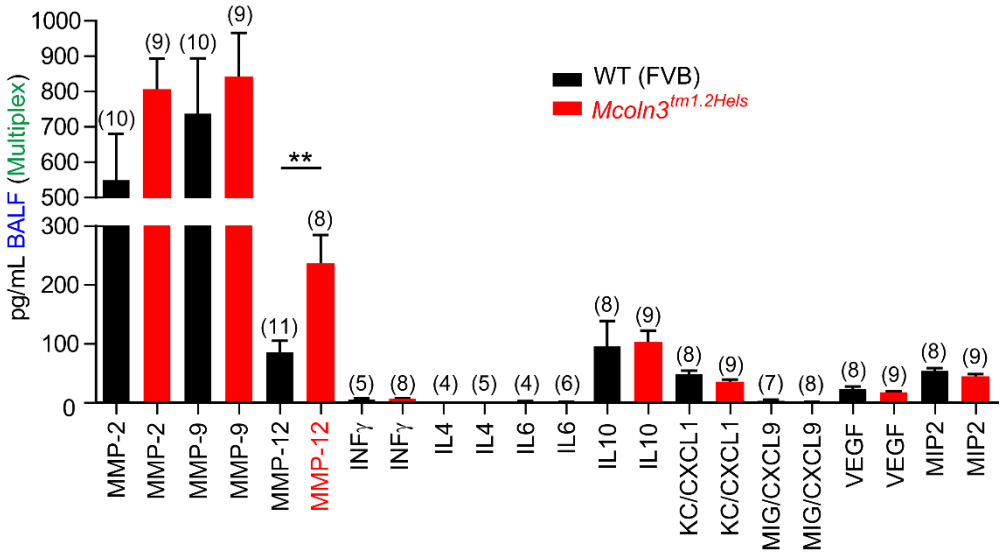

Figure 20. Quantification of inflammatory mediators in BAL-F. Concentrations of several cytokines, chemokines and MMPs in BAL-F of 4-months old WT and *Trpml3*$^{-/-}$ mice (*Mcoln3*$^{tm1.2Hels}$) assessed through multiplex analysis. Shown is the mean ± SEM. Student's t-test, unpaired, two-tailed, was used for statistical analysis. ** p<0.01. Modified from: Spix et al., *Nat Commun* 13, 318 (2022) (1). Results of this figure were obtained from co-authors.

3.4.2 ELISA of MMP-12

To further confirm the findings of the multiplex analysis, an enzyme-linked immunosorbent assay (ELISA) was performed, specifically for MMP-12, and using BAL-F samples of both *Trpml3*$^{-/-}$ mouse lines (*Mcoln3*$^{tm1.2Hels}$ and *Mcoln3*$^{tm1.1Jga}$). This revealed significantly increased MMP-12 levels in the BAL-F isolated from both knockout mouse models (**Figure 21**) and confirmed the results from the multiplex assay.

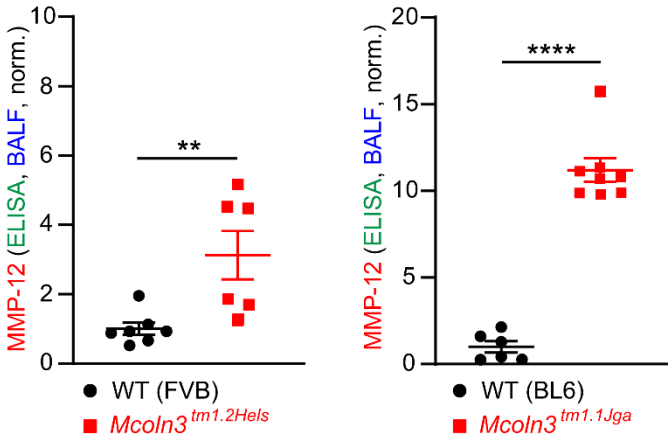

Figure 21. Quantification of MMP-12 in BAL-F through ELISA. Concentrations of MMP-12 were measured in BAL-F isolated from both *Trpml3*$^{-/-}$ mouse models (*Mcoln3*$^{tm1.2Hels}$ and *Mcoln3*$^{tm1.1Jga}$) and normalized to WT control samples. Normalized values are shown in the graphs as mean ± SEM. One dot corresponds to the BAL-F from one mouse. Student's t-test, unpaired, two-tailed, was applied for statistical analysis. ** p<0.01, **** p<0.0001. Modified from: Spix et al., *Nat Commun* 13, 318 (2022) (1).

3.4.3 ELISA of TIMPs

As described in chapter 1.4.1.3.2, the activity of proteolytic enzymes in the ECM is controlled by antiproteases, such as TIMPs controlling MMPs. Therefore, the levels of TIMP-2 and TIMP-1 were assessed by ELISA. TIMP-1 concentrations were found to be not significantly changed between WT and *Trpml3*$^{-/-}$ BAL-F, both in *Mcoln3*$^{tm1.2Hels}$ and *Mcoln3*$^{tm1.1Jga}$ (**Figure 22A**). Likewise, TIMP-2 concentrations were not significantly altered (**Figure 22B**). This pointed to an overabundance of MMP-12 versus TIMPs.

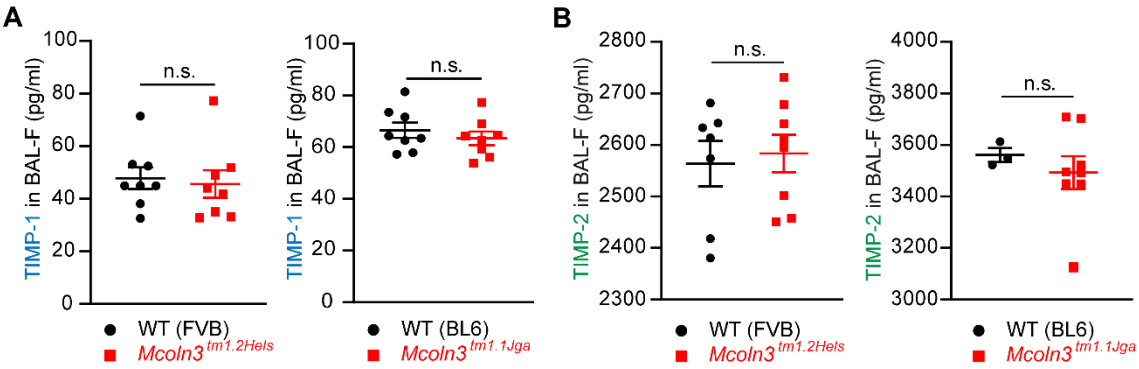

Figure 22. Quantification of TIMPs in BAL-F through ELISA. Concentrations of TIMP-1 (A) and TIMP-2 (B) in BAL-F isolated from both *Trpml3*$^{-/-}$ mouse models (*Mcoln3*$^{tm1.2Hels}$ and *Mcoln3*$^{tm1.1Jga}$) compared to WT control samples. Plotted values are mean ± SEM. One dot corresponds to the BAL-F from one mouse. Student's t-test, unpaired, two-tailed, was applied for statistical analysis. Modified from: Spix et al., *Nat Commun* 13, 318 (2022) (1).

3.4.4 ELISA of desmosine

MMP-12 degrades elastin within the ECM of the lungs. Elastin constitutes the major protein of elastin fibers. During the maturation process to elastin fibers, several elastin monomers are cross-linked via the formation of the amino acids desmosine or isodesmosine. These unique cross linker molecules of elastin can be used as biomarker for elastin degradation and COPD, as increased amounts of it are detected in sputum, plasma or urine (172,173). Hence, the concentration of desmosine was assessed in BAL-F of *Trpml3*$^{-/-}$ mice compared to WT via ELISA. A significant rise of desmosine was found in *Trpml3*$^{-/-}$ mice (**Figure 23**), which is in accordance with the elevated concentrations of MMP-12 in BAL-F that probably results in enhanced matrix degradation and cleavage of desmosine.

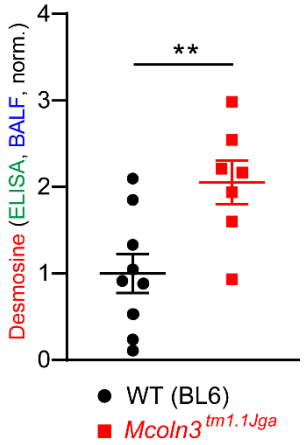

Figure 23. Quantification of desmosine in BAL-F through ELISA. Concentrations of desmosine were measured in BAL-F isolated from *Trpml3*$^{-/-}$ mice (*Mcoln3*$^{tm1.1Jga}$) and normalized to WT control samples. Normalized values are shown in the graph as mean ± SEM. One dot corresponds to the BAL-F from one mouse. Student's t-test, unpaired, two-tailed, was applied for statistical analysis. ** p<0.01. Modified from: Spix et al., *Nat Commun* 13, 318 (2022) (1).

3.4.5 ELISA of surfactant protein D (SP-D)

Pulmonary surfactant is important for normal and healthy lung activity. It is mainly composed of lipids, but also contains smaller amounts of surfactant proteins (SP), i.e. SP-A, SP-B, SP-C and SP-D (174). Overabundance or deficiency of surfactant proteins have been found to be linked to pulmonary disorders, e.g. an emphysema phenotype was found in SP-D deficient mice associated with higher MMP (-2, -9, -12) expression levels as compared with WT mice (110). Thus, it was important to investigate whether *Trpml3*$^{-/-}$ mice are also showing a deficiency in SP-D. However, an ELISA of BAL-F revealed no significant alterations of SP-D between WT and *Trpml3*$^{-/-}$ samples (**Figure 24**).

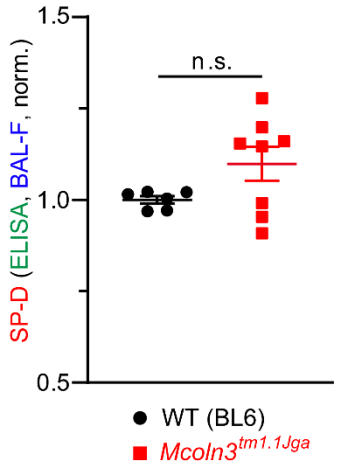

Figure 24. Quantification of SP-D in BAL-F through ELISA. Concentrations of SP-D were measured in BAL-F isolated from *Trpml3*$^{-/-}$ mice (*Mcoln3*$^{tm1.1Jga}$) and normalized to WT control samples. Normalized values are shown in the graph as mean ± SEM. One dot corresponds to the BAL-F from one mouse. Student's t-test, unpaired, two-tailed, was applied for statistical analysis. Modified from: Spix et al., *Nat Commun* 13**,** 318 (2022) (1).

3.5 Analysis of SN from cultured AMΦ

Next aim was to find out whether the increased MMP-12 amounts found in BAL-F of *Trpml3* deficient mice lungs are indeed due to secretions of TRPML3-expressing AMΦ and not due to other lung cell type's secretions. Thus, the SN from cultured AMΦ isolated from WT and *Trpml3*$^{-/-}$ mice lungs were analyzed for MMP-12 and several other MMPs. For that, both ELISAs and a multiplex assay was applied.

Using ELISA, elevated MMP-12 concentrations were detected in the SN from cultured *Trpml3*$^{-/-}$ AMΦ in comparison with WT AMΦ (**Figure 25A**), which confirmed that the changes of MMP-12 levels in BAL-F are most likely and specifically due to functional changes of AMΦ lacking TRPML3. An extended analysis of the SN using a multiplex assay revealed no significant changes between WT and *Trpml3*$^{-/-}$ samples for MMP-2, MMP-3, and proMMP-9, whereas the MMP-8 concentration was significantly elevated in *Trpml3*$^{-/-}$ AMΦ compared to WT (**Figure 25B**). Additionally, an MMP-8 selective ELISA supported this, as a significant rise of the MMP-8 levels was again detected in *Trpml3*$^{-/-}$ samples (**Figure 25C**).

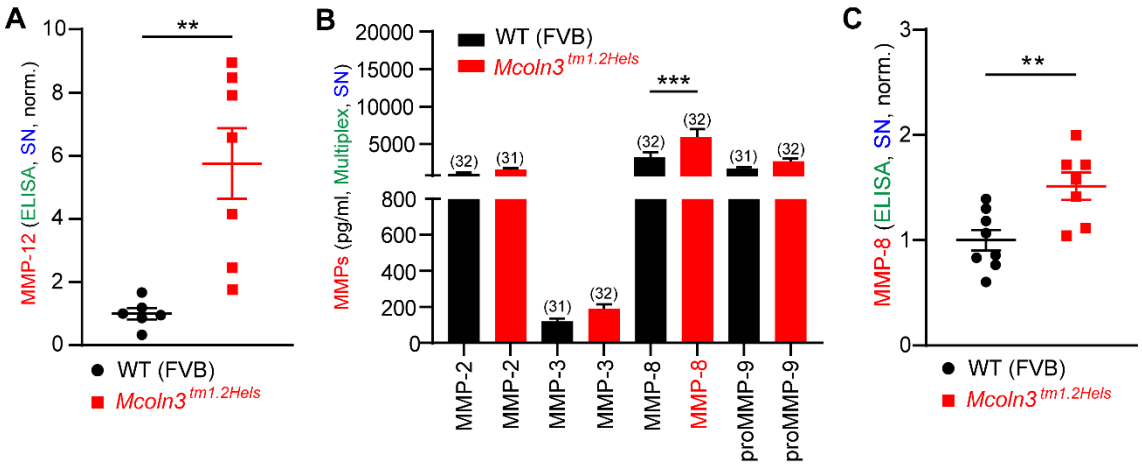

Figure 25. Quantification of MMPs in SN from cultured AMΦ. Concentrations of MMP-12 (A) and concentrations of MMP-8 (C) were measured in the SN from *Trpml3*$^{-/-}$ AMΦ cultures (*Mcoln3*$^{tm1.2Hels}$) and normalized to WT control samples. Normalized values are shown in the graphs as mean ± SEM. One dot represents the SN collected from one well. Student's t-test, unpaired, two-tailed, was used for statistical analysis. ** p<0.01. (B) Concentrations of several MMPs in SN from cultured AMΦ from WT and *Trpml3*$^{-/-}$ lungs (*Mcoln3*$^{tm1.2Hels}$). Values are shown as mean ± SEM. Two-way ANOVA followed by Tukey's post-hoc test. *** p<0.001. Modified from: Spix et al., *Nat Commun* 13, 318 (2022) (1). Results shown in B were obtained from co-authors.

3.6 qRT-PCR of AMΦ for MMP-12

The increase of MMP-12 found in BAL-F of *Trpml3*$^{-/-}$ mice lungs and found in the SN from *Trpml3*$^{-/-}$ AMΦ might be due to enhanced synthesis of MMP-12 in *Trpml3*$^{-/-}$ AMΦ. Therefore, qRT-PCR was performed using AMΦ cell pellets collected from WT and *Trpml3*$^{-/-}$ lungs by BAL. **Figure 26** shows that the mRNA expression levels of the *Mmp-12* gene were not significantly altered between WT and *Trpml3*$^{-/-}$ samples. These normal expression rates for the MMP-12 protein directed the focus rather on defects in endocytosis, endolysosomal trafficking and secretion/exocytosis of MMP-12 as potential reasons for the pulmonary emphysema phenotype in *Trpml3*$^{-/-}$ mice.

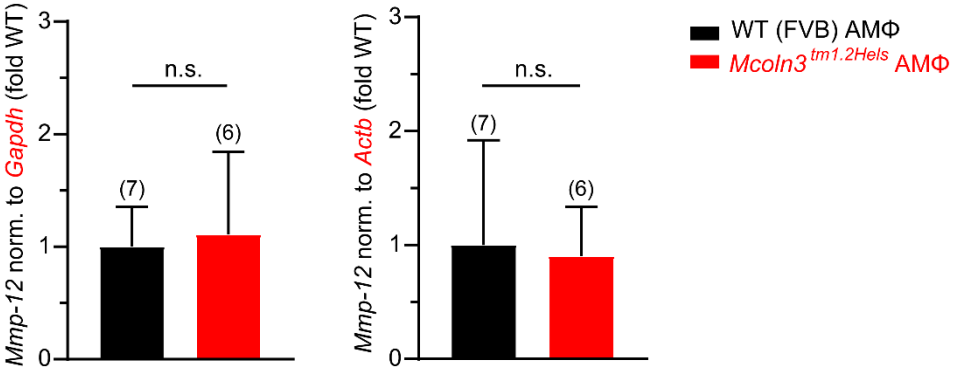

Figure 26. qRT-PCR of AMΦ for *Mmp-12* gene. mRNA expression of *Mmp-12* in WT and *Trpml3*$^{-/-}$ AMΦ (*Mcoln3*$^{tm1.2Hels}$) was measured and normalized to the house keeping genes *Gapdh* and *Actb*. Values obtained from *Trpml3*$^{-/-}$ samples were normalized to WT control samples and are shown as mean ± SEM. Student's t-test, unpaired, two-tailed, was applied for statistical analysis. Modified from: Spix et al., *Nat Commun* 13**,** 318 (2022) (1).

3.7 Intracellular trafficking assay

To study early endosomal trafficking, fluorescent transferrin (Tf) was used as a probe to visualize its trafficking and recycling pathway in AMΦ. Tf usually binds to the Tf-receptor (TfR) on the cell surface, which induces the uptake of the formed ligand-receptor complex. Within the cell, the complex is transported through early endosomes and finally reaches recycling endosomes, from where it is recycled back to the cell surface (175).

Firstly, WT and *Trpml3*$^{-/-}$ AMΦ were pulsed with Tf and subsequently chased for 20 min via confocal microscope. It revealed a decline of intracellular Tf in WT AMΦ due to regular recycling of ligand and receptor to the cell surface (**Figure 27A, B**). On the other hand, such a decline was not observed in *Trpml3*$^{-/-}$ AMΦ (*Mcoln3*$^{tm1.2Hels}$ and *Mcoln3*$^{tm1.1Jga}$), instead, the intracellular Tf amounts remained on levels similar to those at the beginning of the chase time (**Figure 27A, B**). Thus, Tf trafficking was significantly delayed in *Trpml3*$^{-/-}$ AMΦ. Additionally, the uptake of Tf was reduced in *Trpml3*$^{-/-}$ AMΦ (*Mcoln3*$^{tm1.2Hels}$ and *Mcoln3*$^{tm1.1Jga}$), when pulsed with the fluorescent Tf for 20 min (**Figure 27C**). Similarly, co-localization experiments revealed a higher degree of Tf co-localized with EEA1 in *Trpml3*$^{-/-}$ AMΦ compared to WT (**Figure 27D, E**), which pointed to a block of Tf forward trafficking and thus retention of Tf within early endosomes. To rule out that the afore described changes were due to different TfR expression in WT and *Trpml3*$^{-/-}$ AMΦ, western blots were performed for the TfR protein and obtained bands were normalized to ß-Actin. As shown in **Figure 27F, G**, no significant alterations in TfR expression were found between WT and *Trpml3*$^{-/-}$ samples.

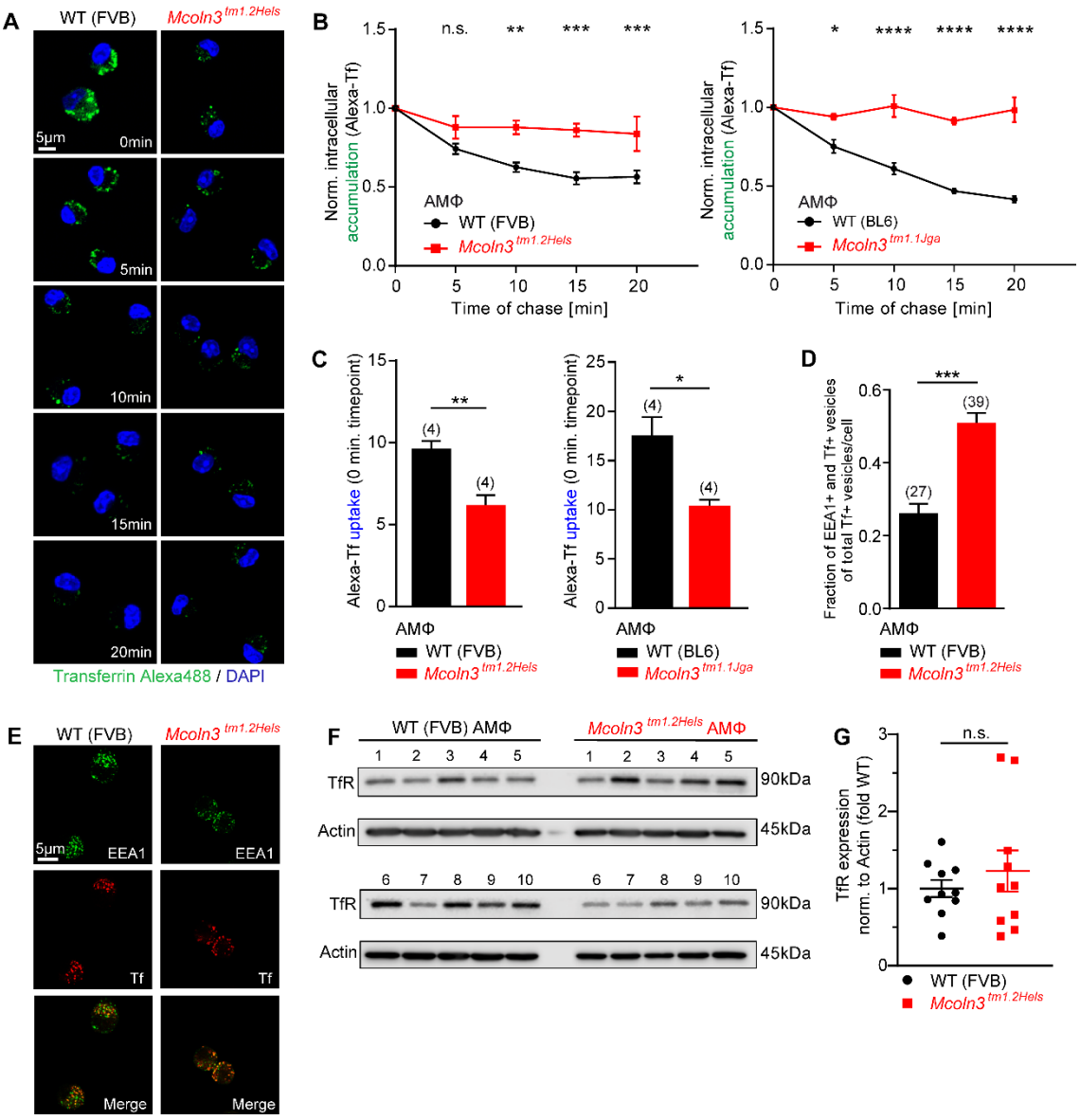

Figure 27. Early endosomal trafficking in AMΦ. (A) Representative images of WT and *Trpml3*$^{-/-}$ AMΦ demonstrating the decline of fluorescent Tf within 20 min after pulse. (B) Quantification of fluorescent and intracellular Tf within 20 min of chase after the pulse using images as shown in A, for *Mcoln3*$^{tm1.2Hels}$ and *Mcoln3*$^{tm1.1Jga}$. The decline of intracellular Tf is depicted as normalized to 0 min timepoint. Mean ± SEM obtained from four independent experiments. Two-way ANOVA followed by Bonferroni's post-hoc test. * p<0.05, ** p<0.01, *** p<0.001, **** p<0.0001. (C) Quantification of Tf in the cells immediately after the pulse as Tf uptake (= 0 min timepoint of chase), for *Mcoln3*$^{tm1.2Hels}$ and *Mcoln3*$^{tm1.1Jga}$. Mean ± SEM obtained from four independent experiments. Student's t-test, unpaired, two-tailed. * p<0.05, ** p<0.01. (D-E) Representative pictures and quantitative analysis of co-localization between Tf and EEA1 in vesicles of WT and *Trpml3*$^{-/-}$ AMΦ (*Mcoln3*$^{tm1.2Hels}$). 3 independent experiments were performed and 27 WT cells and 39 *Trpml3*$^{-/-}$ cells were analyzed. Student's t-test, unpaired, two-tailed. *** p<0.001. (F) Western blots (WB) for Tf-receptor (TfR) (90kDa) and ß-Actin (45kDa) as the loading control. Shown are two independent blots obtained from 5 WT and 5 *Trpml3*$^{-/-}$ AMΦ lysates, each. (G) Quantitative analysis of WB bands as depcited in F. TfR expression was normalized to ß-Actin and *Trpml3*$^{-/-}$ samples were normalized to WT. One dot corresponds to one mouse. Mean ± SEM. Statistical analysis was performed using Student's t-test. Modified from: Spix et al., *Nat Commun* 13, 318 (2022) (1). Results shown in D, E were obtained from co-authors.

3.8 Lysosomal exocytosis

Increased amounts of MMP-12 in BAL-F of *Trpml3*$^{-/-}$ mice or in the SN from cultured *Trpml3*$^{-/-}$ AMΦ might be due to increased secretion of MMP-12, e.g. through lysosomal exocytosis. To investigate whether loss of TRPML3 is associated with dysfunctions in exocytosis, two different assays were applied, ß-hexosaminidase-assay and LAMP1 translocation assay.

ß-Hexosaminidase is a lysosomal enzyme that is secreted via lysosomal exocytosis and is involved in the hydrolysis of several substrates. Thus, it can be used as a marker for lysosomal exocytosis. Here, secreted ß-hexosaminidase activity was measured in the SN of cultured WT and *Trpml3*$^{-/-}$ AMΦ after stimulation of TRPML3 by the selective agonist ML3-SA1 (1). Ionomycin is known to induce lysosomal exocytosis (176,177) and was used as a positive control. Treatment of AMΦ with 4 µM ionomycin for 10 min led to the strongest effects on ß-hexosaminidase release both in WT and *Trpml3*$^{-/-}$ samples (**Figure 28A**). The TRPML3 activator ML3-SA1 did not induce lysosomal exocytosis, neither in WT nor in *Trpml3*$^{-/-}$ AMΦ, as the ß-hexosaminidase release was very low and comparable to the levels obtained with the DMSO control (**Figure 28A**).

LAMP1 is translocated to the PM upon lysosomal exocytosis. Thus, the LAMP1 content of the PM may serve as a measure for lysosomal exocytosis. LAMP1 was visualized through an immunostaining and its intensity in the PM was measured as depicted in **Figure 28B, C**. Once again, maximum effects were obtained with the lysosomal exocytosis inducer ionomycin serving as the positive control (**Figure 28B, C**). However, treatment with 30 µM ML3-SA1 for 60 or 120 min did not affect lysosomal exocytosis, since the LAMP1 PM intensity was not significantly changed compared to DMSO control (**Figure 28B, C**).

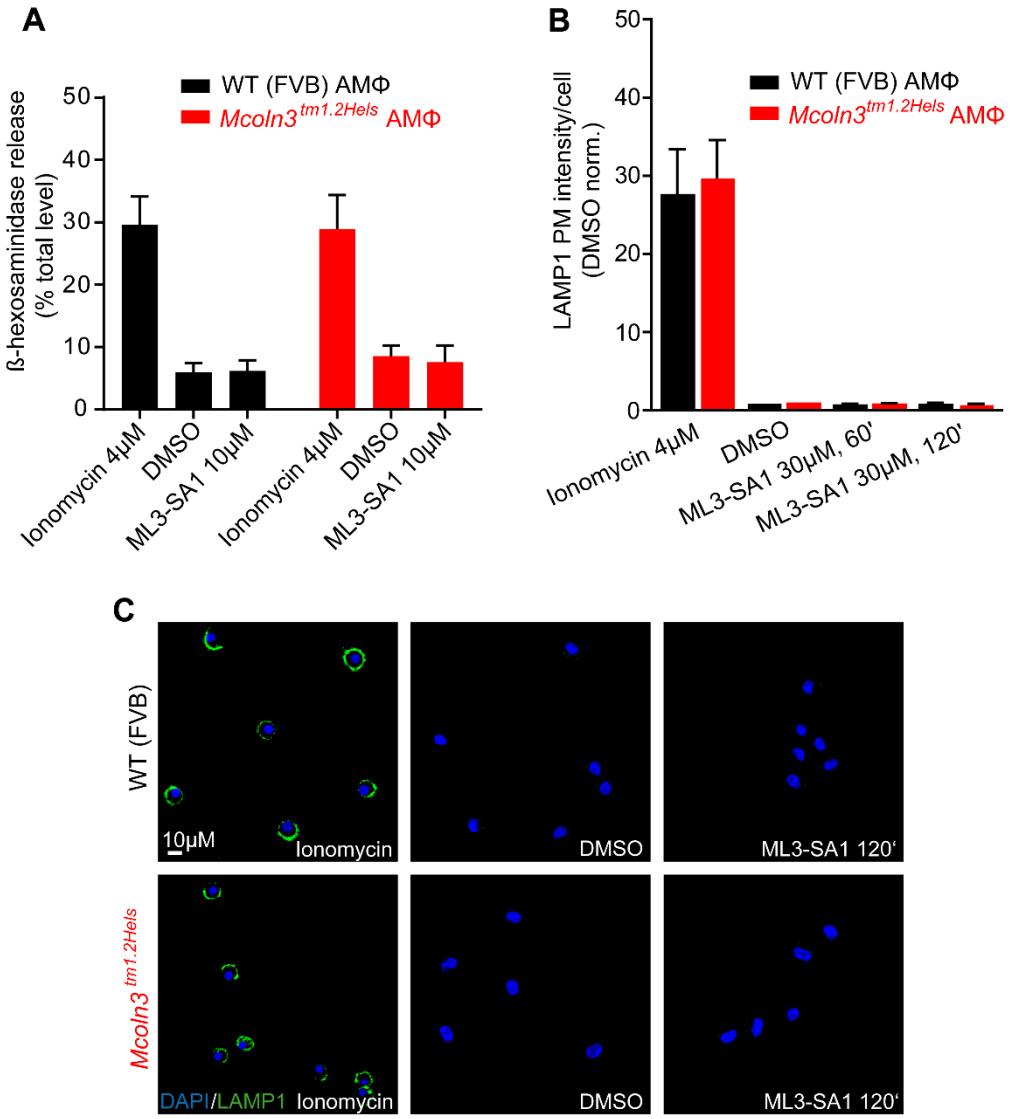

Figure 28. Lysosomal exocytosis. (A) ß-Hexosaminidase release measured in SN from WT and *Trpml3*$^{-/-}$ AMΦ (*Mcoln3*$^{tm1.2Hels}$) stimulated with ML3-SA1 agonist or vehicle control. Values are mean ± SEM obtained from four independent experiments. (B) LAMP1 intensity PM of WT and *Trpml3*$^{-/-}$ AMΦ (*Mcoln3*$^{tm1.2Hels}$) stimulated with ML3-SA1 agonist for 60 or 120 min or DMSO control. Values were normalized to DMSO control and are presented as mean ± SEM obtained from three independently conducted experiments. (C) Representative pictures showing LAMP1 translocation to the PM using WT and *Trpml3*$^{-/-}$ AMΦ (*Mcoln3*$^{tm1.2Hels}$). Images were obtained after treatment of AMΦ with either 4 µM ionomycin for 10 min or DMSO control for 120 min or with 30 µM ML3-SA1 for 120min. Modified from: Spix et al., *Nat Commun* 13, 318 (2022) (1).

3.9 Endocytosis

To examine if loss of TRPML3 is associated with dysfunctions in endocytosis, e.g. of MMP-12, several experiments were implemented. Firstly, a dextran uptake assay was performed, and further on, MMP-12 was measured in the SN collected from AMΦ after blockage of endocytosis and after activation of TRPML3.

3.9.1 Dextran uptake assay

Fluorescent dextran molecules are commonly used to study fluid endocytosis, also called pinocytosis, in which fluids and particles contained therein are taken up into the cell (178). To evaluate such endocytosis rates in the presence and absence of TRPML3, the quantity of intracellular and fluorescently labeled dextran was measured in WT and *Trpml3*$^{-/-}$ AMΦ. The representative images in **Figure 29A** show the increase of dextran absorbed into the cells over a period of 30min. The intracellular fluorescence intensities were measured and graphed over time, as depicted in **Figure 29B**. Both WT AMΦ and *Trpml3*$^{-/-}$ AMΦ are taking up the dextran molecules, as the intracellular dextran is increasing and accumulating in the cells during the 30 min period. Nevertheless, the graphs also clearly show lower endocytosis rates in *Trpml3*$^{-/-}$ AMΦ in comparison with WT AMΦ, which applied for both *Trpml3*$^{-/-}$ mouse models (**Figure 29B**). Thus, TRPML3 appeared to be involved in fluid phase endocytosis and triggered the focus on endocytosis of MMP-12, specifically, for the next experiments.

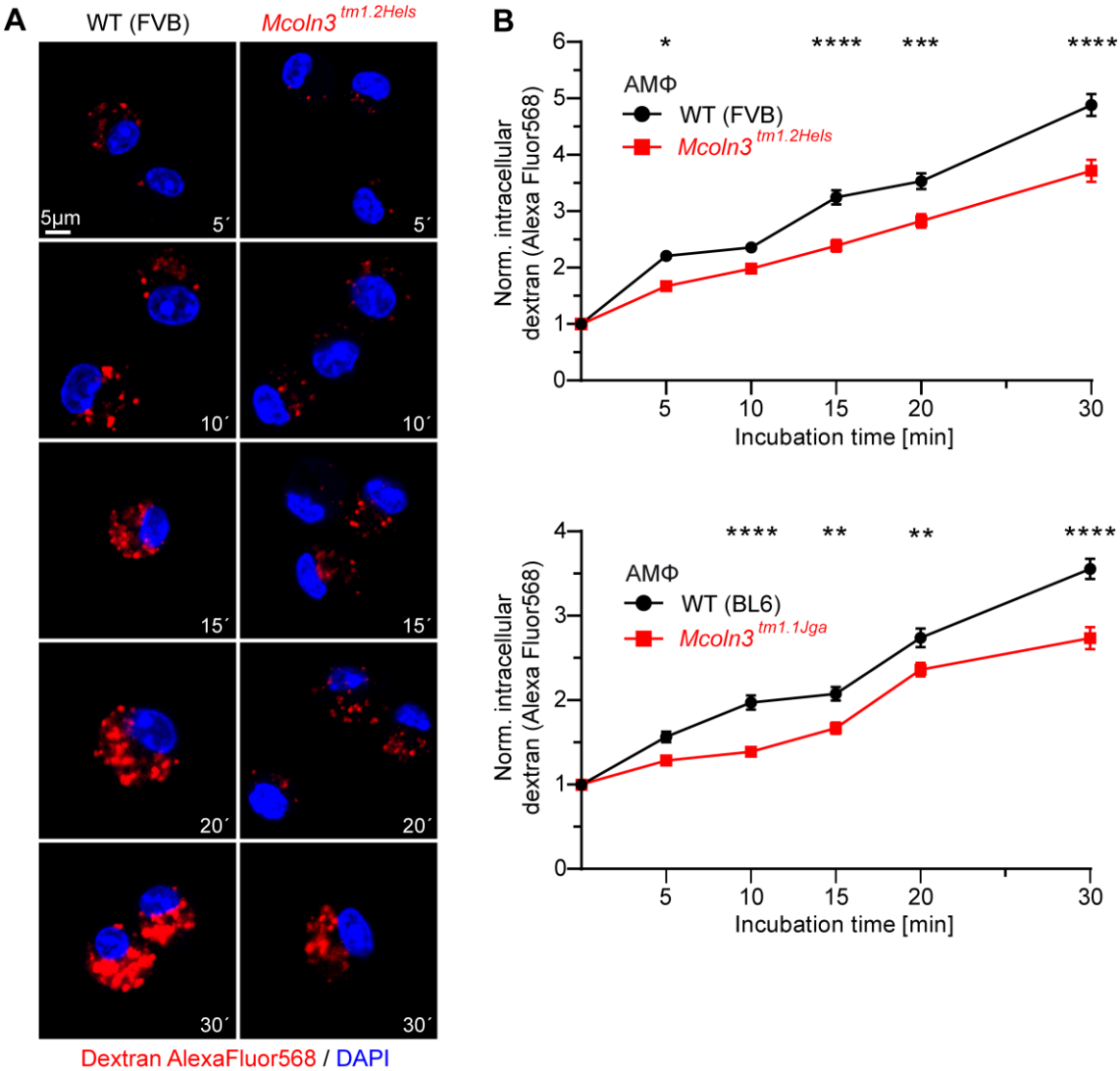

Figure 29. Dextran uptake assay. (A) Representative images of WT and *Trpml3*$^{-/-}$ AMΦ showing the uptake of fluorescent dextran after different incubation times (5, 10, 15, 20 and 30 min). (B) Quantification of intracellular dextran at various incubation timepoints using images as shown in A, for *Mcoln3*$^{tm1.2Hels}$ and *Mcoln3*$^{tm1.1Jga}$. The increase of intracellular fluorescence intensity is depicted as normalized to untreated control cells (0 min of incubation). A minimum of 130 cells were analyzed per timepoint and genotype obtained from five independently conducted experiments for both *Trpml3*$^{-/-}$ lines. Mean ± SEM. Two-way ANOVA followed by Bonferroni's post-hoc test. * p<0.05, ** p<0.01, *** p<0.001, **** p<0.0001. Modified from: Spix et al., *Nat Commun* 13**,** 318 (2022) (1).

3.9.2 MMP-12 levels after blockage of endocytosis

To investigate whether the MMP-12 levels are affected by the reduced endocytosis rates found in *Trpml3*$^{-/-}$ AMΦ, MMP-12 was measured in the SN from cultured AMΦ (WT vs. *Trpml3*$^{-/-}$) after blockage of various endocytosis pathways. The following known blockers were used and compared to DMSO control (basal): Methyl-β-cyclodextrin (MBCD) to inhibit clathrin-independent endocytosis (CIE), 5-(N-ethyl-N-isopropyl)-amiloride (EIPA) for macropinocytosis (MP), and Dynasore (Dyn) as a blocker for clathrin-mediated endocytosis (CME) (179,180). Dyn didn`t affect MMP-12 concentration in the SN, neither from WT nor from *Trpml3*$^{-/-}$ AMΦ (**Figure 30A**). MBCD induced a strong increase of MMP-12 in WT AMΦ SN (****), however it also had an effect in *Trpml3*$^{-/-}$ AMΦ SN (**) (**Figure 30A**). On the contrary, for EIPA, an increase of the MMP-12 levels were only observed in the SN from WT AMΦ, while the effect was gone in the *Trpml3*$^{-/-}$ AMΦ SN (**Figure 30A**). In summary, these results suggest that MMP-12 levels may be regulated by AMΦ through endocytosis, since its blockage is leading to an accumulation of MMP-12 in the SN. Beyond that and more precisely, MMP-12 seems to be taken up via CIE and MP, but not via CME, as illustrated in **Figure 30B**.

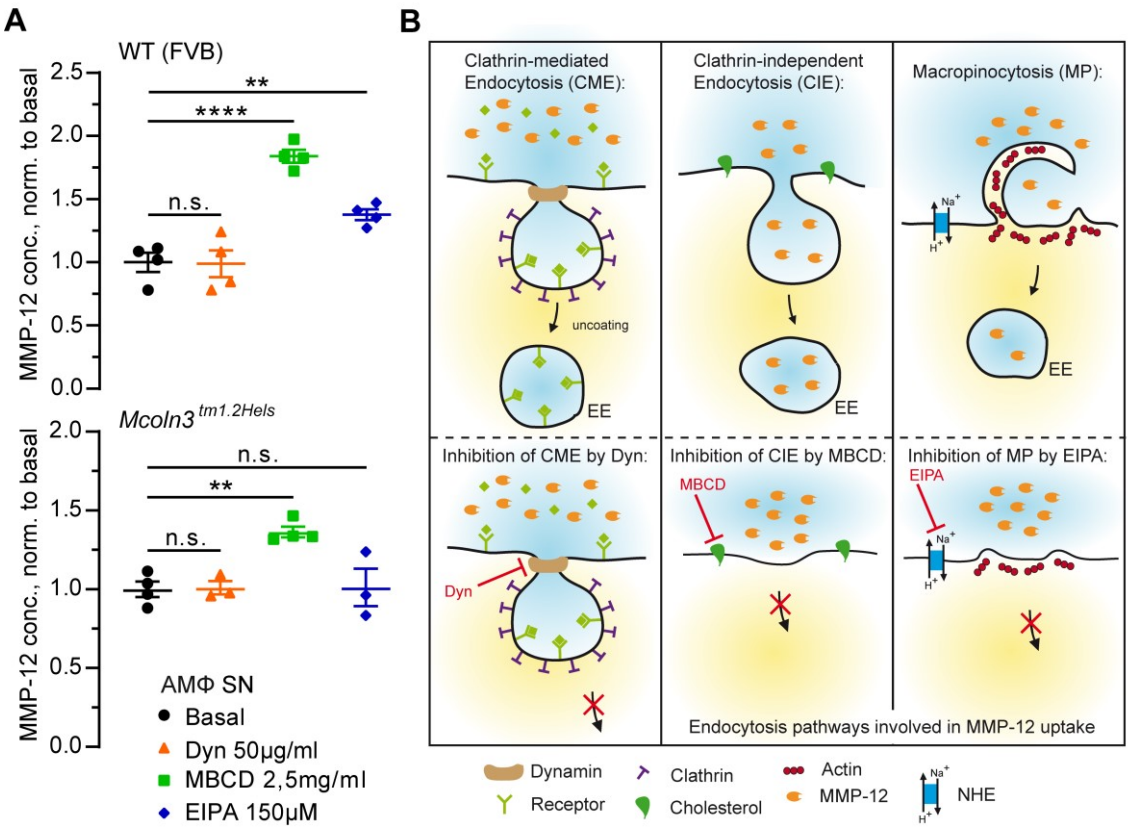

Figure 30. Impact of endocytosis blockers on MMP-12 levels. (A) MMP-12 concentrations in the SN from WT and *Trpml3*$^{-/-}$ AMΦ after inhibition of endocytosis by Dyn, MBCD and EIPA normalized to DMSO control (basal). Each dot represents the SN collected from one well. Shown is the mean ± SEM. One-way ANOVA followed by Dunnett's post-hoc test. * p<0.05, ** p<0.01, **** p<0.0001. (B) Illustration of results as shown in A, highlighting the involvement of CIE and MP, but not CME, on MMP-12 uptake though AMΦ. Modified from: Spix et al., *Nat Commun* 13, 318 (2022) (1).

3.9.3 MMP-12 levels after activation of TRPML3

The previous experiments demonstrated a relation between endocytosis and MMP-12, meaning that inhibition of two different endocytosis pathways, CIE and MP, is able to increase MMP-12 levels. However, a proof for TRPML3 being involved in endocytosis of MMP-12, specifically, was still missing. Therefore, MMP-12 levels were finally measured in the SN of AMΦ after modulation of TRPML3. The selective mouse TRPML3 agonist ML3-SA1 was used in order to find out, whether this would influence the MMP-12 state of the AMΦ SN. As shown in **Figure 31A**, ML3-SA1 significantly decreased MMP-12 in WT AMΦ SN, whereas no ML3-SA1 effect was seen in *Trpml3*$^{-/-}$ AMΦ SN as compared with DMSO.

Additionally, and to rule out that ML3-SA1 had cytotoxic effects on the AMΦ during the incubation overnight, a LDH cytotoxicity assay was performed. The positive control (lysis

buffer) expectedly resulted in high optical densities, meaning high LDH levels in the SN and high cytotoxicity (**Figure 31B**). This also became visible by the color change from light yellow to deep orange. Importantly, ML3-SA1 did not induce any color change and showed optical densities that were comparable to the DMSO control. Therefore, a cytotoxic effect of ML3-SA1 could be excluded.

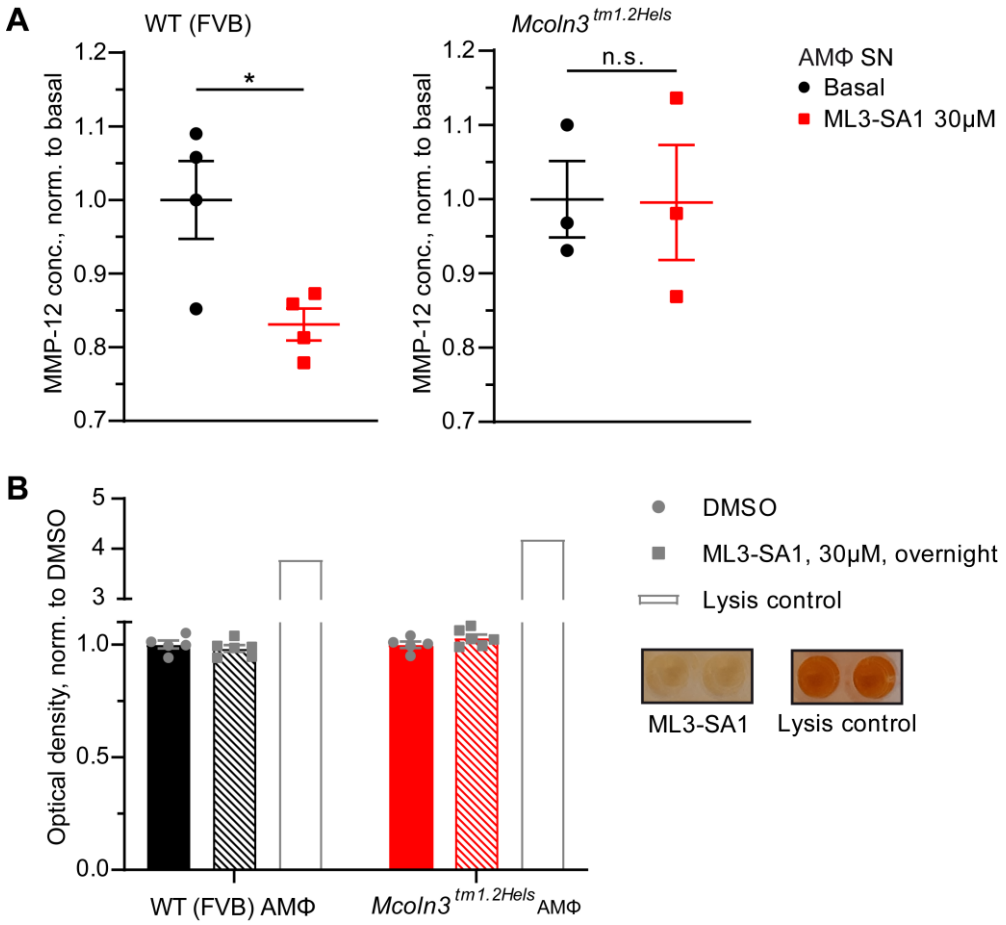

Figure 31. Impact of TRPML3 activation on MMP-12 levels. (A) MMP-12 concentrations in the SN from WT and *Trpml3*$^{-/-}$ AMΦ after activation of TRPML3 through ML3-SA1, 30 µM. Values were normalized to DMSO control (basal). Each dot represents the SN collected from one well. Shown is the mean ± SEM. Student's t-test, unpaired, two-tailed. * $p<0.05$. (B) LDH toxicity assay. AMΦ were either treated with ML3-SA1, 30 µM, or DMSO control overnight and cytotoxicity was evaluated through measuring LDH as optical density in the SN. As a positive control, a lysis buffer was used. Values were normalized to the DMSO control. Each dot corresponds to the SN collected from one well. Shown is the mean ± SEM. Modified from: Spix et al., *Nat Commun* 13, 318 (2022) (1).

4. Discussion

4.1 TRPML3 expression in the murine lung

TRPML3 expression in whole lung tissue has been reported previously based on qRT-PCR (28,34), but so far, it remained unclear in which lung cell types exactly TRPML3 is expressed. In this dissertation, a *Trpml3*-IRES-Cre/*eR26*-τGFP reporter mouse line (1) was used to overcome this problem. In these mice, all TRPML3-expressing cells simultaneously express τGFP in their cytoplasm and can thereby be detected and visualized. Similar mouse models for TRPM5 and TRPV6 have been generated before and were successfully used to determine the TRPM5 and TRPV6 expression pattern throughout the murine body (181,182). Here, immunofluorescence and FACS experiments using both tissue and lavage cells isolated from *Trpml3*-IRES-Cre/*eR26*-τGFP mouse lungs clearly demonstrate the presence of TRPML3, specifically in lung AMΦ. Surprisingly, TRPML3 expression was found to be rather negligible in interstitial lung tissue macrophages. Lower levels of TRPML3 in lung tissue macrophages compared to high levels in AMΦ were also confirmed by qRT-PCR (1). The aforementioned analyses mainly included lung immune cells, while neglecting lung epithelial and endothelial cells. However, transcriptomic data obtained from single-cell suspensions of murine WT lung tissue unveiled once more predominant TRPML3 expression in AMΦ (1). Except from pulmonary immune cells, this analysis included a broad range of lung epithelial cells, e.g. AT2- and AT1-cells, ciliated cells, fibroblasts, club cells, goblet cells, and endothelial cells, e.g. lymphatic endothelial cells and vascular endothelial cells, all showing low percentages of TRPML3 expression, and low average expression level of TRPML3 (1). Conversely, the averaged expression of TRPML3 was exceptionally high in AMΦ (1). To conclude, the extraordinary high and predominant expression in AMΦ suggested TRPML3 to have an important function in this cell type and thus, in AMΦ related mechanisms and processes.

4.2 Role of TRPML3 in development of COPD and lung emphysema

To investigate the contribution of TRPML3 in lung function and disease, respiratory system mechanics of WT vs. *Trpml3*$^{-/-}$ mice were evaluated by measuring lung function parameters, firstly under basal conditions, meaning that the mice haven`t been treated before measurements. To this end, two different *Trpml3*$^{-/-}$ mouse models were used:

Mcoln3$^{tm1.2Hels}$, on FVB background, and in which exon 11 of the *Mcoln3* gene encoding the pore-loop and the pore adjacent transmembrane domain 6 was excised (168), and *Mcoln3*$^{tm1.1Jga}$, on 75% BL6 background, in which exons 7 and 8 were excised resulting in transmembrane domains 2-6 and the pore of TRPML3 not being synthesized (32,35). The lung function measurements using the flexiVent system and its forced oscillation technique (FOT) revealed a significant increase of dynamic Compliance (lung's ability to stretch) and significant decrease of Elastance (lung's elastic stiffness) in both *Trpml3*$^{-/-}$ mouse models compared to WT. These kinds of changes in lung function parameters are typical of an emphysema lung, as it was previously shown for the elastase-induced emphysema mouse model (183). By using two different *Trpml3*$^{-/-}$ lines, any reliance of the lung emphysema phenotype on genetic backgrounds or on the way of knocking out the channel could be excluded. Until now, not any other phenotypic disease has been shown for *Trpml3*$^{-/-}$ mice, confirming the novelty of this finding. Only mice lacking both TRPML1 and TRPML3 have been found with a pathological phenotype present in intestinal enterocytes that show accelerated vacuolation during birth and weaning (35). On the contrary, single knockouts of either TRPML1 or TRPML3 were not affected (35).

4.2.1 The elastase-induced lung emphysema mouse model

The elastase-induced emphysema mouse model is a widely used method to provoke emphysematous changes in the lungs (184). The application of a porcine pancreatic elastase results in direct alveolar tissue destruction, enlarged airspaces and reduction of the elastic recoil of the lungs (183–185), all of which are contributing to problems in breathing. The elastase is typically administered via the oropharynx or via the nares. However, the intranasal application route is associated with the disadvantage of inhomogeneous distribution of the instilled solution within the respiratory system as the distribution efficiency is dependent on several parameters like delivery volume and anesthesia depth (186). Several studies found the oropharyngeal administration superior to the intranasal one, since the application via the oropharynx resulted in more homogenous distribution of compounds across both sides of the lung and across all lobes (187,188). Thus, in this dissertation the elastase was administered oropharyngeally. By using this elastase model on WT and *Trpml3*$^{-/-}$ mice, it should be investigated, whether lung function is further declining and tissue destruction increasing under such disease conditions. Indeed, all measured lung function parameters, i.e. Elastance, dynamic Compliance, Inspiratory Capacity, Tissue Elasticity, Total Lung Capacity and Quasi-Static Compliance, were changed in the direction of a pulmonary emphysema phenotype in

Trpml3$^{-/-}$ mice compared to WT. Additionally, under the elastase treatment, the lung emphysema phenotype in *Trpml3*$^{-/-}$ mice was further exacerbated as compared with WT mice. The same applied to the recorded pressure-volume-loops that showed emphysema-typical shifts approaching bigger volumes in *Trpml3*$^{-/-}$ mice. Larger volumes upon maximal inflation, meaning maximal pressure, are typically found in an emphysematous lung (183,189), because of the destruction of alveolar tissue and the enlarged airspaces providing more space for inhaled air. These pathological changes of the lung tissue were also visualized through H&E-stained lung paraffin slices. *Trpml3*$^{-/-}$ mice lungs exhibited clearly and significantly enlarged airspaces in comparison to WT mice, both with control treatment and under elastase application. The most prominent changes were again found in elastase treated *Trpml3*$^{-/-}$ mice, which was further confirmed by quantification of airspace enlargements as mean linear chord length (MLI) for every group. Conclusively, the lung function results were in line with the lung histology analysis, both pointing to an emphysematous lung condition in *Trpml3*$^{-/-}$ mice and suggesting that TRPML3 loss results in higher susceptibility of the mice to develop emphysema.

4.2.2 The smoke-induced COPD mouse model

The exposure to CS is known to be the most relevant root of COPD, including emphysema development. Therefore, it appeared obvious and mandatory to investigate the effect of tobacco smoke on WT and *Trpml3*$^{-/-}$ mice. In addition, it is better reflecting the human COPD disease. While the elastase application induces direct and fast atrophy of alveolar lung tissue measurable shortly after the application (190), the effects of cigarette smoke exposure on lung tissue are rather slowly developing. Therefore, mice were chronically treated with cigarette smoke over a long-term period of two months and analyzed thereafter regarding respiratory mechanics and lung histology. Similar to the elastase-induced emphysema model, the cigarette smoke treatment induced changes of Elastance and dynamic Compliance in the direction of lung emphysema in *Trpml3*$^{-/-}$ mice compared to WT. These pathological changes were further confirmed by lung histology images and measurements of MLI, showing the strongest phenotype for CS-exposed *Trpml3*$^{-/-}$ mice. Interestingly, single-cell RNA sequencing data obtained from murine WT lungs that were exposed either to 2 or 6 months of CS or to FA control, showed a strong upregulation of TRPML3 channel expression, nearly exclusively in AMΦ (1). This suggested that TRPML3 might play a pivotal role during COPD development and progression.

In summary, the two most common used mouse models for COPD and lung emphysema were used here, and both pointed to a pathological lung emphysema phenotype present in *Trpml3*$^{-/-}$ mice.

4.3 Mechanisms for the lung emphysema phenotype of *Trpml3*$^{-/-}$ mice

4.3.1 Role of MMP-12

The enhanced inflammation present in COPD is particularly mediated by certain immune cells like macrophages, neutrophils and $CD8^+$ T-cells, as well as their secretions such as inflammatory mediators (cytokines and chemokines) and proteolytic enzymes (130). The analysis of BAL-F revealed increased levels of the macrophage specific MMP-12 in *Trpml3*$^{-/-}$ in comparison to WT samples, while several other inflammation mediators (IFNγ, IL10, KC/CXCL1, IL6, KC/CXCL9, IL4, VEGF, and MIP2) and MMPs (MMP-9, MMP-2) were unchanged. MMP-12 has been investigated quite intensively in the context of COPD and emphysema development, as it is capable of degrading elastin of the ECM. Production and secretion of MMP-12 has been found to be upregulated upon smoke exposure (191,192). Additionally, *Mmp-12*$^{-/-}$ mice are protected against emphysema after chronic exposure to tobacco smoke (193) and MMP-12 polymorphisms were described to be linked to COPD severity (123,194). In this context, Haq et al. and Hunninghake et al. found that possession of the minor allele of SNPs in *Mmp-12* (rs2276109 or rs652438) is related to protective effects on COPD onset and progression (123,194). Furthermore, inhibitors for MMPs, e.g. for MMP-9/MMP-12 or MMP-12 specifically, have been developed and successfully used for treatments of animals, as they were able to reduce airspace enlargements and the inflammatory responses after cigarette smoke exposure or elastase treatment (195–198). All these findings clearly underline the relevance specifically of MMP-12 in COPD and emphysema development. Thus, it was suggested that the lung emphysema phenotype found for *Trpml3*$^{-/-}$ mice are due to elevated MMP-12 concentrations in BAL-F. MMP-12 is a protease degrading elastin of the ECM and resulting in degradation products such as desmosine found in urine or BAL-F. Desmosine is therefore used as biomarker for elastin degredation (172,173). In line with this, increased desmosine levels were detected in BAL-F obtained from *Trpml3*$^{-/-}$ mice, suggesting that this is a direct result of the increased amounts of MMP-12. Additionally, lung tissue stainings to visualize elastin (VVG staining) revealed a reduction of elastic fibers in *Trpml3*$^{-/-}$ lungs compared to WT, both under basal conditions and even stronger with elastase treatment. However, the activity of MMPs and MMP-12 is regulated endogenously by TIMPs. E.g., MMP-12 can be inhibited by TIMP-1 and TIMP-2 (199–202). The

concentrations of both inhibitors, TIMP-1 and TIMP-2, were not altered between WT vs. *Trpml3*$^{-/-}$ BAL-F samples concluding that the increased amounts of MMP-12 in BAL-F of *Trpml3*$^{-/-}$ mice are not compensated by increased amounts of its inhibitors. Obviously, in BAL-F of *Trpml3*$^{-/-}$ mice the ratios between MMP-12 and TIMPs are shifted in favor of an overabundance of MMP-12. Such disbalance between proteases like MMP-12 and TIMPs is proposed to be one fundamental pathomechanism involved in COPD or emphysema development (130,203,204).

The increased MMP-12 levels measured in *Trpml3*$^{-/-}$ BAL-F might be due to AMΦ, but could also be mediated through other lung cell types, e.g. lung epithelial cells (205,206). Therefore, it was essential to relate the increased MMP-12 levels specifically to TRPML3-deficient AMΦ and possible functional changes. In this regard, an elevation of MMP-12 was also measured in the SN obtained from *Trpml3*$^{-/-}$ AMΦ cultures in comparison to WT cultures, suggesting that the alterations of MMP-12 in BAL-F are most likely due to functional changes of AMΦ lacking TRPML3 and not due to other cell types. Besides, transcriptomic data could show that MMP-12 is most strongly associated with macrophage populations of the lung, whereas it is seems widely absent in lung epithelial cells (1). Nevertheless, MMP-12 was not the only MMP being increased in the SN from *Trpml3*$^{-/-}$ AMΦ cultures. This applied also to MMP-8, otherwise named neutrophil collagenase. MMP-8 is a collagen-cleaving enzyme and is thereby capable of remodeling the ECM. So far, MMP-8 has been implicated in different forms of cancer (207,208), in metastasis suppression (209), in cardiovascular diseases (210,211), and in rheumatoid arthritis (212), but was not associated with lung-related diseases. Further and according to transcriptomic data, MMP-8 is most strongly associated with neutrophils (1). Thus, an involvement of MMP-8 in the pathomechanism of emphysema development in *Trpml3*$^{-/-}$ mice seemed unlikely. Of note, other lung disease related mediators, i.e. SP-D, MMP-3, MMP-9, and MMP-2 were found unchanged in BAL-F or AMΦ SN obtained from WT and *Trpml3*$^{-/-}$ mice. In conclusion, all arguments mentioned above are clearly favoring MMP-12 as the emphysema-inducing factor in *Trpml3*$^{-/-}$ mice.

4.3.2 Role of TRPML3 in AMΦ

Deriving from the clear link between AMΦ and MMP-12, and the knowledge of high TRPML3 expression in AMΦ, the increased MMP-12 levels in *Trpml3*$^{-/-}$ samples resulted most probably from functional changes in *Trpml3*$^{-/-}$ AMΦ. An increased intracellular synthesis of MMP-12 in *Trpml3*$^{-/-}$ AMΦ could be excluded as a reason for the elevated MMP-12 concentrations, because mRNA levels were found to be unchanged between WT and *Trpml3*$^{-/-}$ AMΦ using qRT-PCR. This rather pointed to defects of TRPML3 deficient AMΦ

in regulating MMP-12 levels properly, e.g. through endolysosomal trafficking, secretion/exocytosis and/or uptake/endocytosis of the mediator. Suitably, TRPML3 has been reported to be located on intracellular organelles (26,30,31), such as EEs, LEs/LYs, suggesting the channel to be involved in processes like endocytosis (19), endolysosomal trafficking (17,20) and exocytosis (21,23). Additionally, using a novel and selective small agonist for TRPML3, named ML3-SA1, and whole-endolysosomal and whole-cell patch clamp techniques, TRPML3 currents were measureable in EEs and LEs/LYs isolated from AMΦ, but not in REs and not on the PM (1). Notably, TRPML3 is less active in LEs/LYs (pH 4-5), while being more active at higher pH as present in EEs (pH 6-7) (15,17,18), pointing to functional abnormalities in the early endosomal system when lacking TRPML3.

4.3.2.1 TRPML3 in endolysosomal trafficking and endocytosis

TRPML3 has been reported previously to be involved in endocytosis and intracellular trafficking (37,38), as well as in luminal Ca^{2+} regulation (213). Lelouvier et al. found that inhibition of TRPML3 function is associated with luminal Ca^{2+} accumulation and impaired acidification (higher pH) of endosomes resulting in enhanced endosomal fusion events (213). Contrarily, Martina et al. showed the endosomal pH to be higher in cells overexpressing TRPML3 (37). However, TRPML3 has been clearly implicated in endosomal pH regulation, but further studies are necessary to clarify the exact contribution of the channel. Further, TRPML3 was studied in the context of membrane trafficking and endocytosis (37,38). In these studies, fluorophore-conjugated epidermal growth factor (EGF) was used to monitor EGF endocytosis and its delivery from the PM to lysosomes for final degradation. During this process, EGF is internalized through receptor-mediated endocytosis (also called clathrin-mediated endocytosis) and activates EGF signaling pathways that regulate cell proliferation, differentiation, survival and growth (214). After that, the EGF and its receptor is directed to lysosomes, where it is degraded and its signaling terminated. It was found, that EGF receptor degradation is accelerated in cells expressing the channel-dead dominant negative TRPML3 (D458K) or when TRPML3 was knocked down by small interfering RNA, while EGF degradation was delayed in cells overexpressing TRPML3 (37,38). Moreover, Martina et al. found that overexpression of TRPML3 did not affect the internalization of EGF (37), while Kim et al. demonstrated increased endocytosis of transferrin (Tf) and EGF in cells with silenced TRPML3 and decreased endocytosis of Tf and EGF in cells with TRPML3 overexpression (38). Contradictory to their own presented results, they claim in the abstract that endocytosis is

reduced in case of knock-down of TRPML3 (38). However, the hitherto performed studies show different results and were not able to elucidate the role of TRPML3 in trafficking and endocytosis consistently. Additionally, these studies were exclusively based on artificial cellular systems, i.e. cell lines with TRPML3 overexpression or cells in which TRPML3 function was inhibited by expression of the channel-dead dominant negative mutant of TRPML3 (D458K) or silenced by the use of small interfering RNA. Overexpression of TRPML3 results in non-physiological channel concentrations and might lead to altered interactions, binding or localization compared to cells that natively express the channel. In this context, TRPML3 was found in the PM in overexpression systems, as demonstrated by whole-cell patch clamp experiments (18), while PM channel activity was not detectable in native TRPML3 expressing cells such as sensory hair cells or AMΦ (1,36). In this dissertation, native TRPML3 expressing AMΦ isolated from WT and *Trpml3*$^{-/-}$ mice and fluorescent Tf were employed as a probe to investigate intracellular trafficking and endocytosis. Similar to EGF, Tf is internalized through receptor-mediated endocytosis. Whereas EGF follows the degradation pathway, Tf is trafficked through early endosomes to recycling endosomes, from where the receptor is recycled back to the cells' surface (175). As a result, endocytosis of Tf was found to be reduced in *Trpml3*$^{-/-}$ AMΦ and trafficking of Tf back to the cell surface was delayed. Further co-localization experiments of Tf with the early endosomal marker EEA1 suggested that trafficking of Tf is suspended in *Trpml3*$^{-/-}$ AMΦ with a retention of Tf in early endosomes. These impairments of trafficking in lungs' AMΦ lacking TRPML3 might contribute to the emphysema lung phenotype of *Trpml3*$^{-/-}$ mice, as MMP-12 forward trafficking might be interrupted, similar to Tf, resulting in a backlog and accumulation of this factor in the ECM of the lung.

As already mentioned above, TRPML3 has been implicated in endocytosis, which can be sub-classified into pinocytosis and phagocytosis. Whereas phagocytosis describes the absorption of large particles e.g. bacteria, pinocytosis means the internalization of fluids (180). Pinocytosis can be further divided into clathrin-mediated endocytosis (CME), as described above for Tf and EGF, clathrin-independent endocytosis (CIE) and macropinocytosis (MP) (180). CME describes the internalization of specific cargo from the surface into calthrin-coated vesicles that are pinched off the membrane by the use of dynamin enzyme (215). On the contrary, CIE is an umbrella term for several pathways that are all independent of clathrin (216). Finally, MP involves the uptake of extracellular material into vesicles called macropinosomes in an actin dependent manner (217). It has been reported to play functional roles in the uptake of nutrients and in the acquisition and processing of antigens for presentation on macrophage or dendritic cell surfaces (218,219), constituting a key process in adaptive immunity. In this dissertation, the role of TRPML3 in endocytosis was investigated, more precisely in CME by using fluorescent

Tf and in MP by the use of a fluorescent dextran probe. Similar to the reduced Tf uptake into *Trpml3*$^{-/-}$ AMΦ, the dextran uptake over time through MP was reduced as well compared to WT AMΦ. These impairments of endocytosis found for TRPML3 deficient AMΦ might be another rationale for the increased MMP-12 levels found in *Trpml3*$^{-/-}$ mouse lungs' fluid, as the mediator might be insufficiently taken up for intracellular recycling or degradation, thereby resulting in pathological concentrations of MMP-12.

4.3.2.2 TRPML3 – endocytosis – MMP-12

As described above, a clear link between TRPML3 and endocytosis was found in this work and was suggested to affect the extracellular MMP-12 levels. To proof this hypothesis further, meaning that MMP-12 is less endocytosed in *Trpml3*$^{-/-}$ AMΦ, MMP-12 was measured in the SN from cultured AMΦ (WT vs. *Trpml3*$^{-/-}$) after blockage of various endocytosis pathways using respective inhibitors. Of note, endocytosis of MMP-12 has been reported before by Koppisetti et al. They found MMP-12 to bind to plasma and intracellular membrane bilayers and further observed MMP-12 endocytosis and trafficking in HeLa cells within minutes (220). In line with this, MMP-12 activity was found specifically at the PM of BAL macrophages and around them (221). However, the exact mechanisms of uptake, trafficking and processing of MMP-12 remained largely elusive (222). Nevertheless, the results of this dissertation were able to provide some new insights into this topic. Dyn, an inhibitor for CME (180,223), was not affecting the MMP-12 levels in both WT and *Trpml3*$^{-/-}$ AMΦ SN, suggesting that this endocytosis pathway is not involved in the internalization of MMP-12. Next, MBCD, a blocker for CIE (179,180,223), increased the MMP-12 concentration in both WT and *Trpml3*$^{-/-}$ AMΦ SN, meaning that MMP-12 is endocytosed through CIE, but in a TRPML3 independent manner, as MBCD also has an effect in the absence of TRPML3. On the other hand, the MP blocker EIPA (180,223) showed MMP-12 accumulation effects only in WT AMΦ SN, suggesting that EIPA exhibited a TRPML3-dependent effect on the uptake of MMP-12, as this effect was gone when TRPML3 is lacking. Taken together, MMP-12 is likely taken up via CIE and MP, but not via CME. Even more, TRPML3 was found to play a role in MP of MMP-12 through AMΦ. This involvement of TRPML3 was corroborated by results showing decreased MMP-12 levels in WT AMΦ SN after activation of TRPML3 through the selective agonist ML3-SA1. This demonstrated that activation of TRPML3 in AMΦ is effecting MMP-12 levels of the SN, possibly through modulation or enhancement of endocytosis resulting in increased uptake of MMP-12 back into the cells. In these experiments, a selective antagonist of TRPML3 could have been used to potentially mimic the observed *Trpml3*$^{-/-}$ AMΦ phenotype with increased extracellular MMP-12 levels, but

since such a selective TRPML3 antagonist is at present not available, the selective agonist of TRPML3 (ML3-SA1) was used instead. Anyways, modulation of the TRPML3 channel, e.g. its activation through selective agonists as shown here, has the potential to positively influence the regulation capacity of AMΦ for MMP-12, thus preventing pathological concentrations of the mediator. In this regard, the TRPML3 channel appears as a potential target for drugs to induce a proper regulation of MMP-12 levels in the lungs, which would be valuable in the treatment of emphysema and COPD.

4.3.2.3 TRPML3 in lysosomal exocytosis and lysosomal pH

TRPML3 has been shown to be present within the proximal endosomal system, namely on EEs, but was also found to be expressed on LEs/LYs (26,30,31). Its localization on LEs and LYs suggests TRPML3 to be involved in lysosomal exocytosis, although the channel activity in these organelles is much lower as compared with EEs, because of the acidic condition in LEs/LYs (pH 4-5) (15,17,18). Similarly, lysosomal TRPML3 was activated in human bladder epithelial cells when the lysosomal pH was neutralized through therein-contained bacteria and the resulting Ca^{2+} release induced lysosomal exocytosis (23). Thus, alterations of the lysosomal pH in the direction of a more neutralized condition are able to induce lysosomal exocytosis and an increased lysosomal exocytosis of MMP-12 would also constitute an explanation for elevated, extracellular MMP-12 levels. However, lysosomal pH measurements of WT and *Trpml3*$^{-/-}$ AMΦ revealed no differences, pointing to a normal and physiological lysosomal function (1). Still, lysosomal exocytosis was evaluated using WT and *Trpml3*$^{-/-}$ AMΦ to assess any defects in lysosomal exocytosis itself. Using two different approaches, ß-hexosaminidase assay and LAMP1 translocation assay, it was shown that, firstly, loss of TRPML3 is not resulting in enhanced lysosomal exocytosis, and secondly, activation of TRPML3 through ML3-SA1 is not inducing lysosomal exocytosis. However, the closely related TRPML1 channel is expressed on the lysosomal membrane as well (41), and is known to induce lysosomal exocytosis upon activation of the channel (22). Therefore, TRPML1 activity was measured in WT vs. *Trpml3*$^{-/-}$ AMΦ using endolysosomal path-clamp technique and a recently published agonist of TRPML1, named ML1-SA1, that was shown to be selective for TRPML1 over TRPML2 and TRPML3 (1). These experiments demonstrated a normal activity of the TRPML1 channel in LYs of *Trpml3*$^{-/-}$ AMΦ (1). Thus, an increased secretion of MMP-12 through enhanced lysosomal exocytosis mediated through TRPML1 or TRPML3 channel activity could be excluded as a cause for the elevated MMP-12 concentration in *Trpml3*$^{-/-}$ lungs.

4.3.2.4 TRPML3 in autophagy

Autophagy is the natural “self-eating” process of the cell with the aim to clean the body from damaged or dysfunctional cells or organelles or from intracellular pathogens (224). It constitutes a strongly regulated mechanism that involves, as a final step, the fusion of autophagosomes, loaded with the material to be cleared, with LYs to form autolysosomes whereby the material is finally degraded (224). Autophagy was found to be associated with COPD pathogenesis in various respects (225,226). On the one hand, activation of autophagy is boosting the inflammatory response and epithelial cell death thereby promoting COPD progression (227,228). On the other hand, the lungs are protected through activation of autophagy due to enhanced clearance of bacteria that is preventing lung infections (229). In line with this, defects in autophagy were found in AMΦ of smokers being especially vulnerable for lung infections (230). Interestingly, TRPML3 has been implicated in autophagy as well. Thus, overexpression of TRPML3 was shown to enhance autophagy, as shown by increased amounts of LC3 positive autophagosomes (24,37,38). Loss of TRPML3, as in *Trpml3*$^{-/-}$ mice, could therefore be related with reduced autophagy, which might result in lung infections and COPD progression. Anyways, using WB analysis, decreased amounts of LC3II protein were found in *Trpml3*$^{-/-}$ AMΦ under normal conditions, but LC3II was unchanged between WT and *Trpml3*$^{-/-}$ AMΦ with bafilomycin A1 treatment (1), which inhibits the fusion of autophagosomes and lysosomes (231). Thus, *Trpml3*$^{-/-}$ AMΦ exhibit defects in the formation of autophagosomes, but still can be considered as autophagy competent cells (1). Concluding, the discovered alterations in autophagy in *Trpml3*$^{-/-}$ mice might contribute to the COPD/emphysema phenotype, especially if infections are present.

5. Outlook

5.1 TRPML3 as a novel therapeutic target for COPD treatment

Currently, no therapeutic drugs are available that can slow down the progression of COPD or reduce its mortality. Until now, the known relevance of MMPs in COPD pathogenesis, especially of MMP-9 and MMP-12, guided the development of broad or selective MMP inhibitors that were able to reduce the burden of inflammation and prevent pathological tissue remodeling in the lungs (195,196,232). All these studies were performed in animals, usually mice or guinea pigs. However, Dahl et al. conducted a randomized, placebo-controlled trial using an oral MMP-9/MMP-12 inhibitor, AZD1236, for the treatment of female and male COPD patients aged ≥ 40 (233). In this study, no significant effects were seen on inflammatory biomarkers of sputum, desmosine levels, lung function parameters or COPD symptoms between the placebo and treatment group (233). The discrepancy between the studies in animals and the trial in humans might stem from the different timepoints of the drug intervention. While the study animals were treated with the drug from the early onset of the CS-induced COPD development, human patients were treated late in disease progression, when COPD and all related pathological processes had already manifested. This generally also shows the difficulty and problems when transferring results from experimental animals to humans. Anyways, the hitherto lack of clinical efficacy of MMP inhibitors underlines the urgent need to find novel strategies and novel drug targets for the treatment of COPD. The endolysosomal cation channel TRPML3 might potentially be such a target. In this dissertation, loss of TRPML3 was found to be associated with a COPD/emphysema phenotype in mice due to impairments of TRPML3 deficient AMΦ to properly balance MMP-12 levels in the lungs. Thus, TRPML3 apparently plays an essential functional role in keeping the lungs in a physiological and healthy condition. In this context, modulation of the TRPML3 channel in AMΦ through small molecule agonists might help to enhance the uptake and clearance of excess MMP-12 in the lungs, and thus might prevent the emphysematous tissue remodeling driven by MMP-12 and further disease progression. Of note, a selective TRPML3 agonist is actually available, ML3-SA1, deriving from the modification of SN-2, a small molecule activator of TRPML3 that was published earlier (36). ML3-SA1 has been shown to be selective for TRPML3, over TRPML1 and TRPML2, and was able to activate TRPML3 in AMΦ in endolysosomal patch-clamp experiments (1). Targeting an endolysosomal cation channel such as TRPML3 constitutes a completely novel treatment strategy for COPD.

Additionally, gene array data are supporting the involvement of the TRPML3 channel in COPD in humans. Analysis of several data sets revealed higher expression of TRPML3 in lung tissue obtained from smokers with COPD compared to healthy smokers, as well as higher TRPML3 expression in BAL macrophages from smokers in comparison with non-smokers (1). Obviously, TRPML3 is strongly upregulated in COPD and through smoking, confirming the relevance of the channel also in humans and supporting the idea of TRPML3 as a potential drug target.

References

1. Spix B, Butz ES, Chen C-C, Rosato AS, Tang R, Jeridi A, et al. Lung emphysema and impaired macrophage elastase clearance in mucolipin 3 deficient mice. Nat Commun. 2022;13(1):1–18.
2. Klumperman J, Raposo G. The complex ultrastructure of the endolysosomal system. Cold Spring Harb Perspect Biol. 2014;6(10):1–22.
3. Grimm C. Endolysosomal Cation Channels as Therapeutic Targets—Pharmacology of TRPML Channels. Messenger. 2017;5(1):30–6.
4. O'sullivan MJ, Lindsay AJ. The endosomal recycling pathway—at the crossroads of the cell. Int J Mol Sci. 2020;21(17):1–21.
5. Bucci C, Stasi M. Endosome to Lysosome Transport. Vol. 2, Encyclopedia of Cell Biology. Elsevier Ltd.; 2016. 408–417 p.
6. Coutinho MF, Prata MJ, Alves S. Mannose-6-phosphate pathway: A review on its role in lysosomal function and dysfunction. Mol Genet Metab. 2012;105(4):542–50.
7. Buratta S, Tancini B, Sagini K, Delo F, Chiaradia E, Urbanelli L, et al. Lysosomal exocytosis, exosome release and secretory autophagy: The autophagic- and endo-lysosomal systems go extracellular. Int J Mol Sci. 2020;21(7):1–20.
8. Tancini B, Buratta S, Delo F, Sagini K, Chiaradia E, Pellegrino RM, et al. Lysosomal exocytosis: The extracellular role of an intracellular organelle. Membranes (Basel). 2020;10(12):1–21.
9. Martinez O, Goud B. Rab proteins. Biochim Biophys Acta - Mol Cell Res. 1998;1404(1–2):101–12.
10. Zhao C, Slevin JT, Whiteheart SW. Cellular functions of NSF: Not just SNAPs and SNAREs. FEBS Lett. 2007;581(11):2140–9.
11. Shen D, Wang X, Xu H. Pairing phosphoinositides with calcium ions in endolysosomal dynamics. BioEssays. 2011;33(6):448–57.
12. Cheng X, Shen D, Samie M, Xu H. Mucolipins: Intracellular TRPML1-3 channels. FEBS Lett. 2010;584(10):2013–21.
13. Venkatachalam K, Thomas H, Montell C. Lysosomal localization of TRPML3 depends on TRPML2 and the mucolipidosis-associated protein TRPML1. J Biol Chem. 2006;281(25):17517–27.
14. Dong XP, Shen D, Wang X, Dawson T, Li X, Zhang Q, et al. PI(3,5)P2 Controls Membrane Traffic by Direct Activation of Mucolipin Ca2+ Release Channels in the Endolysosome. Nat Commun. 2010;1(4):38.
15. Chen CC, Butz ES, Chao YK, Grishchuk Y, Becker L, Heller S, et al. Small Molecules for Early Endosome-Specific Patch Clamping. Cell Chem Biol. 2017;24(7):907–16.
16. Chen CC, Keller M, Hess M, Schiffmann R, Urban N, Wolfgardt A, et al. A small molecule restores function to TRPML1 mutant isoforms responsible for mucolipidosis type IV. Nat Commun. 2014;5(May):1–10.
17. Plesch E, Chen CC, Butz E, Rosato AS, Krogsaeter EK, Yinan H, et al. Selective agonist of TRPML2 reveals direct role in chemokine release from innate immune cells. Elife. 2018;7:1–23.
18. Kim HJ, Li Q, Tjon-Kon-Sang S, So I, Kiselyov K, Soyombo AA, et al. A novel

mode of TRPML3 regulation by extracytosolic pH absent in the varitint-waddler phenotype. EMBO J. 2008;27(8):1197–205.

19. Lelouvier B, Puertollano R. Mucolipin-3 regulates luminal calcium, acidification, and membrane fusion in the endosomal pathway. J Biol Chem. 2011;286(11):9826–32.

20. Venkatachalam K, Wong C-O, Zhu MX. The Role of TRPMLs in Endolysosomal Trafficking and Function. Cell Calcium. 2016;58(1):48–56.

21. Rosato AS, Tang R, Grimm C. Two-pore and TRPML cation channels: Regulators of phagocytosis, autophagy and lysosomal exocytosis. Pharmacol Ther. 2021;220.

22. Samie M, Wang X, Zhang X, Goschka A, Li X, Cheng X, et al. A TRP Channel in the Lysosome Regulates Large Particle Phagocytosis via Focal Exocytosis. PLoS One. 2017;32(7):736–40.

23. Miao Y, Li G, Zhang X, Xu H, Abraham SN. A TRP channel senses lysosome neutralization by pathogens to trigger their expulsion. Cell. 2015;161(6):1306–19.

24. Scotto Rosato A, Montefusco S, Soldati C, Di Paola S, Capuozzo A, Monfregola J, et al. TRPML1 links lysosomal calcium to autophagosome biogenesis through the activation of the CaMKKβ/VPS34 pathway. Nat Commun. 2019;10(1).

25. Grimm C, Barthmes M, Wahl-schott C. TRPML3. In: Mammalian Transient Receptor Potential (TRP) Cation Channels Handbook of Experimental Pharmacology, vol 222. 2014. p. 659–74.

26. Di Palma F, Belyantseva IA, Kim HJ, Vogt TF, Kachar B, Noben-Trauth K. Mutations in Mcoln3 associated with deafness and pigmentation defects in varitint-waddler (Va) mice. Proc Natl Acad Sci U S A. 2002;99(23):14994–9.

27. Kim HJ, Li Q, Tjon-Kon-Sang S, So I, Kiselyov K, Muallem S. Gain-of-function mutation in TRPML3 causes the mouse varitint-waddler phenotype. J Biol Chem. 2007;282(50):36138–42.

28. Cuajungco MP, Samie MA. The varitint-waddler mouse phenotypes and the TRPML3 ion channel mutation: Cause and consequence. Pflugers Arch Eur J Physiol. 2008;457(2):463–73.

29. Nagata K, Zheng L, Madathany T, Castiglioni AJ, Bartles JR, García-Añoveros J. The varitint-waddler (Va) deafness mutation in TRPML3 generates constitutive, inward rectifying currents and causes cell degeneration. Proc Natl Acad Sci U S A. 2008;105(1):353–8.

30. Grimm C, Cuajungco MP, Van Aken AFJ, Schnee M, Jörs S, Kros CJ, et al. A helix-breaking mutation in TRPML3 leads to constitutive activity underlying deafness in the varitint-waddler mouse. Proc Natl Acad Sci U S A. 2007;104(49):19583–8.

31. Xu H, Delling M, Li L, Dong X, Clapham DE. Activating mutation in a mucolipin transient receptor potential channel leads to melanocyte loss in varitint-waddler mice. Proc Natl Acad Sci U S A. 2007;104(46):18321–6.

32. Castiglioni, Andrew J., Remis, Natalie N., Flores, Emma N., Garcia-Anoveros J. Expression and vesicular localization of mouse Trpml3 in stria vascularis, hair cells, and vomeronasal and olfactory receptor neurons. J Comp Neurol. 2011;519(6):1095–114.

33. Kim HJ, Yamaguchi S, Li Q, So I, Muallem S. Properties of the TRPML3 channel pore and its stable expansion by the varitint-waddler-causing mutation. J Biol Chem. 2010;285(22):16513–20.

34. Samie MA, Grimm C, Evans JA, Curcio-Morelli C, Heller S, Slaugenhaupt SA, et al. The tissue-specific expression of TRPML2 (MCOLN-2) gene is influenced by the presence of TRPML1. Pflugers Arch Eur J Physiol. 2009;459(1):79–91.

35. Remis NN, Wiwatpanit T, Castiglioni AJ, Flores EN, Cantú JA, García-Añoveros J. Mucolipin Co-deficiency Causes Accelerated Endolysosomal Vacuolation of Enterocytes and Failure-to-Thrive from Birth to Weaning. PLoS Genet. 2014;10(12).

36. Grimm C, Jörs S, Saldanha SA, Obukhov AG, Pan B, Oshima K, et al. Small Molecule Activators of TRPML3. Chem Biol. 2010;17(2):135–48.

37. Martina JA, Lelouvier B, Puertollano R. The calcium channel Mucolipin-3 is a novel regulator of trafficking alon the endosomal pathway. Traffic. 2009;10(8):1443–1156.

38. Kim HJ, Soyombo AA, Tjon-Kon-Sang S, So I, Muallem S. The Ca 2+ channel TRPML3 regulates membrane trafficking and autophagy. Traffic. 2009;10(8):1157–67.

39. Bargal R, Avidan N, Ben-Asher E, Olender Z, Zeigler M, Frumkin A, et al. Identification of the gene causing mucolipidosis type IV. Nat Genet. 2000;26(1):118–21.

40. Sun M, Goldin E, Stahl S, Falardeau JL, Kennedy JC, Acierno JS, et al. Mucolipidosis type IV is caused by mutations in a gene encoding a novel transient receptor potential channel. Hum Mol Genet. 2000;9(17):2471–8.

41. Pryor PR, Reimann F, Gribble FM, Luzio JP. Mucolipin-1 is a lysosomal membrane protein required for intracellular lactosylceramide traffic. Traffic. 2006;7(10):1388–98.

42. Chen CS, Bach G, Pagano RE. Abnormal transport along the lysosomal pathway in Mucolipidosis, type IV disease. Proc Natl Acad Sci U S A. 1998;95(11):6373–8.

43. Bargal R, Bach G. Mucolipidosis type IV: Abnormal transport of lipids to lysosomes. J Inherit Metab Dis. 1997;20(5):625–32.

44. LaPlante JM, Sun M, Falardeau J, Dai D, Brown EM, Slaugenhaupt SA, et al. Lysosomal exocytosis is impaired in mucolipidosis type IV. Mol Genet Metab. 2006;89(4):339–48.

45. Medina DL, Fraldi A, Bouche V, Annunziata F, Mansueto G, Spampanato C, et al. Transcriptional activation of lysosomal exocytosis promotes cellular clearance. Dev Cell. 2011;21(3):421–30.

46. Dayam RM, Saric A, Shilliday RE, Botelho RJ. The Phosphoinositide-Gated Lysosomal Ca2+ Channel, TRPML1, Is Required for Phagosome Maturation. Traffic. 2015;16(9):1010–26.

47. Vergarajauregui S, Connelly PS, Daniels MP, Puertollano R. Autophagic dysfunction in mucolipidosis type IV patients. Hum Mol Genet. 2008;17(17):2723–37.

48. Jennings JJ, Zhu JH, Rbaibi Y, Luo X, Chu CT, Kiselyov K. Mitochondrial aberrations in mucolipidosis type IV. J Biol Chem. 2006;281(51):39041–50.

49. Medina DL, Di Paola S, Peluso I, Armani A, De Stefani D, Venditti R, et al. Lysosomal calcium signaling regulates autophagy via calcineurin and TFEB. Nat Cell Biol. 2015;17(3):288–99.

50. Settembre C, Zoncu R, Medina DL, Vetrini F, Erdin S, Erdin S, et al. A lysosome-to-nucleus signalling mechanism senses and regulates the lysosome via mTOR

and TFEB. EMBO J. 2012;31(5):1095–108.

51. Onyenwoke RU, Sexton JZ, Yan F, Díaz MCH, Forsberg LJ, Major MB, et al. The mucolipidosis IV Ca2+ channel TRPML1 (MCOLN1) is regulated by the TOR kinase. Biochem J. 2015;470(3):331–42.

52. Sun X, Yang Y, Zhong XZ, Cao Q, Zhu XH, Zhu X, et al. A negative feedback regulation of MTORC1 activity by the lysosomal Ca2+ channel MCOLN1 (mucolipin 1) using a CALM (calmodulin)-dependent mechanism. Autophagy. 2018;14(1):38–52.

53. Zhang X, Cheng X, Yu L, Yang J, Calvo R, Patnaik S, et al. MCOLN1 is a ROS sensor in lysosomes that regulates autophagy. Nat Commun. 2016;7(May).

54. Jung J, Cho K, Naji AK, Clemons KN, Wong CO, Villanueva M, et al. HRAS-driven cancer cells are vulnerable to TRPML1 inhibition. EMBO Rep. 2019;20(4):1–22.

55. Xu M, Almasi S, Yang Y, Yan C, Sterea AM, Rizvi Syeda AK, et al. The lysosomal TRPML1 channel regulates triple negative breast cancer development by promoting mTORC1 and purinergic signaling pathways. Cell Calcium. 2019;79:80–8.

56. Grimm C, Jörs S, Guo Z, Obukhov AG, Heller S. Constitutive activity of TRPML2 and TRPML3 channels versus activation by low extracellular sodium and small molecules. J Biol Chem. 2012;287(27):22701–8.

57. Lev S, Zeevi DA, Frumkin A, Offen-Glasner V, Bach G, Minke B. Constitutive activity of the human TRPML2 channel induces cell degeneration. J Biol Chem. 2010;285(4):2771–82.

58. Sun L, Hua Y, Vergarajauregui S, Diab HI, Puertollano R. Novel Role of TRPML2 in the Regulation of the Innate Immune Response. J Immunol. 2015;195(10):4922–32.

59. Lindvall JM, Blomberg KEM, Wennborg A, Smith CIE. Differential expression and molecular characterisation of Lmo7, Myo1e, Sash1, and Mcoln2 genes in Btk-defective B-cells. Cell Immunol. 2005;235(1):46–55.

60. Lingala SM, Ghany MGMMhs. The Mucolipin-2 (TRPML2) Ion Channel: a tissue-specific protein crucial to normal cell function. Pflugers Arch. 2016;25(3):289–313.

61. Valadez JA, Cuajungo MP. PAX5 is the transcriptional activator of Mucolipin-2 (MCOLN2) gene. Gene. 2015;555(2):194–202.

62. Cuajungco MP, Basilio LC, Silva J, Hart T, Tringali J, Chen C, et al. Cellular Zinc Levels are Modulated by Trpml1-Tmem163 Interaction. Traffic. 2014;14(11):1247–65.

63. Condamine T, Le Texier L, Howie D, Lavault A, Hill M, Halary F, et al. Tmem176B and Tmem176A are associated with the immature state of dendritic cells. J Leukoc Biol. 2010;88(3):507–15.

64. Rinkenberger N, Schoggins W. Mucolipin-2 Cation Channel Increases Trafficking Efficiency of Endocytosed Viruses. MBio. 2018;9(1):1–16.

65. Vaupel P, Schaible H-G, Mutschler E. Anatomie, Physiologie, Pathophysiologie des Menschen. 7. Auflage. Wissenschaftliche Vertragsgesellschaft Stuttgart; 2015. 315–318 p.

66. Weibel ER. Geometric and Dimensional Airway Models of Conductive, Transitory and Respiratory Zones of the Human Lung. Morphometry Hum Lung Springer, Berlin, Heidelberg. 1963;136–42.

67. Hyde DM, Hamid Q, Irvin CG. Anatomy, pathology, and physiology of the

tracheobronchial tree: emphasis on the distal airways. J Allergy Clin Immunol. 2009;124(6 Suppl):S72–7.

68. Leiva-Juárez MM, Kolls JK, Evans SE. Lung epithelial cells: therapeutically inducible effectors of antimicrobial defense. Mucosal Immunol. 2018;11(1):21–34.

69. Sleigh MA, Blake JR, Liron N. The Propulsion of Mucus by Cilia. Am Rev Respir Dis. 1998;137(3):726–41.

70. Bustamante-Marin XM, Ostrowski LE. Cilia and mucociliary clearance. Cold Spring Harb Perspect Biol. 2017;9(4):1–17.

71. Groneberg DA, Eynott PR, Oates T, Lim S, Wu R, Carlstedt I, et al. Expression of MUC5AC and MUC5B mucins in normal and cystic fibrosis lung. Respir Med. 2002;96(2):81–6.

72. Thornton DJ, Rousseau K, McGuckin MA. Structure and function of the polymeric mucins in airways mucus. Annu Rev Physiol. 2008;70:459–86.

73. Fahy J V., Dickey BF. Airway Mucus Function and Dysfunction John. N Engl J Med. 2010;363(23):2233–47.

74. Kim YD, Bae CH, Song SY, Choi YS. Effect of β-glucan on MUC4 and MUC5B expression in human airway epithelial cells. Int Forum Allergy Rhinol. 2015;5(8):708–15.

75. Fujisawa T, Chang MMJ, Velichko S, Thai P, Hung LY, Huang F, et al. NF-κB mediates IL-1β- and IL-17A-induced MUC5B expression in airway epithelial cells. Am J Respir Cell Mol Biol. 2011;45(2):246–52.

76. Zhert G, Sung WP, Nguyenvu LT, Rodriguez MW, Barbeau R, Paquet AC, et al. IL-13 and epidermal growth factor receptor have critical but distinct roles in epithelial cell mucin production. Am J Respir Cell Mol Biol. 2007;36(2):244–53.

77. Cuthbert AW, Murthy M, Darlington APS. Neural control of submucosal gland and apical membrane secretions in airways. Physiol Rep. 2015;3(6):1–11.

78. Dajani R, Zhang Y, Taft PJ, Travis SM, Starner TD, Olsen A, et al. Lysozyme secretion by submucosal glands protects the airway from bacterial infection. Am J Respir Cell Mol Biol. 2005;32(6):548–52.

79. Wine JJ, Joo NS. Submucosal glands and airway defense. Proc Am Thorac Soc. 2004;1(1):47–53.

80. Widdicombe JH, Wine JJ. Airway gland structure and function. Physiol Rev. 2015;95(4):1241–319.

81. Crystal RG, Randell SH, Engelhardt JF, Voynow J, Sunday ME. Airway epithelial cells: Current concepts and challenges. Proc Am Thorac Soc. 2008;5(7):772–7.

82. Boers JE, Ambergen AW, Thunnissen FBJM. Number and proliferation of Clara cells in normal human airway epithelium. Am J Respir Crit Care Med. 1999;159(5 I):1585–91.

83. Rokicki W, Rokicki M, Wojtacha J, Dzeljijli A. The role and importance of club cells (Clara cells) in the pathogenesis of some respiratory diseases. Kardiochirurgia i Torakochirurgia Pol. 2016;13(1):26–30.

84. Niden AH. Bronchiolar and large alveolar cell in pulmonary phospholipid metabolism. Science (80-). 1967;158(3806):1323–4.

85. Barnes PJ. Club cells, their secretory protein, and COPD. Chest. 2015;147(6):1447–8.

86. Park HY, Churg A, Wright JL, Li Y, Tam S, Man SFP, et al. Club cell protein 16 and disease progression in chronic obstructive pulmonary disease. Am J Respir

Crit Care Med. 2013;188(12):1413–9.

87. Snyder JC, Reynolds SD, Hollingsworth JW, Li Z, Kaminski N, Stripp BR. Clara cells attenuate the inflammatory response through regulation of macrophage behavior. Am J Respir Cell Mol Biol. 2010;42(2):161–71.

88. Reynolds SD, Malkinson AM. Clara Cell: Progenitor for the Bronchiolar Epithelium. Int J Biochem Cell Biol. 2010;42(1):1–4.

89. Boyd MR. Evidence for the Clara cell as a site of cytochrome P450-dependent mixed-function oxidase acitivity in lung. Nature. 1977;269:713–5.

90. Fanucchi MV, Murphy ME, Buckpitt AR, Philpot RM, Plopper CG. Pulmonary Cytochrome P450 Monooxygenase and Clara Cell Differentiation in Mice. Am J Respir Cell Mol Biol. 1997;17(3):302–14.

91. Boers JE, den Brok JLM, Koudstaal J, Arends JW, Thunnissen FBJM. Number and proliferation of Neuroendocrine cells in normal human airway epithelium. Am J Respir Crit Care Med. 1996;154:758–63.

92. Reynolds SD, Giangreco A, Power JHT, Stripp BR. Neuroepithelial bodies of pulmonary airways serve as a reservoir of progenitor cells capable of epithelial regeneration. Am J Pathol. 2000;156(1):269–78.

93. Noguchi M, Furukawa KT, Morimoto M. Pulmonary neuroendocrine cells: Physiology, tissue homeostasis and disease. DMM Dis Model Mech. 2021;13(12).

94. Van Lommel A. Pulmonary neuroendocrine cells (PNEC) and neuroepithelial bodies (NEB): Chemoreceptors and regulators of lung development. Paediatr Respir Rev. 2001;2(2):171–6.

95. Song H, Yao E, Lin C, Gacayan R, Chen MH, Chuang PT. Functional characterization of pulmonary neuroendocrine cells in lung development, injury,and tumorigenesis. Proc Natl Acad Sci U S A. 2012;109(43):17531–6.

96. Davis JD, Wypych TP. Cellular and functional heterogeneity of the airway epithelium. Mucosal Immunol. 2021;14(5):978–90.

97. Rock JR, Randell SH, Hogan BLM. Airway basal stem cells: A perspective on their roles in epithelial homeostasis and remodeling. DMM Dis Model Mech. 2010;3(9–10):545–56.

98. Hakim A, Usmani OS. Structure of the Lower Respiratory Tract. Third Edit. Reference Module in Biomedical Sciences. Elsevier; 2014. 1–8 p.

99. White ES. Lung extracellular matrix and fibroblast function. Ann Am Thorac Soc. 2015;12(Suppl 1):S30–3.

100. Burgstaller G, Oehrle B, Gerckens M, White ES, Schiller HB, Eickelberg O. The instructive extracellular matrix of the lung: Basic composition and alterations in chronic lung disease. Eur Respir J. 2017;50(1).

101. Aspal M, Zemans RL. Mechanisms of ATII-to-ATI cell differentiation during lung regeneration. Int J Mol Sci. 2020;21(9).

102. Crapo JD, Barry BE, Gehr P, Bachofen M, Weibel ER. Cell number and cell characteristics of the normal human lung. Am Rev Respir Dis. 1982;125(6):740–5.

103. Andreeva A V., Kutuzov MA, Voyno-Yasenetskaya TA. Regulation of surfactant secretion in alveolar type II cells. Am J Physiol - Lung Cell Mol Physiol. 2007;293(2).

104. Han SH, Mallampalli RK. The role of surfactant in lung disease and host defense against pulmonary infections. Ann Am Thorac Soc. 2015;12(5):765–74.

105. Wu H, Kuzmenko A, Wan S, Schaffer L, Weiss A, Fisher JH, et al. Surfactant proteins A and D inhibit the growth of Gram-negative bacteria by increasing membrane permeability. J Clin Invest. 2003;111(10):1589–602.

106. McCormack FX, Gibbons R, Ward SR, Kuzmenko A, Wu H, Deepe GS. Macrophage-independent fungicidal action of the pulmonary collectins. J Biol Chem. 2003;278(38):36250–6.

107. Brinker KG, Garner H, Wright JR. Surfactant protein A modulates the differentiation of murine bone marrow-derived dendritic cells. Am J Physiol - Lung Cell Mol Physiol. 2003;284(1 28-1):232–41.

108. Cheng G, Ueda T, Nakajima H, Nakajima A, Kinjyo S, Motojima S, et al. Suppressive effects of SP-A on ionomycin-induced IL-8 production and release by eosinophils. Int Arch Allergy Immunol. 1998;117(suppl 1):59–62.

109. Whitsett JA, Wert SE, Weaver TE. Diseases of pulmonary surfactant homeostasis. Annu Rev Pathol Mech Dis. 2015;10:371–93.

110. Yoshida M, Whitsett JA. Alveolar macrophages and emphysema in surfactant protein-D-deficient mice. Respirology. 2006;11:37–40.

111. Statistisches Bundesamt. 18% mehr Krankenhausfälle wegen raucherspezifischer Erkrankungen binnen zehn Jahren [Internet]. 2021. Available from: https://www.destatis.de/DE/Presse/Pressemitteilungen/2021/05/PD21_N036_23.html

112. WHO. The top 10 causes of death [Internet]. 2020. Available from: https://www.who.int/en/news-room/fact-sheets/detail/the-top-10-causes-of-death

113. Raherison C, Girodet PO. Epidemiology of COPD. Eur Respir Rev. 2009;18(114):213–21.

114. Ko FWS, Tam W, Tze WW, Chan DPS, Tung AH, Lai CKW, et al. Temporal relationship between air pollutants and hospital admissions for chronic obstructive pulmonary disease in Hong Kong. Thorax. 2007;62(9):779–84.

115. Morgan G, Corbett S, Wlodarczyk J. Air pollution and hospital admissions in Sydney, Australia, 1990 to 1994. Am J Public Health. 1998;88(12):1761–6.

116. Hnizdo E, Sullivan PA, Bang KM, Wagner G. Association between chronic obstructive pulmonary disease and employment by industry and occupation in the US population: A study of data from the Third National Health and Nutrition Examination Survey. Am J Epidemiol. 2002;156(8):738–46.

117. Barker DJP, Godfrey KM, Fall C, Osmond C, Winter PD, Shaheen SO. Relation of birth weight and childhood respiratory infection to adult lung function and death from chronic obstructive airways disease. Br Med J. 1991;303:671–5.

118. Donaldson GC, Seemungal TAR, Bhowmik A, Wedzicha JA. Relationship between exacerbation frequency and lung function decline in chronic obstructive pulmonary disease. Thorax. 2002;57:847–52.

119. Molfino NA. Genetics of COPD. Chest. 2004;125(5):1929–40.

120. Chappell S, Daly S, Morgan K, Baranes TG, Roca J, Rabinovich R, et al. Cryptic Haplotypes of SERPINA1 Confer Susceptibility to Chronic Obstructive Pulmonary Disease. Hum Mutat. 2006;27(1):103–9.

121. Stoller JK, Aboussouan LS. Alpha1-Antitrypsin Deficiency. Lancet. 2005;365(9478):2225–36.

122. Ito I, Nagai S, Handa T, Muro S, Hirai T, Tsukino M, et al. Matrix metalloproteinase-9 promoter polymorphism associated with upper lung dominant

emphysema. Am J Respir Crit Care Med. 2005;172(11):1378–82.

123. Haq I, Chappell S, Johnson SR, Lotya J, Daly L, Morgan K, et al. Association of MMP - 12 polymorphisms with severe and very severe COPD: A case control study of MMPs - 1, 9 and 12 in a European population. BMC Med Genet. 2010;11(1):0–10.

124. Evren E, Ringqvist E, Willinger T. Origin and ontogeny of lung macrophages: from mice to humans. Immunology. 2019;160(2):126–38.

125. Guilliams M, De Kleer I, Henri S, Post S, Vanhoutte L, De Prijck S, et al. Alveolar macrophages develop from fetal monocytes that differentiate into long-lived cells in the first week of life via GM-CSF. J Exp Med. 2013;210(10):1977–92.

126. Hashimoto D, Chow A, Noizat C, Teo P, Beasley MB, Leboeuf M, et al. Tissue-resident macrophages self-maintain locally throughout adult life with minimal contribution from circulating monocytes. Immunity. 2013;38(4):792–804.

127. Maus UA, Janzen S, Wall G, Srivastava M, Blackwell TS, Christman JW, et al. Resident alveolar macrophages are replaced by recruited monocytes in response to endotoxin-induced lung inflammation. Am J Respir Cell Mol Biol. 2006;35(2):227–35.

128. Rubins JB. Alveolar Macrophages Wielding the Double-Edged Sword of Imflammation. Am J Respir Crit Care Med. 2003;167(2):103–4.

129. Hu G, Christman JW. Editorial: Alveolar macrophages in Lung Inflammation and Resolution. Front Immunol. 209AD;10(2275).

130. MacNee W. Pathology, pathogenesis, and pathophysiology. Br J Pharmacol. 2006;32:1202–4.

131. Boer WI De, Sont JK, Schadewijk A Van, Stolk J, Krieken JH Van, Hiemstra PS. Monocyte chemoattractant protein 1, interleukin 8, and chronic airways inflammation in COPD. J Pathol. 2000;190(5):619–26.

132. Manuscript A. Cytotoxic potential of lung CD8+ T cells increases with COPD severity and with in vitro stimulation with IL-18 or IL-15. 2010;184(11):6504–13.

133. Pandey KC, De S, Mishra PK. Role of proteases in chronic obstructive pulmonary disease. Front Pharmacol. 2017;8:1–9.

134. Churg A, Zhou S, Wright JL. Matrix metalloproteinases in COPD. Eur Respir J. 2012;39(1):197–209.

135. Lee EJ, In KH, Kim JH, Lee SY, Shin C, Shim JJ, et al. Proteomic analysis in lung tissue of smokers and COPD patients. Chest. 2009;135(2):344–52.

136. Linder R, Rönmark E, Pourazar J, Behndig A, Blomberg A, Lindberg A. Serum metalloproteinase-9 is related to COPD severity and symptoms - cross-sectional data from a population based cohort-study. Respir Res. 2015;16(1):1–9.

137. Legrand C, Gilles C, Zahm JM, Polette M, Buisson AC, Kaplan H, et al. Airway epithelial cell migration dynamics: MMP-9 role in cell- extracellular matrix remodeling. J Cell Biol. 1999;146(2):517–29.

138. Lemjabbar H, Gosset P, Lamblin C, Tillie I, Hartmann D, Wallaert B, et al. Contribution of 92 kDa gelatinase/type IV collagenase in bronchial inflammation during status asthmaticus. Am J Respir Crit Care Med. 1999;159(4 I):1298–307.

139. Demedts IK, Morel-Montero A, Lebecque S, Pacheco Y, Cataldo D, Joos GF, et al. Elevated MMP-12 protein levels in induced sputum from patients with COPD. Thorax. 2006;61(3):196–201.

140. Segura-Valdez L, Pardo A, Gaxiola M, Uhal BD, Becerril C, Selman M.

Upregulation of gelatinases A and B, collagenases 1 and 2, and increased parenchymal cell death in COPD. Chest. 2000;117(3):684–94.

141. Kasahara Y, Tuder RM, Cool CD, Lynch DA, Flores SC, Voelkel NF. Endothelial cell death and decreased expression of vascular endothelial growth factor and vascular endothelial growth factor receptor 2 in emphysema. Am J Respir Crit Care Med. 2001;163(3 I):737–44.

142. Garratt LW, Sutanto EN, Ling KM, Looi K, Iosifidis T, Martinovich KM, et al. Matrix metalloproteinase activation by free neutrophil elastase contributes to bronchiectasis progression in early cystic fibrosis. Eur Respir J. 2015;46(2):384–94.

143. Okada Y, Watanabe S, Nakanishi I, Kishi J ichi, Hayakawa T, Watorek W, et al. Inactivation of tissue inhibitor of metalloproteinases by neutrophil elastase and other serine proteinases. FEBS Lett. 1988;229(1):157–60.

144. Kim KC, Wasano K, Niles RM, Schuster JE, Stone PJ, Brody JS. Human neutrophil elastase releases cell surface mucins from primary cultures of hamster tracheal epithelial cells. Proc Natl Acad Sci U S A. 1987;84(24):9304–8.

145. Breuer R, Christensen TG, Lucey EC, Stone PJ, Snider GL. An ultrastructural morphometric analysis of elastase-treated hamster bronchi shows discharge followed by progressive accumulation of secretory granules. Am Rev Respir Dis. 1987;136(3):698–703.

146. Janoff A, Raju L, Dearing R. Levels of elastase activity in bronchoalveolar lavage fluids of healthy smokers and nonsmokers. Am Rev Respir Dis. 1983;127(5):540–4.

147. Belaaouaj A, McCarthy R, Baumann M, Gao Z, Ley TJ, Abraham SN, et al. Mice lacking neutrophil elastase reveal impaired host defense against gram negative bacterial sepsis. Nat Med. 1998;4(5):615–8.

148. Pryor WA, Stone K. Oxidants in Cigarette Smoke Radicals, Hydrogen Peroxide, Peroxynitrate, and Peroxynitrite. Ann N Y Acad Sci. 1993;686:12–27.

149. Inonu H, Doruk S, Sahin S, Erkorkmaz U, Celik D, Celikel S, et al. Oxidative stress levels in exhaled breath condensate associated with COPD and smoking. Respir Care. 2012;57(3):413–9.

150. Gerritsen WBM, Asin J, Zanen P, van den Bosch JMM, Haas FJLM. Markers of inflammation and oxidative stress in exacerbated chronic obstructive pulmonary disease patients. Respir Med. 2005;99(1):84–90.

151. Morrison D, Rahman I, Lannan S, MacNee W. Epithelial permeability, inflammation, and oxidant stress in the air spaces of smokers. Am J Respir Crit Care Med. 1999;159(2):473–9.

152. MacNee W, Rahman I. Is oxidative stress central to the pathogenesis of chronic obstructive pulmonary disease? Trends Mol Med. 2001;7(2):55–62.

153. Domej W, Oettl K, Renner W. Oxidative stress and free radicals in COPD-implications and relevance for treatment. Int J COPD. 2014;9:1207–24.

154. Keatings VM, Collins PD, Scott DM, Barnes PJ. Differences in Interleukin-8 and Tumor Necrosis Facfor-α in Induced Sputum from Patients with Chronic Obstructive Pulmonary Disease or Asthma. Am J Respir Crit Care Med. 1996;153(2):530–4.

155. Rangasamy T, Cho CY, Thimmulappa RK, Zhen L, Srisuma SS, Kensler TW, et al. Genetic ablation of Nrf2 enhances susceptibility to cigarette smoke-induced emphysema in mice. J Clin Invest. 2004;114(9):1248–59.

156. Kondo T, Tagami S, Yoshioka A, Nishimura M, Kawakami Y. Current smoking of elderly men reduces antioxidants in alveolar macrophages. Am J Respir Crit Care Med. 1994;149(1):178–82.

157. Täger M, Piecyk A, Köhnlein T, Thiel U, Ansorge S, Welte T. Evidence of a defective thiol status of alveolar macrophages from COPD patients and smokers. Chronic obstructive pulmonary disease. Free Radic Biol Med. 2000;29(11):1160–5.

158. Vaupel P, Schaible H-G, Mutschler E. Anatomie, Physiologie, Pathophysiologie des Menschen. 7. Auflage. Wissenschaftliche Vertragsgesellschaft Stuttgart; 2015. 351–358 p.

159. GOLD Commitee. Global Strategy for the diagnosis, management, and prevention of chronic obstructive pulmoary disease, 2021 Report [Internet]. 2021. Available from: https://goldcopd.org.

160. Anthonisen NR, Skeans MA, Wise RA, Manfreda J, Kanner RE, Connett JE. The Effects of a Smoking Cessation Intervention on 14.5-Year Mortality. Ann Intern Med. 2005;142:233–9.

161. Godtfredsen NS, Lam TH, Hansel TT, Leon ME, Gray N, Dresler C, et al. COPD-related morbidity and mortality after smoking cessation: Status of the evidence. Eur Respir J. 2008;32(4):844–53.

162. Newman SP. Drug delivery to the lungs: challenges and opportunities. Ther Deliv. 2017;8(8):647–61.

163. Antus B. Pharmacotherapy of Chronic Obstructive Pulmonary Disease: A Clinical Review. ISRN Pulmonol. 2013;2013:1–11.

164. Aktories K, Förstermann U, Hofmann FB, Klaus S. Allgemeine und spezielle Pharmakologie und Toxikologie. 11. Auflag. Elsevier GmbH.; 2013. 182–185 p.

165. Rabe KF. Update on roflumilast, a phosphodiesterase 4 inhibitor for the treatment of chronic obstructive pulmonary disease. Br J Pharmacol. 2011;163(1):53–67.

166. Appleton S, Poole P, Smith BJ, Veale A, Lasserson TJ, Chan MMK, et al. Long-acting beta2-agonists for poorly reversible chronic obstructive pulmonary disease. Cochrane Database Syst Rev. 2006;3(1).

167. Vogelmeier C, Hederer B, Glaab T, Schmidt H, Rutten-van Mölken MPMH, Beeh KM, et al. Tiotropium versus Salmeterol for the Prevention of Exacerbations of COPD. N Engl J Med. 2011;364(12):1093–103.

168. Jörs S, Grimm C, Becker L, Heller S. Genetic inactivation of Trpml3 does not lead to hearing and vestibular impairment in mice. PLoS One. 2010;5(12).

169. Schmittgen TD, Livak KJ. Analyzing real-time PCR data by the comparative CT method. Nat Protoc. 2008;3(6):1101–8.

170. Rodriguez I, Feinstein P, Mombaerts P. Variable Patterns of Axonal Projections of Sensory Neurons in the Mouse Vomeronasal System. Cell. 1999;97:199–208.

171. Wen S, Götze IN, Mai O, Schauer C, Leinders-Zufall T, Boehm U. Genetic identification of GnRH receptor neurons: A new model for studying neural circuits underlying reproductive physiology in the mouse brain. Endocrinology. 2011;152(4):1515–26.

172. Luisetti M, Ma S, Iadarola P, Stone PJ, Viglio S, Casado B, et al. Desmosine as a biomarker of elastin degradation in COPD: Current status and future directions. Eur Respir J. 2008;32(5):1146–57.

173. Turino GM, Ma S, Lin YY, Cantor JO, Luisetti M. Matrix elastin: A promising biomarker for chronic obstructive pulmonary disease. Am J Respir Crit Care Med.

2011;184(6):637–41.

174. Goerke J. Pulmonary surfactant: Functions and molecular composition. Biochim Biophys Acta. 1998;1408(2–3):79–89.

175. Mayle KM, Le AM, Kamei DT. The Intracellular Trafficking Pathway of Transferrin. Biochim Biophys Acta. 2012;1820(3):264–81.

176. Rodríguez A, Webster P, Ortego J, Andrews NW. Lysosomes behave as Ca2+-regulated exocytic vesicles in fibroblasts and epithelial cells. J Cell Biol. 1997;137(1):93–104.

177. Gerndt S, Chen CC, Chao YK, Yuan Y, Burgstaller S, Rosato AS, et al. Agonist-mediated switching of ion selectivity in TPC2 differentially promotes lysosomal function. Elife. 2020;9:1–63.

178. Li L, Wan T, Wan M, Liu B, Cheng R, Zhang R. The effect of the size of fluorescent dextran on its endocytic pathway. Cell Biol Int. 2015;39(5):531–9.

179. Vercauteren D, Vandenbroucke RE, Jones AT, Rejman J, Demeester J, De Smedt SC, et al. The use of inhibitors to study endocytic pathways of gene carriers: Optimization and pitfalls. Mol Ther. 2010;18(3):561–9.

180. Dutta D, Donaldson JG. Search for inhibitors of endocytosis. Cell Logist. 2012;2(4):203–8.

181. Wyatt A, Wartenberg P, Candlish M, Krasteva-Christ G, Flockerzi V, Boehm U. Genetic strategies to analyze primary TRP channel-expressing cells in mice. Cell Calcium. 2017;67:91–104.

182. Wartenberg P, Lux F, Busch K, Fecher-Trost C, Flockerzi V, Krasteva-Christ G, et al. A TRPV6 expression atlas for the mouse. Cell Calcium. 2021;100:102481.

183. Vanoirbeek JAJ, Rinaldi M, De Vooght V, Haenen S, Bobic S, Gayan-Ramirez G, et al. Noninvasive and invasive pulmonary function in mouse models of obstructive and restrictive respiratory diseases. Am J Respir Cell Mol Biol. 2010;42(1):96–104.

184. Suki B, Bartolák-Suki E, Rocco PRM. Elastase-induced lung emphysema models in mice. Methods Mol Biol. 2017;1639:67–75.

185. Hamakawa H, Bartolaḱ-Suki E, Parameswaran H, Majumdar A, Lutchen KR, Suki B. Structure-function relations in an elastase-induced mouse model of emphysema. Am J Respir Cell Mol Biol. 2011;45(3):517–24.

186. Southam DS, Dolovich M, O'Byrne PM, Inman MD. Distribution of intranasal instillations in mice: Effects of volume, time, body position, and anesthesia. Am J Physiol - Lung Cell Mol Physiol. 2002;282(4):833–9.

187. Egger C, Cannet C, Gérard C, Jarman E, Jarai G, Feige A, et al. Administration of Bleomycin via the Oropharyngeal Aspiration Route Leads to Sustained Lung Fibrosis in Mice and Rats as Quantified by UTE-MRI and Histology. PLoS One. 2013;8(5).

188. Lakatos HF, Burgess HA, Thatcher TH, Redonnet MR, Hernady E, Williams JP, et al. Oropharyngeal aspiration of a silica suspension produces a superior model of silicosis in the mouse when compared to intratracheal instillation. Exp Lung Res. 2006;32(5):181–99.

189. Harris RS. Pressure-volume curves of the respiratory system. Respir Care. 2005;50(1):78–99.

190. Vidal D, Fortunato G, Klein W, Cortizo L, Vasconcelos J, Ribeiro-dos-Santos R, et al. Alterations in pulmonary structure by elastase administration in a model of emphysema in mice is associated with functional disturbances. Rev Port

Pneumol. 2012;18(3):128–36.

191. Da Hora K, Valença SS, Porto LC. Immunohistochemical study of tumor necrosis factor-α, matrix metalloproteinase-12, and tissue inhibitor of metalloproteinase-2 on alveolar macrophages of BALB/c mice exposed to short-term cigarette smoke. Exp Lung Res. 2005;31(8):759–70.

192. Arunachalam G, Sundar IK, Hwang JW, Yao H, Rahman I. Emphysema is associated with increased inflammation in lungs of atherosclerosis-prone mice by cigarette smoke: Implications in comorbidities of COPD. J Inflamm. 2010;7:1–10.

193. Hautamaki RD, Kobayashi DK, Senior RM, Shapiro SD. Requirement for macrophage elastase for cigarette smoke-induced emphysema in mice. Science (80-). 1997;277(5334):2002–4.

194. Hunninghake GM, Cho MH, Tesfaigzi Y, Soto-Quiros ME, Melen E. MMP-12, Lung Function, and COPD in High-Risk Populations. N Engl J Med. 2009;361(27):2599–608.

195. Churg A, Wang R, Wang X, Onnervik PO, Thim K, Wright JL. Effect of an MMP-9/MMP-12 inhibitor on smoke-induced emphysema and airway remodelling in guinea pigs. Thorax. 2007;62(8):706–13.

196. Le Quément C, Guénon I, Gillon JY, Valença S, Cayron-Elizondo V, Lagente V, et al. The selective MMP-12 inhibitor, AS111793 reduces airway inflammation in mice exposed to cigarette smoke. Br J Pharmacol. 2008;154(6):1206–15.

197. Vandenbroucke RE, Dejonckheere E, Libert C. A therapeutic role for matrix metalloproteinase inhibitors in lung diseases? Eur Respir J. 2011;38(5):1200–14.

198. Shibata S, Miyake K, Tateishi T, Yoshikawa S, Yamanishi Y, Miyazaki Y, et al. Basophils trigger emphysema development in a murine model of COPD through IL-4–mediated generation of MMP-12–producing macrophages. Proc Natl Acad Sci U S A. 2018;115(51):13057–62.

199. Kim B, Abdel-Rahman MH, Wang T, Pouly S, Mahmoud AM, Cebulla CM. Retinal MMP-12, MMP-13, TIMP-1, and TIMP-2 expression in murine experimental retinal detachment. Investig Ophthalmol Vis Sci. 2014;55(4):2031–40.

200. Suomela S, Kariniemi AL, Snellman E, Saarialho-Kere U. Metalloelastase (MMP-12) and 92-kDa gelatinase (MMP-9) as well as their inhibitors, TIMP-1 and -3, are expressed in psoriatic lesions. Exp Dermatol. 2001;10(3):175–83.

201. Ishii T, Abboud RT, Wallace AM, English JC, Coxson HO, Finley RJ, et al. Alveolar macrophage proteinase/antiproteinase expression in lung function and emphysema. Eur Respir J. 2014;43(1):82–91.

202. John-Schuster G, Günter S, Hager K, Conlon TM, Eickelberg O, Yildirim AÖ. Inflammaging increases susceptibility to cigarette smoke-induced COPD. Oncotarget. 2016;7(21):30068–83.

203. Groutas WC, Dou D, Alliston KR. Neutrophil elastase inhibitors. Expert Opin Ther Pat. 2011;21(3):339–54.

204. Tetley TD. Macrophages and the Pathogenesis of COPD. Chest. 2002;121(5):156S-159S.

205. Qu P, Du H, Wang X, Yan C. Matrix metalloproteinase 12 overexpression in lung epithelial cells plays a key role in emphysema to lung bronchioalveolar adenocarcinoma transition. Cancer Res. 2009;69(18):7252–61.

206. Lavigne MC, Thakker P, Gunn J, Wong A, Miyashiro JS, Wasserman AM, et al. Human bronchial epithelial cells express and secrete MMP-12. Biochem Biophys Res Commun. 2004;324(2):534–46.

207. Sirniö P, Tuomisto A, Tervahartiala T, Sorsa T, Klintrup K, Karhu T, et al. High-serum MMP-8 levels are associated with decreased survival and systemic inflammation in colorectal cancer. Br J Cancer. 2018;119(2):213–9.

208. Thirkettle S, Decock J, Arnold H, Pennington CJ, Jaworski DM, Edwards DR. Matrix metalloproteinase 8 (collagenase 2) induces the expression of interleukins 6 and 8 in breast cancer cells. J Biol Chem. 2013;288(23):16282–94.

209. Decock J, Hendrickx W, Thirkettle S, Gutiérrez-Fernández A, Robinson SD, Edwards DR. Pleiotropic functions of the tumor- and metastasis-suppressing matrix metalloproteinase-8 in mammary cancer in MMTV-PyMT transgenic mice. Breast Cancer Res. 2015;17(1):1–13.

210. Kormi I, Nieminen MT, Havulinna AS, Zeller T, Blankenberg S, Tervahartiala T, et al. Matrix metalloproteinase-8 and tissue inhibitor of matrix metalloproteinase-1 predict incident cardiovascular disease events and all-cause mortality in a population-based cohort. Eur J Prev Cardiol. 2017;24(11):1136–44.

211. Tuomainen AM, Nyyssönen K, Laukkanen JA, Tervahartiala T, Tuomainen TP, Salonen JT, et al. Serum matrix metalloproteinase-8 concentrations are associated with cardiovascular outcome in men. Arterioscler Thromb Vasc Biol. 2007;27(12):2722–8.

212. Mattey DL, Nixon NB, Dawes PT. Association of circulating levels of MMP-8 with mortality from respiratory disease in patients with rheumatoid arthritis. Arthritis Res Ther. 2012;14(5).

213. Lelouvier B, Puertollano R. Mucolipin-3 regulates luminal calcium, acidification, and membrane fusion in the endosomal pathway. J Biol Chem. 2011;286(11):9826–32.

214. Wee P, Wang Z. Epidermal growth factor receptor cell proliferation signaling pathways. Cancers (Basel). 2017;9(5):1–45.

215. McMahon HT, Boucrot E. Molecular mechanism and physiological functions of clathrin-mediated endocytosis. Nat Rev Mol Cell Biol. 2011;12(8):517–33.

216. Mayor S, Pagano RE. Pathways of clathrin-independent endocytosis. Nat Rev Mol Cell Biol. 2007;8(8):603–12.

217. Canton J. Macropinocytosis: New insights into its underappreciated role in innate immune cell surveillance. Front Immunol. 2018;9:1–8.

218. Lim JP, Teasdale RD, Gleeson PA. SNX5 is essential for efficient macropinocytosis and antigen processing in primary macrophages. Biol Open. 2012;1(9):904–14.

219. Norbury CC, Chambers BJ, Prescott AR, Ljunggren HG, Watts C. Constitutive macropinocytosis allows TAP-dependent major histocompatibility compex class I presentation of exogenous soluble antigen by bone marrow-derived dendritic cells. Eur J Immunol. 1997;27(1):280–8.

220. Koppisetti RK, Fulcher YG, Jurkevich A, Prior SH, Xu J, Lenoir M, et al. Ambidextrous binding of cell and membrane bilayers by soluble matrix metalloproteinase-12. Nat Commun. 2014;5.

221. Cobos-Correa A, Trojanek JB, Diemer S, Mall MA, Schultz C. Membrane-bound FRET probe visualizes MMP12 activity in pulmonary inflammation. Nat Chem Biol. 2009;5(9):628–30.

222. Bassiouni W, Ali MAM, Schulz R. Multifunctional intracellular matrix metalloproteinases: implications in disease. FEBS J. 2021;288(24):7162–82.

223. Francia V, Reker-Smit C, Boel G, Salvati A. Limits and challenges in using

transport inhibitors to characterize how nano-sized drug carriers enter cells. Nanomedicine. 2019;14(12):1533–49.

224. Glick D, Barth S, Macleod KF. Autophagy: Cellular and molecular mechanisms. J Pathol. 2010;221(1):3–12.

225. Jiang S, Sun J, Mohammadtursun N, Hu Z, Li Q, Zhao Z, et al. Dual role of autophagy/mitophagy in chronic obstructive pulmonary disease. Pulm Pharmacol Ther. 2019;56(April):116–25.

226. Mizumura K, Cloonan S, Choi ME, Hashimoto S, Nakahira K, Ryter SW, et al. Autophagy: Friend or foe in lung disease? Ann Am Thorac Soc. 2016;13(March):S40–7.

227. Ryter SW, Chen ZH, Hong PK, Choi AMK. Autophagy in chronic obstructive pulmonary disease: Homeostatic or pathogenic mechanism? Autophagy. 2009;5(2):235–7.

228. Li Y, Yu G, Yuan S, Tan C, Xie J, Ding Y, et al. 14,15-Epoxyeicosatrienoic acid suppresses cigarette smoke condensateinduced inflammation in lung epithelial cells by inhibiting autophagy. Am J Physiol - Lung Cell Mol Physiol. 2016;311(5):L970–80.

229. Jati S, Kundu S, Chakraborty A, Mahata SK, Nizet V, Sen M. Wnt5A signaling promotes defense against bacterial pathogens by activating a host autophagy circuit. Front Immunol. 2018;9.

230. Monick MM, Powers LS, Walters K, Lovan N, Zhang M, Gerke A, et al. Identification of an Autophagy Defect in Smokers' Alveolar Macrophages. J Immunol. 2010;185(9):5425–35.

231. Yamamoto A, Tagawa Y, Yoshimori T, Moriyama Y, Masaki R, Tashiro Y. Bafilomycin A1 Prevents Maturation of Autophagic Vacuoles by Inhibiting Fusion between Autophagosomes and Lysosomes in Rat Hepatoma Cell Line, H-4-II-E Cells. Cell Struct Funct. 1998;23(1):33–42.

232. Pemberton PA, Cantwell JS, Kim KM, Sundin DJ, Kobayashi D, Fink JB, et al. An inhaled matrix metalloprotease inhibitor prevents cigarette smoke-induced emphysema in the mouse. COPD J Chronic Obstr Pulm Dis. 2005;2(3):303–10.

233. Dahl R, Titlestad I, Lindqvist A, Wielders P, Wray H, Wang M, et al. Effects of an oral MMP-9 and -12 inhibitor, AZD1236, on biomarkers in moderate/severe COPD: A randomised controlled trial. Pulm Pharmacol Ther. 2012;25(2):169–77.

Acknowledgements

At this point, I would like to thank all the people who supported me in many ways during the realization and preparation of my doctoral thesis.

First, I want to express my deepest gratitude to my supervisor Prof. Dr. Dr. Christian Grimm. Thank you for your great support, guidance, passion, and motivation, all of which have contributed significantly to the successful completion of the project. Cordial thanks to Prof. Dr. Martin Biel for initiating the project and for the support and guidance along the way.

Moreover, I have been very lucky for being part of the Research Training Group 2338, Targets in Toxicology, which was valuable in many respects. I got to know many nice people, was trained in various fields of toxicology and had the chance to exchange ideas with fellow young and experienced researchers. Also, I appreciate all activities and events outside of work organized within the framework of the GRK2338. Simply said, this program offered the best opportunity to develop myself within the scientific area. Thank you to all, who were involved making the group to what it is now, including Prof. Dr. med. Thomas Gudermann, PD Dr. Claudia Staab-Weijnitz, Dr. Julia Brandt, and Stefanie Resenberger.

Further, I would like to thank Dr. Önder Yildirim and his team, in specific Christine Hollauer, Dr. Aicha Jeridi, and Dr. Thomas Conlon, for exchanging, knowledge, techniques, and experience. Thank you for the tremendous support during all experiments I have performed at the Helmholtz-Institute. Marco, Jakob and Alexa, thank you for taking care of the mice and managing the breedings.

I am also particularly grateful for the cooperation with Prof. Dr. Ulrich Boehm, who shared the TRPML3 reporter mouse with us. Thank you for the warm welcome during the two lab visits in Homburg. Special thanks go to Dr. Philipp Wartenberg for teaching me the tissue preparations and Amanda Wyatt for shipping mice and answering my many questions.

I would also like to acknowledge all colleagues from the Walther Straub Institute, including members of the animal facility. I very much appreciated the cooperative working atmosphere and the great willingness to share materials, instruments, and ideas. Particularly, I want to thank my lovely currently and former colleagues from the Grimm lab: Carla, Anna, Julia, Yu-Kai, Einar, Dawid, Marcel, Eva-Maria, Irene, Veronika, Alina, Rachel. You all have been a great support to me! I really enjoyed working with you, chatting with you, suffering with you, being happy with you, celebrating with you…it has been a time that I will never forget.

Finally, I would like to express my deepest gratitude to the most important people in my life: my mother, my father, my wonderful sister, and Sebastian. I would not have come this far without your love, support, and belief in me. Sebastian, you accompanied me through all ups and downs and motivated me during difficult times. You were always there for me, and I cannot express how grateful I am to you. I would also like to thank my friends and my other family members distributed over Krefeld, Hamburg, and Viersen for providing all the distraction from work and giving the possibility to rest my mind.

In memory of my deceased mother, Elisabeth Spix, I would like to dedicate this dissertation to her. From the depths of my heart, I would like to thank her for the deep love, all the beautiful unforgettable moments and for everything she has given to me.

Affidavit

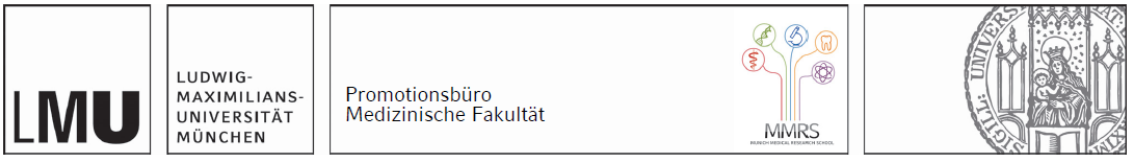

Affidavit

Spix, Barbara Julia

Surname, first name

Nußbaumstraße 26

Street

80336 Munich, Germany

Zip code, town, country

I hereby declare, that the submitted thesis entitled:

Endolysosomal cation channels and toxic chronic lung disease

is my own work. I have only used the sources indicated and have not made unauthorised use of services of a third party. Where the work of others has been quoted or reproduced, the source is always given.

I further declare that the submitted thesis or parts thereof have not been presented as part of an examination degree to any other university.

Munich, 20.05.22 — Barbara Julia Spix

place, date — Signature doctoral candidate

Confirmation of congruency

LMU LUDWIG-MAXIMILIANS-UNIVERSITÄT MÜNCHEN

Promotionsbüro Medizinische Fakultät

MMRS

Confirmation of congruency between printed and electronic version of the doctoral thesis

Spix, Barbara Julia

Surname, first name

Nußbaumstraße 26

Street

80336 Munich, Germany

Zip code, town, country

I hereby declare, that the submitted thesis entitled:

Endolysosomal cation channels and toxic chronic lung disease

is congruent with the printed version both in content and format.

Munich, 20.05.22

place, date

Barbara Julia Spix

Signature doctoral candidate